Quantitatively Designing Lithium Metal Batteries for Practical Applications

Lu, Bingyu

2023

UNIVERSITY OF CALIFORNIA SAN DIEGO

Quantitatively Designing Lithium Metal Batteries for Practical Applications

A dissertation submitted in partial satisfaction of the
requirements for the degree Doctor of Philosophy

in

NanoEngineering

by

Bingyu Lu

Committee in Charge:

Professor Ying Shirley Meng, Chair
Professor Ping Liu, Co-Chair
Professor Zheng Chen
Professor Eric Fullerton
Professor Oleg Shpyrko

2023

The Dissertation of Bingyu Lu is approved, and it is acceptable in quality and form for publication on microfilm and electronically.

University of California San Diego

2023

DEDICATION

To my Mother *Yinlan Zhao*, my Father *Wenbiao Lu* and my Wife *Lin Xia*.

EPIGRAPH

"Two things fill the mind with ever new and increasing admiration and awe, the more often and steadily we reflect upon them: the starry heavens above me and the moral law within me."

- Immanuel Kant, Critique of Practical Reason, 1788

TABLE OF CONTENTS

LIST OF FIGURES

LIST OF TABLES

ACKNOWLEDGEMENTS

First and foremost, I would like to thank my PhD advisor, Prof. Ying Shirley Meng. During the past six and half years since I was a undergraduate research assistant, she devoted so much time and energy to guide me, and offered support, and many valuable opportunities towards the success of my study and career. Outside research, she taught me how to develop my professionalism, confidence, as well as interpersonal relationship. I believe the training she offered me will benefit my life forever. Her dedication towards excellence will always be a great inspiration for me.

I would like to give my special thanks to my committee numbers Prof. Ping Liu, Prof. Eric Fullerton, Prof. Oleg Shpyrko and Prof. Zheng Chen for their efforts and guidance through the journey.

I would like to acknowledge my colleagues and co-authors in UCSD, Dr. Chengcheng Fang, Dr. Xuefeng Wang, Dr. Wurigumula Bao, Dr. Xiaowei Wang, Dr. Minghao Zhang, Dr. Shen Wang, Dr. Jean-Marie Doux, Dr. Darren H. S. Tan, Dr. Jonathan Scharf, Mr. Diyi Cheng, Mr. Yijie Yin, Mr. Bhargav Bhamwala, Mr. Saurabh Parab, Mr. Bhagath Sreenarayanan, Mr. Mr. Miguel Ceja, for all the collocative work and support. I am also grateful to all my lab mates in LESC who had helped and inspired me in many ways.

I would like to express my sincere thanks to all external collaborators. I would like to thank Dr. Boryann Liaw and Dr. Bin Li from Idaho National Laboratory, Prof. Sarah Tolbert and Mr. Edgar Olivera from University of California Los Angeles, Prof. Alejandro Franco and Dr. Mehdi Chouchane from University of Picardy Jules Verne. Dr. Mei Cai, Dr. Dai Fang and Dr. Shuru Chen from General Motors, Dr. Xu Wu and Dr. Cao Xiao from Pacific Northwestern National Laboratory for their generous support.

I would like to acknowledge the financial support from Office of Vehicle Technologies of the U.S. Department of Energy through the Advanced Battery Materials Research (BMR) Program (Battery500 Consortium) under Contract DE-EE0007764.

Last but not least, I would like to thank my parents and my wife, for their everlasting love, patience and support. Their understanding is the best gift in my life.

Chapter 2, in full, is a reprint of the material "Quantitatively Designing Porous Copper Current Collectors for Lithium Metal Anodes" as it appears in the ACS Applied Energy Materials, Bingyu Lu, Edgar Olivera, Jonathan Scharf, Mehdi Chouchane, Chengcheng Fang, Miguel Ceja, Lisa E. Pangilinan, Shiqi Zheng, Andrew Dawson, Diyi Cheng, Wurigumula Bao, Oier Arcelus, Alejandro A. Franco, Xiaochun Li, Sarah H. Tolbert, Ying Shirley Meng, 2021, 4, 7, 6454–6465. The dissertation author was the primary investigator and author of this paper.

Chapter 3, in full, is a reprint of the material "Editors' Choice—Methods—Pressure Control Apparatus for Lithium Metal Batteries" as it appears in the Journal of Electrochemical Society, Bingyu Lu, Wurigumula Bao, Weiliang Yao, Jean-Marie Doux, Chengcheng Fang, Ying Shirley Meng, 2022, 169, 070537, and "Pressure-tailored lithium deposition and dissolution in lithium metal batteries", as it appears in the Nature Energy, Chengcheng Fang*, **Bingyu Lu***, Gorakh Pawar, Minghao Zhang, Diyi Cheng, Shuru Chen, Miguel Ceja, Jean-Marie Doux, Henry Musrock, Mei Cai, Boryann Liaw, Ying Shirley Meng, 2021, 6, 987–994. The dissertation author was the primary investigator and author of these two papers.

Chapter 4, in full, is a reprint of the material “Suppressing Chemical Corrosions of Lithium Metal Anodes” as it appears in the Advanced Energy Materials, Bingyu Lu, Weikang Li, Diyi Cheng, Bhargav Bhamwala, Miguel Ceja, Wurigumula Bao, Chengcheng Fang, Ying Shirley Meng, 2022, 2202012. The dissertation author was the primary investigator and author of this paper.

Chapter 5, in full, is an unpublished material “Key Parameters in Determining the Reactivity of Lithium Metal Battery”, Bingyu Lu, Diyi Cheng, Bhagath Sreenarayanan, Weikang Li, Bhargav Bhamwala, Wurigumula Bao, Ying Shirley Meng. The dissertation author was the co-primary investigator and author of this paper.

VITA

2018	Bachelor of Science in NanoEngineering, University of California San Diego, La Jolla, U.S.
2021	Master of Science in NanoEngineering, University of California San Diego, La Jolla, U.S.
2023	Doctor of Philosophy in NanoEngineering, University of California San Diego, La Jolla, U.S.

PUBLICATIONS

1. **B. Lu**, E. Olivera, J. Scharf, M. Chouchane, C. Fang, M. Ceja, L. E. Pangilinan, S. Zheng, A. Dawson, D. Cheng, W. Bao, O. Arcelus, A. A. Franco, X. Li, S. H. Tolbert & Y. S. Meng, "Quantitatively Designing Porous Copper Current Collectors for Lithium Metal Anodes", ***ACS Appl. Energy Mater***. 2021, 4, 7, 6454–6465

2. C. Fang, **B. Lu (Co-first)**, G. Pawar, M. Zhang, D. Cheng, S. Chen, M. Ceja, J. Doux, H. Musrock, M. Cai, B. Liaw and Y. S. Meng, "Pressure-tailored lithium deposition and dissolution in lithium metal batteries", ***Nature Energy*** 2021, 6, 987–994

3. **B. Lu**, W. Li, D. Cheng, M. Ceja, W. Bao, C. Fang, Y. S. Meng, "Suppressing Chemical Corrosions of Lithium Metal Anodes", ***Adv. Energy Mater.*** 2022, 2202012

4. **B. Lu**, W. Bao, W. Yao, J.M. Doux, C. Fang, Y. S. Meng, "Methods – Pressure control apparatus for lithium metal battery", ***J. Electrochem. Soc.,*** 2022, 169, 070537

5. B. Liaw, G. Pawar, Y. S. Meng, C. Fang and **B. Lu**, "Perspective—Lithium Metal Nucleation and Growth on Conductive Substrates: A Multi-Scale Understanding from Atomistic, Nano-, Meso-, to Micro-Scales", ***J. Electrochem. Soc.,*** 2022, 169, 112505

6. J. Kim, M. H. Engelhard, **B. Lu**, Y. Xu, S. Tan, B. E. Matthews, S. Tripathi, X. Cao, C. Niu, E. Hu, S. Bak, C. Wang, Y. S. Meng, J. Zhang and W. Xu, "High Current-Density-Charging Lithium Metal Batteries Enabled by Double-Layer Protected Lithium Metal Anode", ***Adv. Funct. Mater.***, 2022, 2207172

7. R. Shimizu, D. Cheng, J. L. Weaver, M. Zhang, **B. Lu**, T. A. Wynn, R. Burger, M. Kim, G. Zhu and Y. S. Meng, "Unraveling the Stable Cathode Electrolyte Interface in all Solid-State Thin-Film Battery Operating at 5 V", ***Adv. Energy Mater.*** 2022, 2201119

8. Y. Yin, Y. Yang, D. Cheng, M. Mayer, J. Holoubek, W. Li, G. Raghavendran, A. Liu, **B. Lu**, D. M. Davies, Z. Chen, O. Borodin and Y. S. Meng, "Fire-extinguishing, recyclable liquefied gas electrolytes for temperature-resilient lithium-metal batteries", ***Nature Energy***, 2022, ASAP

9. U. Pal, D. Rakov, **B. Lu**, B. Sayahpour, F. Chen, B. Roy, D. R. MacFarlane, M. Armand, P. C. Howlett, Y. S. Meng and M. Forsyth, "Interphase control for high performance lithium metal batteries using ether aided ionic liquid electrolyte", ***Energy Environ. Sci.*** 2022, 15, 1907-1919

10. J. Scharf, M. Chouchane, D. P. Finegan, **B. Lu**, C. Redquest, M. Kim, W. Yao, A. A. Franco, D. Gostovic, Z. Liu, M. Riccio, F. Zelenka, J. Doux and Y. S. Meng, "Bridging nano- and microscale X-ray tomography for battery research by leveraging artificial intelligence", ***Nature Nanotechnology***, 2022, ASAP

11. D. Cheng, **B. Lu**, G. Raghavendran, M. Zhang and Y. S. Meng, "Leveraging cryogenic electron microscopy for advancing battery design", ***Matter***, 2022, 5, 26–42

12. B. Han, X. Li, S. Bai, Y. Zou, **B. Lu**, M. Zhang, X. Ma, Z. Chang, Y. S. Meng, M. Gu, "Conformal three-dimensional interphase of Li metal anode revealed by low-dose cryo electron microscopy", ***Matter***, 2021, 4, 1-12

13. W. Bao, C. Fang, D. Cheng, Y. Zhang, **B. Lu**, D. H. S. Tan, R. Shimizu, B. Sreenarayanan, S. Bai, W. Li, M. Zhang and Y. S. Meng, "Quantifying lithium loss in amorphous silicon thin-film anodes via titration-gas chromatography", ***Cell Reports Physical Science***, 2021, 2,100597

14. D. H. S. Tan, Y. Chen, H. Yang, W. Bao, B. Sreenarayanan, J. Doux, W. Li, **B. Lu**, S. Ham, B. Sayahpour, J. Scharf, E. A. Wu, G. Deysher, H. E. Han, H. J. Hah, H. Jeong, J. B. Lee, Z. Chen and Y. S. Meng, "Carbon-free high-loading silicon anodes enabled by sulfide solid electrolytes", ***Science,*** 2021, 373, 1494–1499

15. H. S. Hirsh, B. Sayahpour, A. Shen, W. Li, **B. Lu**, E. Zhao, M. Zhang and Y. S. Meng, "Role of electrolyte in stabilizing hard carbon as an anode for rechargeable sodium-ion batteries with long cycle life", ***Energy Storage Materials***, 2021, 42, 78–87

16. C. M. Efaw, **B. Lu**, Y. Lin, G. M. Pawar, P. R. Chinnam, M. F. Hurley, E. J. Dufek, Y. S. Meng, B. Li, "A closed-host bi-layer dense/porous solid electrolyte interphase for enhanced lithium-metal anode stability", ***Materials Today***. 2021, 49, 48-58

17. D. M. Davies, Y. Yang, E. S. Sablina, Y. Yin, M. Mayer, Y. Zhang, M. Olguin, J. Z. Lee, **B. Lu**, D. Damien, O. Borodin, C. S. Rustomji & Y. S. Meng, "A Safer, Wide-Temperature Liquefied Gas Electrolyte Based on Difluoromethane", ***Journal of Power Sources***, 2021, 493, 229668

18. D. Cheng, T. A. Wynn, X. Wang, S. Wang, M. Zhang, R. Shimizu, S. Bai, H. Nguyen, C. Fang, M. Kim, W. Li, **B. Lu**, S. J. Kim and Y. S. Meng, "Unveiling the Stable Nature of the Solid Electrolyte Interphase between Lithium Metal and LiPON via Cryogenic Electron Microscopy", ***Joule***, 2020, 4, 11, 2484-2500

19. X. Wang, G. Pawar, Y. Li, X. Ren, M. Zhang, **B. Lu**, A. Banerjee, P. Liu, E. J. Dufek, J. Zhang, J. Xiao, J. Liu, Y. S. Meng and B. Liaw, "Glassy Li metal anode for high-performance rechargeable Li batteries", ***Nature Materials***, 2020, 19, 1339–1345

20. C. Fang, J. Li, M. Zhang, Y. Zhang, F. Yang, J. Z. Lee, M. Lee, J. Alvarado, M. A. Schroeder, Y. Yang, **B. Lu**, N. Williams, M. Ceja, L. Yang, M. Cai, J. Gu, K. Xu, X. Wang and Y. S. Meng "Quantifying inactive lithium in lithium metal batteries", ***Nature***, 2019, 572, 511–515

21. X. Wang, Y. Li, X. Bi, L. Ma, T. Wu, M. Sina, S. Wang, M. Zhang, J. Alvarado, **B. Lu**, A. Banerjee, K. Amine, J. Lu, and Y. S. Meng "Hybrid Li-Ion and Li-O2 Battery Enabled by Oxyhalogen-Sulfur Electrochemistry", ***Joule,*** 2018, 2, 2381–2392

22. X. Wang, M. Zhang, J. Alvarado, S. Wang, M. Sina, **B. Lu**, J. Bouwer, W. Xu, J. Xiao, J.-G. Zhang, J. Liu, and Y. S. Meng "New Insights on the Structure of Electrochemically Deposited Lithium Metal and Its Solid Electrolyte Interphases via Cryogenic TEM", ***Nano Letters***, 2017, 17 (12), 7606

ABSTRACT OF THE DISSERTATION

Quantitatively Designing Lithium Metal Batteries for Practical Applications

by

Bingyu Lu

Doctor of Philosophy in NanoEngineering

University of California San Diego, 2023

Professor Ying Shirley Meng, Chair

Professor Ping Liu, Co-Chair

Lithium-ion battery (LIB) has been playing a vital part in the rapid adoption of electric vehicles and portable electronics. However, due to the limited energy density and poor safety properties of the current generation LIB, the development of longer-range and safe electric vehicles has been largely hindered. There is an urgent need for the new material design for the next generation of LIB, especially on the anode side. Among all the candidates, lithium metal is considered as the holy grail for the next generation battery anodes because of its high theoretical capacity (3,860 mAh/g, or 2,061 mAh/cm^3) and low electrochemical potential (–3.04 V versus the standard hydrogen electrode). Although extensive works have been done to prolong the cycle life of Li-metal batteries, including electrolyte engineering, interphase design, there are still a lot of studies need to be performed before the commercialization of the Lithium metal battery (LMB).

Here, by utilizing a series of characterization tools, the mechanical behaviors, chemical stability and safety properties of the Lithium metal anode in liquid electrolytes have been quantitatively studied. In addition to that, a porous copper current collector is also designed and synthesized for Lithium metal anode with high cycling Coulombic efficiency (CE). To study how the mechanical properties of the Lithium metal anode would affect the performance of the LMB, a split cell with pressure load cell is designed to precisely control the external stack pressure on the LMB during cycling. By employing Cryogenic Focused Ion Beam/ Scanning Electron Microscopy (Cryo FIB/SEM) and Cryogenic Electron Microscopy (Cryo-EM), the effects of external uniaxial stack pressure on the Lithium metal plating/stripping are systematically explored. It is found that by applying a 350-kPa stack pressure on the cell, a nearly 100% dense Lithium can be plated in the electrochemical process. The reversibility of this ultra-dense Lithium is also demonstrated up to 30 cycles. Next, by using three dimensional (3D) reconstruction from Cryo FIB/SEM and Titration Gas Chromatography, the chemical corrosion process of the Lithium metal in liquid electrolyte is thoroughly studied. It is shown that by limiting the contact surface area between the Lithium metal and the electrolyte, the chemical corrosion of the Lithium metal can be largely mitigated. In addition to that, a stable Solid Electrolyte Interphase (SEI) is also crucial for the chemical stability of the Lithium metal anode. The optimized Lithium anode shows less than 0.8% active material loss after 10 days of corrosion in liquid electrolyte. Lastly the safety property of the LMB is quantitatively studied by using Differential Scanning Calorimetry (DSC). The key parameters in controlling the reactivity of the LMB is presented. It is shown that the morphology of the Lithium metal anode, the thermal stability of the cathode and the electrolyte salts and solvents all play a synergetic role in the overall safety of the LMB. By optimizing the all the parameters, a safe LMB is demonstrated which shows no thermal response after being heated up to 400˚C.

Chapter 1 Introduction and Background

1.1 Lithium metal battery (LMB)

In the past a few decades, the world have witnessed the tremendous development in portable electronic devices as well as electric vehicles[1,2]. The current generation Lithium-ion battery (LIB) is unlikely to satisfy the bourgeon of market and the demand of the customers. A next generation battery needs to be developed to meet the growth of the industry. With its high theoretical capacity (3,860 mAh g^{-1}, or 2,061 mAh cm^{-3}) and low electrochemical potential (–3.04 V versus the standard hydrogen electrode), Li metal has been regarded as the ideal candidate for the next generation battery anode[3, 4]. In fact, Li metal anode is irreplaceable for Lithium-Sulfur and Lithium-Oxygen battery. Li metal anode together with lithium transition-metal oxide cathode can provide a specific energy of ~350 Wh kg^{-1}, which is more than double of that of LIB[4].

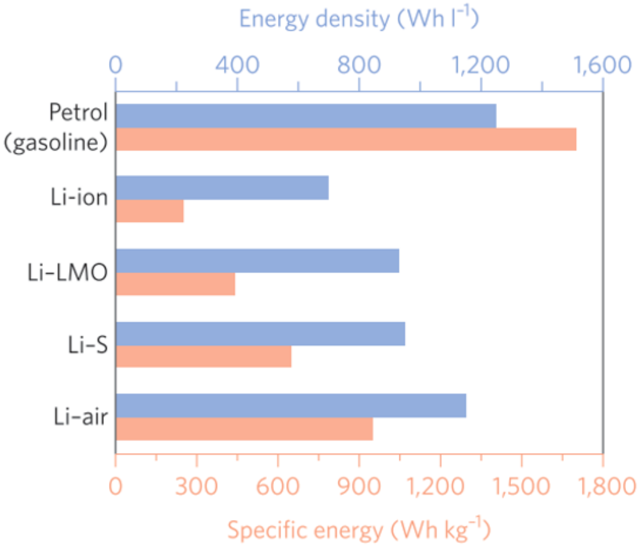

Figure 1.1 Bar chart showing the practical specific energy (pink) and energy densities (blue) of petrol (gasoline) and typical Li battery chemistries[4].

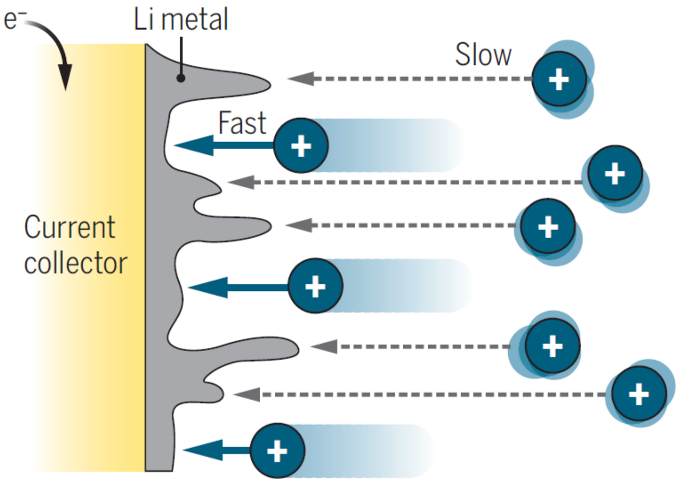

Figure 1.2 The formation of Li whiskers caused by the inhomogeneity in the interphase as well as the nonuniformity in the Li ion transportation from the electrolyte[5].

The research of LMB started in 1970s by Dr. Stanley Whittingham at Exxon. However, with more than 40 years passed, there has been no successful commercialization of Li metal anode. There are many formidable obstacles that need to be overcome before Li metal could be used as anode in commercial cells. The fundamental problem of Li metal anode lies upon the formation of lithium metal whiskers during the Li plating process[6]. Because of the highly negative electrochemical potential of Li^+/Li, all types of electrolytes will form SEI on the surface of Li metal[7]. However, the fragile structure of SEI could easily be fractured during the plating and stripping process[4]. Furthermore, the distribution of SEI component is usually heterogeneous, which leads to the heterogeneous ionic conductivity of the SEI. In addition to that, the local variation in the Li ion concentration in the electrolyte will also lead to a non-uniform Li ion flex during the electrochemical process[8]. The inhomogeneous ionic conductivity in the SEI together with the non-uniform Li ion flux from the electrolyte cause the growth of lithium whisker. The Li whisker could potentially penetrate the separator and cause a short circuit[3]. Also, the fractures of SEI and the formation of inactive Li would produce a large volume fluctuation during cycling, which would cause a mechanical issue for the battery. In the longer cycles of plating and stripping, the continuing formation and cracking of SEI would eventually isolate metallic Li from ionic conducting materials, causing so called “dead” Li. The SEI and the “dead” Li together lead to the low columbic efficiency of Li metal anode.

1.2 Electrolyte design for LMB

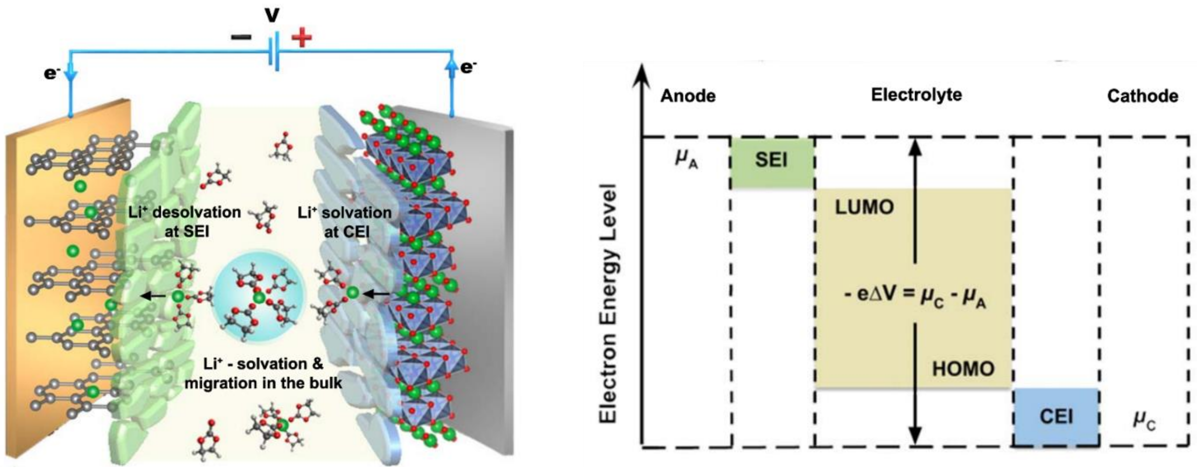

Figure 1.3 The working principles of electrolyte: ionic conducting, electronic insulating and stable at all interfaces. When the cell electrodes are operating at potentials beyond the region enclosed between LUMOs and HOMOs, a stable interphase must be formed to ensure the reversibility of the cell chemistry[10].

There have been several approaches proposed to deal with the Li metal challenge. One of the most crucial ones is the engineering of the electrolytes. The electrolyte is probably the most important component in a battery cell, because it has the duty to rapidly transport Li ions between cathode and anode while maintain a good stability toward the strongly oxidative cathode and strongly reductive anode (**Fig.1.3**)[10]. Many different types of electrolyte designing strategies have been proposed to prolong the cycle life of LMB. First are the electrolyte additives. Several additives have been tried to mitigate the growth of Li dendrite[11,12]. A controlled amount of Fluorinated additives in nonaqueous electrolyte could form a uniform layer of LiF on the Li metal anode surface.[12] The LiF layer could block electrolyte to decompose on the Li surface while still maintaining a good ionic conductivity[12]. However, due to the decomposition nature of the additives, the effectiveness of this engineering method has been questioned for long time. Another way to constrain the dendritic Li growth is to use highly concentrated electrolyte(HCE)[13,14]. Because HCE is able to provide enough cations to lower the critical current density by providing sufficient flux of Li ions during the plating process, Li dendrites could be successfully suppressed when HCE is used[4]. In Qian's work, 1,000 cycles with an average Coulombic efficiency of 98.4% in Copper-Lithium cell are achieved with 4M lithium bis(fluorosulfonyl)imide (LiFSI) in 1,2-dimethoxyethane (DME) electrolyte[13]. However, viscosity and cost of the HCE is usually high, hindering its practical use. Therefore, recently a new class of electrolyte called Localized High Concentration Electrolyte (LHCE) has been designed to cope with the issues of HCE[15–18]. The principle of LHCE is to add an inert diluent, a solvent that does not dissolve the electrolyte salt but is miscible with electrolyte solvent, into the HCE to dilute electrolyte while preserving the unique property of LHCE[16]. Bis(2,2,2-trifluoroethyl) ether (BTFE) and 1,1,2,2-Tetrafluoroethyl-2,2,3,3-Tetrafluoropropyl Ether (TTE) have been proven to be a good diluent for HCE[15]. The Li||Cu Coulombic efficiency (CE) (~99.5%) and the cycling stability have been largely improved with this type of LHCE[15].

1.3 Interphase design for LMB

The engineering of interface is also a popular strategy to boost the performance of LMB. Several artificial SEIs have been designed as a protective layer for Li metal anode[19–23]. By forming a layer of artificial SEI on the Li anode surface before contacting the electrolyte, the Li anode could be protected from reacting with electrolyte. The robust artificial SEI would retain its uniformity during plating and stripping process and also provide a uniform transportation of Li ion flux, thus preventing the growth of lithium dendrite[20]. The easiest way to construct an artificial SEI is through solution reaction. For example, a protective coating layer could be formed when clean Li metal is treated with solutions such as fluoroethylene carbonate[19] and 85 wt% H_3PO_4 in dimethylsulfoxide[20]. A uniform artificial SEI would form on the Li surface to prevent dendrite formation, leading to high CE and longer cycle life. Advanced thin-film fabrication techniques like atomic layer deposition (ALD)[24] and Langmuir–Blodgett film[25] are also used to construct protective layers for Li metal anode. Al_2O_3 has been successfully deposited on Li metal via ALD[24]. The ionic conducting $Li_xAl_2O_3$ is capable of protecting Li from organic solvent and even air corrosion while maintain a good Li ion transportation property[24]. The Li metal anode equipped with Al_2O_3 protective layer shows a longer cycle life than bare Li metal anode[24]. Finally, phosphate-functionalized reduced graphene oxides are grown on copper substrate via Langmuir–Blodgett method and then roll pressed on Li metal to create an artificial SEI[25].

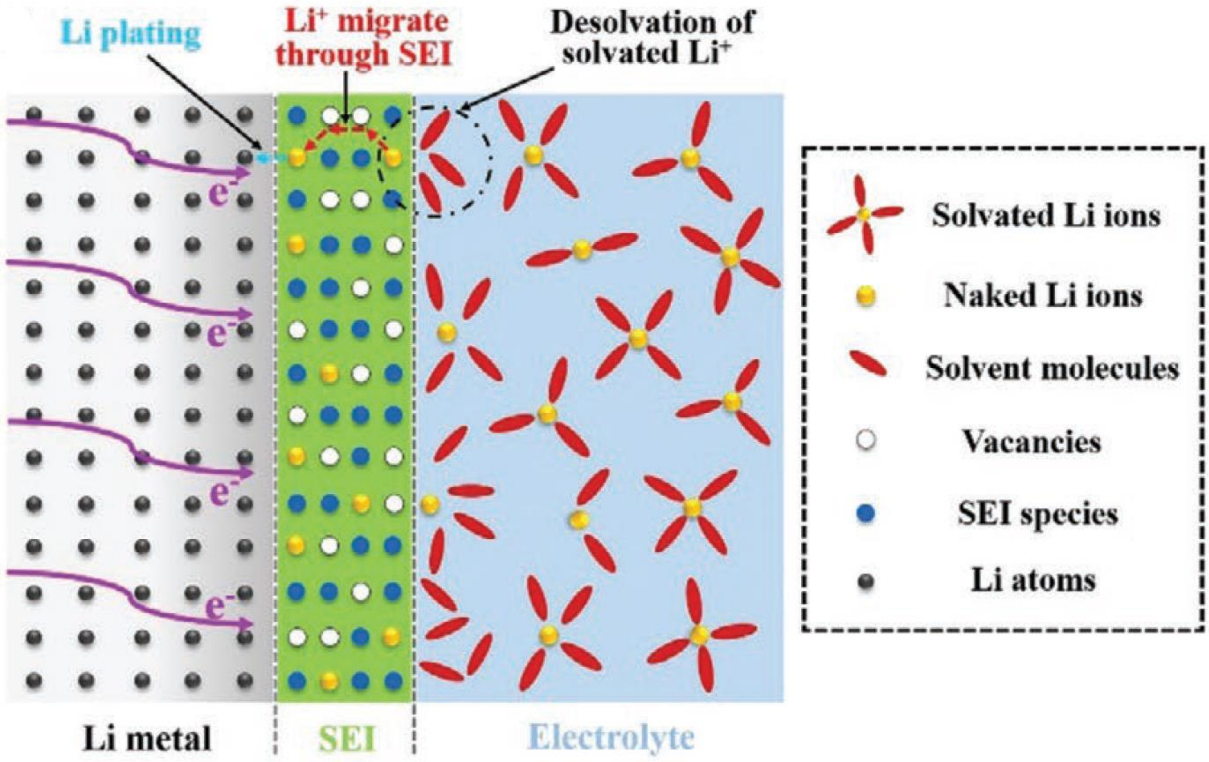

Figure 1.4 Schematic illustration of Li-ion diffusion from electrolyte to the anode[26].

1.4 Current collector design for LMB

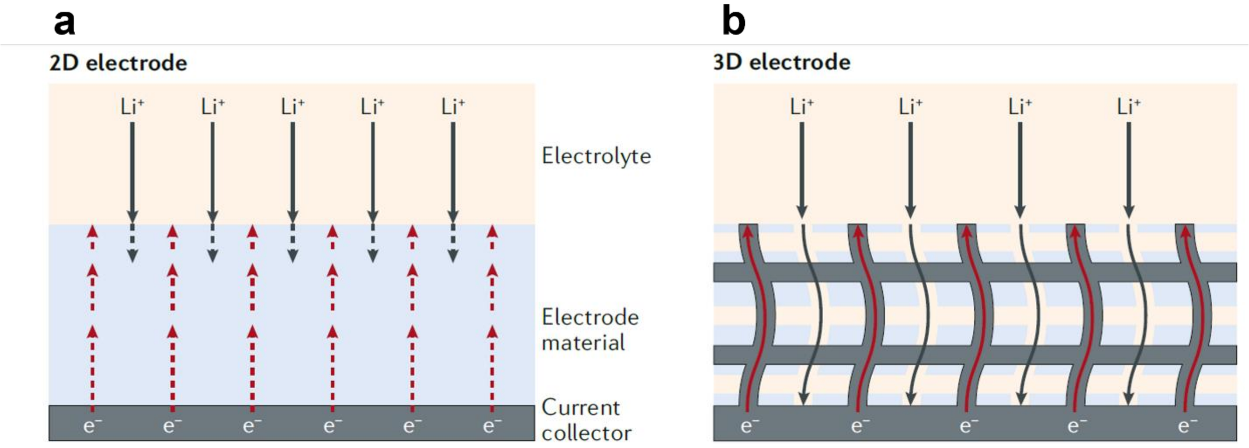

Figure 1.5 The working principles of 3D current collectors: a) The charge transport pathways in a conventional electrode with a 2D current collector show a limited charge penetration depth. b) The charge transport pathways in a 3D thick electrode show efficient charge delivery throughout the entire electrode thickness[27].

Another approach is the engineering of the current collector. The goal of designing a Li host, such as three-dimensional (3D) current collectors, is to constrain the growth of Li and lower the local current density, which would in turn suppress the growth of dendrite and mitigate the volume change during cycling (**Fig 1.5**)[28,29]. The materials that used for making a Li host need to be electronically conducting and electrochemically stable, insuring that no side reaction would happen during cycling[30]. Therefore, the choice of the materials is limited to metals and carbons. Lithiophilic materials such as reduced graphene oxide has been proven to be excellent host for lithium[30]. By simply dipping reduced graphene oxide sponge into molten Li, Li could be easily infused into the sponge by capillary force and ready to be used as battery anode[30]. Constructing hollow carbon structures as Li hosts is also a popular method[31,32]. Carbon nanospheres embedded with gold nanoparticles are designed for hosting Li[31]. The low nucleation barrier of Li on gold makes gold a good candidate for guiding the growth of Li. By implanting gold nanoparticles inside the carbon nanospheres, Li would first grow onto the gold nanoparticles during the plating process, and the carbon spheres can act as hosts to block the continuous formation of SEI[31]. Another way to construct 3D current collectors is through dealloying[29]. Brass is an alloy of zinc and copper. By removing zinc from brass tape via acid corrosion, a copper 3D current collector is constructed, and can provide a better Li deposition morphology than 2D copper foil current collector[29].

1.5 The practical use of LMB

The fast progress on prolonging the cycle life of LMB has laid the foundation for the practical application of this new generation battery. In order to realize the commercial adoption of LMB, several more concerns, such as low calendar life and safety properties, need to be addressed.

1.5.1 Calendar life of LMB

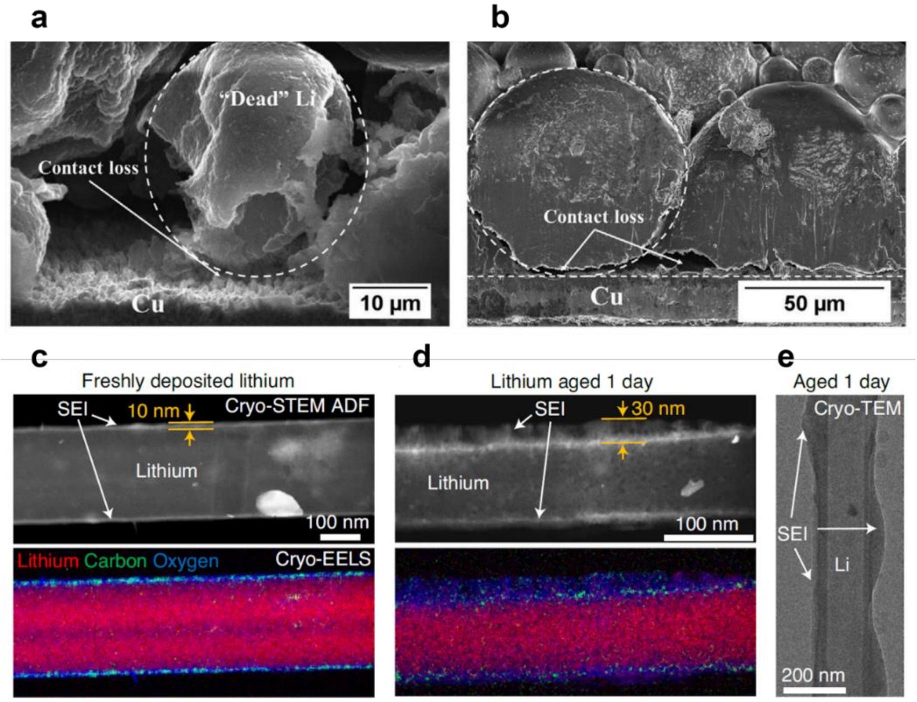

Figure 1.6 The galvanic corrosion of Li metal: a-b) Li particles are isolated from the Cu due to galvanic corrosion[33]. c) cryo-STEM ADF image and EELS map of freshly deposited Li and d) Li aged for 24 hours in electrolyte. e) Bright-field TEM image of a Li filament after calendar ageing in electrolyte[34].

The lifetime of a battery system depends on two separate parts: 1) calendar life, the degradation over storage time and 2) cycle life, the degradation over charge-discharge cycles[35]. Although a large amount of study has been done trying to extend the cycle life of LMB, so far only limited works have explicitly explored the calendar life of Li metal batteries, and the key parameters in controlling that. In the LMB systems, where Li metal is used as the anode, Li metal corrosion by the liquid electrolyte can cause a huge issue of active inventory loss when stored for an extended time[36,37]. The corrosion of metal is usually accompanied by the generation of a passivating layer (SEI in Li metal's case) which can stop the continuous oxidization of the metal[38]. Therefore, it is crucial for the field to study the corrosion process of the Li metal in liquid electrolyte and the propose a mitigation plan to prolong the calendar life of LMB.

Several works have studied the galvanic corrosion of Li metal that takes place when the interface between Li metal and current collector is exposed to the liquid electrolyte[33,39]. The morphological change of the Li powders is studied in a case where Li is directly casted onto the Cu current collector and rested in liquid electrolyte[33]. There is a continuous loss of the Li near the Li||Cu interface, which is believed to be caused by the Galvanic corrosion between Li and Cu (**Fig. 1.6a, b**). Furthermore, due to the inhomogeneity in the solubility and electronic conductivity of these SEI components[41], the continuous decomposition of the electrolyte is found to occur on the SEI surface, which is observed in the recent Cryo-STEM work[34], leading to the further corrosion of the Li metal even after the formation of the initial passivating (SEI) layer (**Fig. 1.6c, d**). These work shows that due to the highly reactive nature of Li metal, any surface of the Li that is exposed to the electrolyte will provide space for continuous exchange of electrons and matter, leading to the corrosion of Li metal. As a result of this continuous chemical/electrochemical corrosion, the Li metal anode will suffer from a loss of active Li^0 inventory, the formation of thicker interphase, and a poor cycling/storage life, which will eventually lead to the failure of the cell. Therefore, it is crucial that the interface of the Li is strictly controlled when designing a secondary battery system so that lifetime of it is not limited by its calendar life. Thus, more work focuses on exploring the parameters that are controlling the rate of the chemical/electrochemical corrosion of Li metal in the liquid electrolyte during the extended storage period needs to be done and propose mitigation plans to extend the calendar life of the rechargeable LMB.

1.5.2 Safety properties of LMB

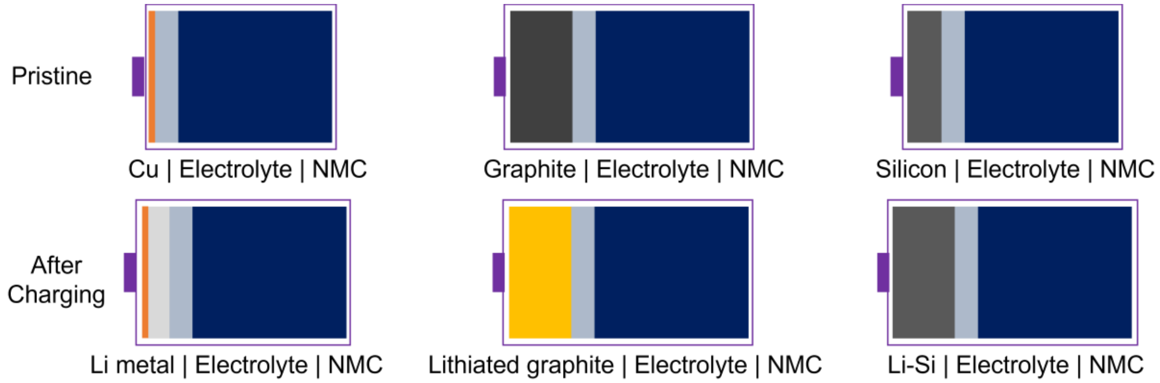

Figure 1.7 The comparison of the cell formats between different anode materials before and after charging process.

Another potential drawback of LMB is its safety properties. Due to the highly reactive nature of Li metal, LMB has long being considered to be more dangerous when compared to other Li anode materials such Graphite (Gr) and Silicon (Si). However, the fair comparison should be made between Li metal, lithiated Gr (Li-Gr) and lithiated Si (Li-Si), which are the actual anode material used in the battery (**Fig. 1.7**). As for commercial Li-ion battery, there has been tremendous work studying the key factors in determining the reactivity of Li-Gr[42–44]. By employing accelerating rate calorimetry (ARC) and X-ray diffraction (XRD), it is discovered that the lithiated Gr ($Li_{0.81}C_6$) starts to decompose with electrolyte at temperatures as low as 90°C, which leads to the release of heat[45]. Based on the results, it can be seen that the Li-Gr at charged state is far from a safe and stable material[46–48].

As a highly reactive alkali metal, Li has always been considered unsafe for practical battery operations. Various solutions have been proposed to design a safe rechargeable Li metal cell and most of them are focusing on the design of non-flammable electrolytes[49–51]. For example, fire-retarding localized high concentration electrolytes (LHCEs) have also been developed using non-flammable solvents, such as trimethyl phosphate or 2,2,2-trifluoroethyl-1,1,2,2-tetrafluoroethyl ether (HFE)[52,53]. These new electrolytes can provide extraordinary performance to the Li metal while retain from catching on fire. However, a new study recently claims that the LMB full cell with non-flammable electrolyte shows worse safety properties when compared to commercial carbonate-based electrolytes[54]. Although the fire-retardant solvent can prevent the electrolyte from ignition, the interaction between the salt and charged cathode will cause catastrophic reaction at elevated temperature, leading to the failure of the cell. Therefore, it is crucial to fully understand the synergetic effects between all cell components when designing a safe LMB. More work needs to be done to identify the key parameters in controlling the reactivity of Li metal and how that is going to affect the full cell safety properties.

1.6 Outlines

To further prolong the cycle life of Lithium metal anode, first, in **Chapter 2**, a new type of porous copper is designed as the current collector for Li metal anode. X-ray microscale computed tomography (micro-CT) allows us to assess the surface area, the pore size, and the tortuosity factor of the porous copper materials. A metallic Zn coating is also applied to study the influence of surface chemistry on the performance of the 3D current collectors. The effects of these parameters on the performance are studied in detail through scanning electron microscopy (SEM) and titration gas chromatography (TGC). Stochastic simulations further allowed us to interpret the role of the tortuosity factor in lithiation. The optimal range of the key parameters is thereby found for the porous coppers and their performance is predicted. Furthermore, the effect of external stack pressure on the Li metal plating process is studied in **Chapter 3**. A dense Li deposition (99.49% electrode density) with an ideal columnar structure that is demonstrated by controlling the uniaxial stack pressure during battery operation. Using multiscale characterization and simulation, the critical role of stack pressure on Li nucleation, growth and dissolution processes is discussed and a Li-reservoir-testing protocol is proposed to maintain the ideal Li morphology during extended cycling.

To understand the inventory loss of Li metal during the storage period, in **Chapter 4**, the chemical corrosion of Li metal in liquid electrolytes is quantitatively understood. By combing the titration gas chromatography method and cryogenic focused ion beam, a quantitative relationship between the chemical corrosion rate and electrochemically deposited Li morphology in various liquid electrolyte systems is established. It has been identified that the corrosion rate is dominated by the porosity of the deposited Li. The larger the porosity of deposited Li has, the faster the corrosion rate will be. Strategies to mitigate the chemical corrosion on Li thus to extend the calendar life of Li-metal batteries are further proposed.

Lastly, the safety properties of the LMB are systematically analyzed in **Chapter 5**. Differential scanning calorimetry (DSC) with in situ Fourier-transform infrared spectroscopy (FTIR) are used to quantitatively investigate the Li metal reactivity. Lithiated graphite (Li-Gr) and lithiated silicon (Li-Si) are also studied as the comparison samples. The reactivity of the plated Li when coupled with different electrolyte composition, morphology, cycle number, and atmosphere is systematically studied. More importantly, the reactivity of Li metal full cell with different cathode materials (NMC 622, LFP and LNMO) has been compared.

Chapter 2 Quantitatively Designing Porous Copper Current Collectors for Lithium Metal Anodes

2.1 Introduction

With a high theoretical capacity (3,860 mAh/g, or 2,061 mAh/cm^3) and low electrochemical potential (–3.04 V versus the standard hydrogen electrode), lithium metal is considered as the ideal candidate for the next generation battery anodes.[3] In fact, the lithium metal anode is a key component of next-generation high-energy-density battery systems such as lithium-sulfur and lithium-oxygen batteries.[4] However, there are many obstacles that need to be solved before lithium metal anodes can be effectively used in commercial cells. The fundamental problem lies in the formation of lithium whiskers during plating, which eventually leads to the formation of inactive lithium after cycling.[6] As a result, the lithium metal anode suffers from low CE and low cyclability.

Numerous methods have been proposed to mitigate the lithium whisker formation issue and improve the cyclability of lithium metal anode. One of the most promising methods to achieve this is through the engineering of the electrolyte,[9] such as adding additives,[11,12,23] using high lithium salt concentration[13,14,57] and localizing high lithium-salt concentration.[16–18] The main working principle of a high-performance electrolyte is to construct a homogeneous SEI layer and to provide a uniform lithium ion flux during the plating process so that a smooth and dense morphology can be achieved.[5] Another emerging method is the engineering of current collectors. The current collectors play a crucial role in the performance of a lithium metal battery cell. Planar Cu foils have been used as the anode current collector for decades because of their electrochemical stability against lithium.[58] However, under practical current densities, due to the inhomogeneous lithium-ion flux, lithium whiskers can easily form on the planar Cu foils during cycling.[59]

Therefore, a new current collector that can regulate the local current density and provide a uniform lithium ion flux is desired for lithium metal anodes.[58, 60,61] A variety of 3D current collectors have been designed to achieve this purpose.[28,31,32,62–67]

For a high-performance 3D current collector, there are three key parameters that need to be carefully designed: surface area, tortuosity factor and surface chemistry.[68] However, these three parameters are correlated with each other, and often one cannot be altered without disrupting the other two. Several works have mentioned the effects of these key parameters on the performance of the 3D current collectors.[29, 69] Yun *et al.* discovered that by tuning the dealloying time of brass foil, the resulting copper foil would have different pore sizes and surface areas, which would eventually lead to different performance of the dealloyed copper foils.[29] Similarly, by tuning the Cu pillar size and spacing, Chen *et al.* were able to study the effects of surface area and pillar spacing on the CE of the Cu pillar current collector and found the best combination for the performance.[69] Therefore, there is no doubt that surface area, tortuosity factor, and surface chemistry play crucial roles in determining the performance of the 3D current collectors. However, quantitative analysis of these key parameters is required when designing a new 3D current collector system.

In the present work, 3D porous Cu current collectors were fabricated by etching Fe from Cu-Fe composites with different compositions. The physical properties of current collectors were then quantified using laboratory micro-CT,[70,71] and their performance was predicted in terms of surface areas, tortuosity factors and surface chemistry. The quantitative study suggested that the high surface area was not as beneficial as previously believed[72, 73] and that the tortuosity factor should always be kept at a minimum. The high performance can only be achieved in a system when the three key parameters are in its optimal range. The prediction of the performance was also validated by Titration Gas Chromatography (TGC)[74] and electrochemical testing.

2.2 Methods

2.2.1 Synthesis of the porous copper networks

Pure Cu powders (Fisher Scientific, electrolytic powder) and pure Fe powder (Beantown Chemical, -325 mesh, reduced, 98%) were used to prepare Cu-Fe precursor ingots with three different compositions**:** 10 atomic percent (at%) Cu-90at%Fe, 20at%Cu-80at%Fe, and 30at%Cu-70at%Fe. The average powder size of both powders was about 30 microns. A hydraulic press was used to make pellets of 1 cm in diameter for each composition. These pellets were then arc melted five times to make homogeneous ingots with high cooling rates. In addition, the 30at%Cu-70at%Fe was loaded in a 3cm-diameter alumina crucible and heated in an Ar-filled furnace at 1550 ˚C for 1 hour, followed by slow cooling down to room temperature. The four different types of samples were sliced and polished using sandpaper to make samples 1 cm in diameter and 200 microns in thickness. These four samples are denoted throughout this paper as 10Arc, 20Arc, 30Arc and 30Furnace, in accordance with their composition and synthesis method.

After the Cu-Fe ingots were successfully synthesized, the disk was then etched in 5wt% H_2SO_4 acid solution at 90˚C under constant stirring for 24 hours. The acid solution was changed every 8 hours to prevent the accumulation of contaminants. The etched sample was then cleaned in 5wt% HCl solution under sonication for 15 minutes. This was followed by an acetone wash under sonication for 15minute to wash away any leftover contaminants. Finally, the cleaned samples were dried under vacuum for one hour.

2.2.2 Zn electrodeposition

The 20Arc Cu sample was Zn-coated using an electrolyte of 0.05 M $ZnSO_4$ +0.3M H_3BO_3 and the 30Furnace Cu sample was Zn-coated using an electrolyte of 0.01 M $ZnSO_4$ +0.3M H_3BO_3. In both cases, a small amount of 1M H_2SO_4 was added to adjust the pH to 1-2. The cleaned porous Cu was removed from the glovebox and used as the working electrode in a three-electrode set up where the counter electrode was platinum foil and the reference electrode was Ag/AgCl in KCl. A current density of 1mA/cm^2 was used to deposit Zn for 10 min and 5 min for the 30Furnace and 20Arc, respectively. The area used for the deposition current density was the measured effective surface area. The sample was then washed with deionized water and acetone and then dried under vacuum for one hour.

2.2.3 Electrochemistry

CR2016-type coin cells were assembled in an Ar-filled glove box for electrochemical characterization. The electrolyte consisted of 75 µL of 1 M lithium bis(trifluoromethane sulfonyl)imide (LiTFSI) in a mixed solvent of 1,3-dioxolane (DOL) and 1,2-dimethoxyethane (DME) (1:1 in volume) with 2% $LiNO_3$ and Li metal foil was used as the counter electrode. A range of current density was used during lithium plating morphology study. For all CE testing, at least three cells were tested at the same condition and the average CE is calculated.

2.2.4 Scanning Electron Microscope (SEM) / Energy Dispersive X-ray Spectroscopy (EDS)

A FEI Apreo SEM was used to study the structure of the as-prepared porous copper current collector as well as the morphology of the electrochemically deposited lithium (EDLi). EDS was used to characterize the elemental composition of the sample.

2.2.5 Micro-CT

The samples were individually punched into films with a 2 mm radius piece and were stacked in a PTFE cylindrical tube with alternating PTFE films to provide separation. Two scans were conducted using a ZEISS Xradia 510 Versa micro-CT instrument. The first scan was conducted on the lager pore samples (30Furnance and 10Arc, shown in **Fig 2.1c-d**) and had a voxel size of 1.07 µm and an exposure of 4 seconds. The second scan was used to examine the smaller pore samples (20Arc and 30Arc, shown in **Fig 2.1a-b**) and had a voxel size of .7834 µm and an exposure of 6 seconds. Both scans were conducted with 1801 projections at an X-ray energy of 140 keV with a 71.3 uA current using a high energy filter at a 4X magnification. The beam hardening constant for the reconstruction was 0 and 0.6 for the first and second scan respectively. Post measurement analysis was performed by the Amira-Avizo method using the Deblur, Delineate, and Median Filter modules for data sharpening and filtration provided by the software. The Separate Objects module, which utilizes a distance map and a watershed algorithm, was used to define 3D pores and determine the overall distribution of the pore sizes. The tortuosity factor was determined for each of the resulting structures using the software TauFactor[75] and cross-validated with GeoDict, both relying on Fickian diffusion.

Simulation of the Li deposition process in the porous copper made use of an *in house* MATLAB-based stochastic algorithm. For a given capacity, the volume of deposited Li was determined considering 100 % coulombic efficiency and a molar volume of 13.02×10^{-6} m^3/mol. Then, this volume was converted into a number of pixels. Subsequently, pixels of void in contact with solid phase (Cu or Li) were converted into pixels of Li until the desired amount was achieved. To mimic the experimental observations, a percentage of the Li was deposited on the top of the copper support (see Table S1). We arbitrarily allowed for an extra 15 µm thick void to be inserted on top of the current collector for Li deposition. After Li deposition, the remaining empty thickness was removed from this extra 15 μm space in order to limit its impact on the tortuosity factor calculation. Additionally, to account for the heterogeneous deposition of Li along the thickness, an arbitrary gradient has been applied to replicate the experimental observations. Each structure was divided into 6 equal sub-volumes for which the deposited Li amount is reported in Table S2. Then the algorithm called the software TauFactor[75] to determine the tortuosity factors of each porous copper network. Each condition was repeated between 5 and 10 times to quantify the uncertainty linked to the stochastic method.

2.2.6 Titration Gas Chromatography (TGC)

The TGC method was used to quantify the amount of inactive metallic lithium formed in the porous copper after cycling. After plating and stripping of Li, the porous Cu electrode was recovered from the coin cell; the porous copper film, including any residual inactive lithium, together with the separator, was put into a 30 mL bottle without washing. The bottle was then sealed with a rubber stopper and the internal pressure of the bottle was adjusted to 1 atm. After the bottle was removed from the glovebox, excess deionized (DI) water (0.5 mL) was injected into the bottle to react with any residual inactive metallic lithium to form H_2 gas. The vial was then well mixed by shaking, and a gas-tight syringe was used to quickly take 30 μL of the gas from the head-space of the sealed bottle. The gas was then injected into a Nexis GC-2030 Gas Chromatograph (Shimadzu) for H_2 quantification. A pre-established H_2 calibration curve was used to calculate the amount of inactive metallic lithium from the measured H_2 peak area. The mass of inactive metallic lithium in the porous copper films was directly related to the amount of H_2.

2.2.7 X-Ray Diffraction (XRD)

XRD was performed using a PANalytical X'Pert Pro powder diffractometer operating with Cu Kα radiation (λ = 1.5418 Å) using a 0.03° step size, a voltage of 45 kV, and a current of 40 mA. XRD patterns were recorded in the range of $15° < 2\theta < 85°$.

2.2.8 X-Ray Photo-electron Spectroscopy (XPS)

XPS analysis was performed using a Kratos Axis Ultra DLD spectrometer with a monochromatic Al (Kα) radiation source. A charge neutralizer filament was used to control charging of the sample. A 20 eV pass energy was used with a 0.1 eV step size; scans were calibrated using adventitious carbon by setting the C 1s peak to 284.8 eV. Samples were etched with an Ar beam with a raster size of 2mm x 2mm at an energy of 4 kV for 1 minute.

2.3 Result and Discussion

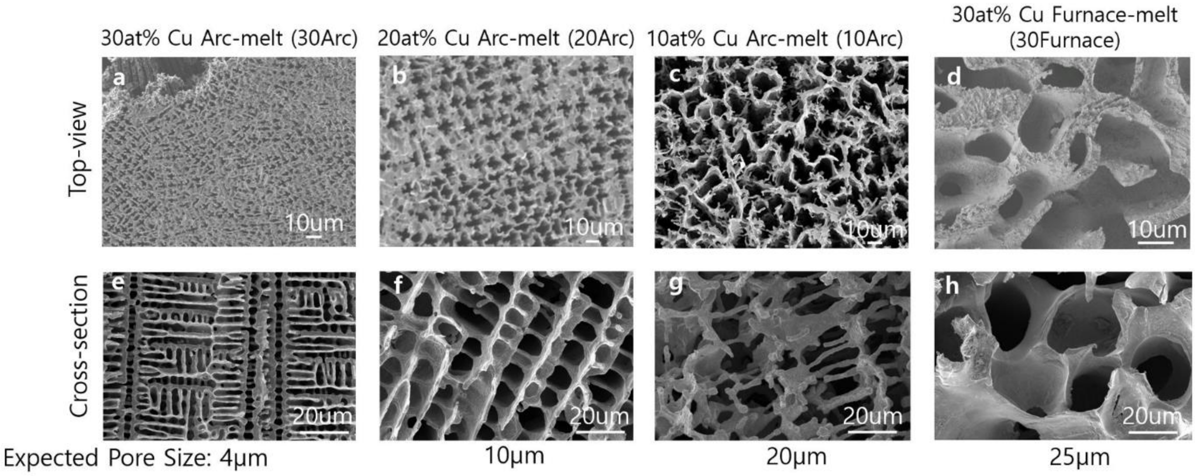

Figure 2.1 SEM images of the four porous copper films used in this work. a) Top-view and e) cross-section of the 30 at% Cu arc-melted (30Arc) sample; b) top-view and f) cross-section of the 20 at% Cu arc-melted (20Arc) sample; c) top-view and g) cross-section of the 10 at% Cu arc-melted (10Arc) sample; d) top-view and h) cross-section of the 30 at% Cu furnace-melted (30Furnace) sample.

Porous copper films with interconnected channels were fabricated by etching Fe from Cu-Fe composites. Ingots with compositions of 10, 20 and 30 atomic percentage (at%) Cu were made by arc melting and one ingot with a composition of 30 at% Cu was made using a conventional Ar-filled furnace. Arc melting involves rapid heating and rapid cooling, while heating and cooling rates in a conventional furnace are much longer. Because Cu and Fe are essentially immiscible in the solid state but fully miscible in the melt, the size of the phase separated domains that form upon solidification is strongly dependent on the cooling rate, with faster cooling of the arc furnace producing smaller domains. For a given cooling rate, the size of domains can be further tuned using the atomic percentage of Cu and Fe with higher Fe fractions resulting in large Fe domains. Because the Fe is the fraction that is etched form the ingot, both larger Fe fractions and slower cooling rates result in larger pore in the remaining Cu. After careful etching and cleaning, porous coppers with different well-structured channels were fabricated. (**Fig. 2.1**). However, there is no Fe or S remaining in the samples. Unlike other randomly structured porous copper that were also synthesized by dealloying method,[29] the porous copper networks derived from Cu-Fe composites show homogeneous, large pored micro-structures that allow us to quantitatively analyze the effects of key parameters such as surface area and tortuosity factor on the performance of a 3D current collector.

As shown in **Fig. 2.1a** and **2.1e**, when 30 at% Cu was mixed with Fe and arc with rapid heating and cooling, the resulting porous copper had roughly 4µm-wide and 10µm-long channels, which provided empty spaces for lithium to deposit. As the Cu at% decreased in the precursor, the channels in the final porous Cu grew longer and wider. The 10 at% Arc melt porous copper showed approximately 20µm-wide channels (**Fig. 2.1c, 2.1g**), but the structure of the channels was very fragile. Therefore, a second melting technique was used when synthesizing the 25µm-wide porous copper, which involved slow heating and cooling an ingot with 30 at% Cu using an Ar-filled furnace. The resulting porous copper showed 25µm-wide pores with sturdy ligaments.

The physical parameters of the porous copper samples were quantified by laboratory X-ray micro-CT. Each piece of the porous copper was punched and fitted into a sample holder tube. With voxel size of 0.7834 µm or 1.07 µm, the 3D structures (**Fig. 2.2a, 2.2b**) of the porous coppers obtained through the tomography was analyzed using the Amira-Avizo software package and the physical properties of the porous coppers were measured (**Fig. 2.2**).

Fig. 2.2d reports the pore size distribution of each porous copper sample. As expected, the 30Furnace sample shows the largest pores and the 30Arc sample had the smallest pores, followed by 20Arc and 10Arc. The peak of each histogram curve represents the average length of the micro-channels in the porous copper. The results match well with the SEM images shown in **Fig. 2.1** except for the 30Arc sample. For the 30Arc samples, the pores are in a narrow but long channel-like structure. The expected pore size measured from the SEM images is around 4 um. However, in the MicroCT measurement, the pore size is defined as the diagonal length of the pores, so the both the diameter and the length of the channel-like pores are included in the pore size calculation. Therefore, in the **Fig. 2.2d**, the pore size of 30Arc centers around 10 um instead of 4 um. The geometric tortuosity values in **Fig. 2e** were calculated based on the average length a fictive particle needs to travel to go through the whole porous copper sample in the z-direction, which approximately quantifies how easy it is for a lithium ion to diffuse and electro-migrate inside the Cu network during an electrochemical plating process. Both the 10Arc and 30Furnace samples have relatively low geometric tortuosity because they have large enough pores for lithium ion to move freely without many obstacles in the z-direction. The volumetric surface area of each porous network can be directly obtained from the 3D tomography (**Fig. 2.2c**). The effective surface area was calculated based on the actual size of the electrode used in the electrochemical testing (7 mm in diameter and 200 µm in thickness). In the surface area measurement, the same trend is observed as in the geometric tortuosity: the samples with smallest pore sizes have the largest effective surface area while the larger pores give the smallest surface areas. There is a slow drop of effective surface area from the 20Arc to 10Arc materials, despite the fact that the pore size difference in these two samples is large. This is caused by the change of ligament size as the at% of Cu in the precursor ingot decreases from 20 to 10 (**Fig. 2.1f, 2.1g**). The thinner ligament contributes to the extra surface area in the 10Arc sample. With these key physical parameters quantified, the effects of morphology and the distribution of deposited Li can now be studied in detail.

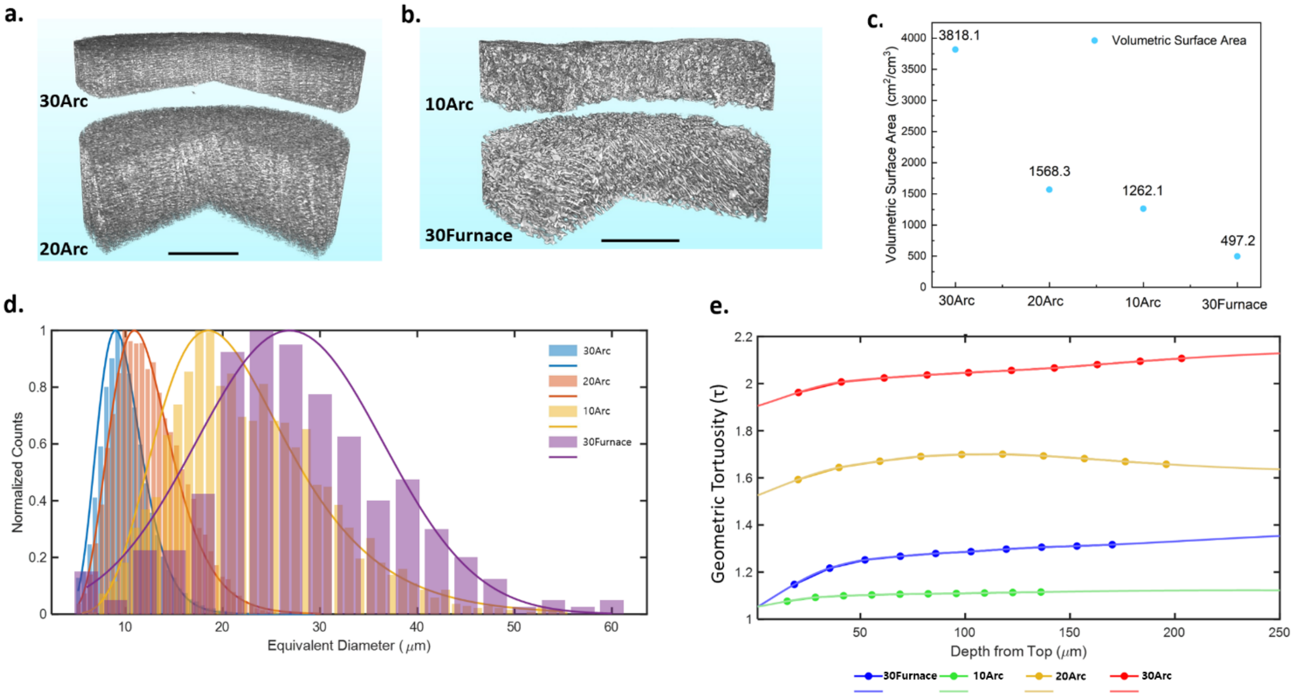

Figure 2.2 Quantification of the physical parameters of the porous copper:a) The 3D tomography of 30Arc and 20Arc with voxel size of 0.7834 μm. b) The 3D tomography of 10Arc and 30Furnace with voxel size of 1.07 μm. For both parts a) and b), the scale bar is 200 μm. c) Volumetric surface area in the porous copper; d) Histograms of the pore size distribution for each porous copper sample. e) Geometric tortuosity of the porous copper as a function of depth.

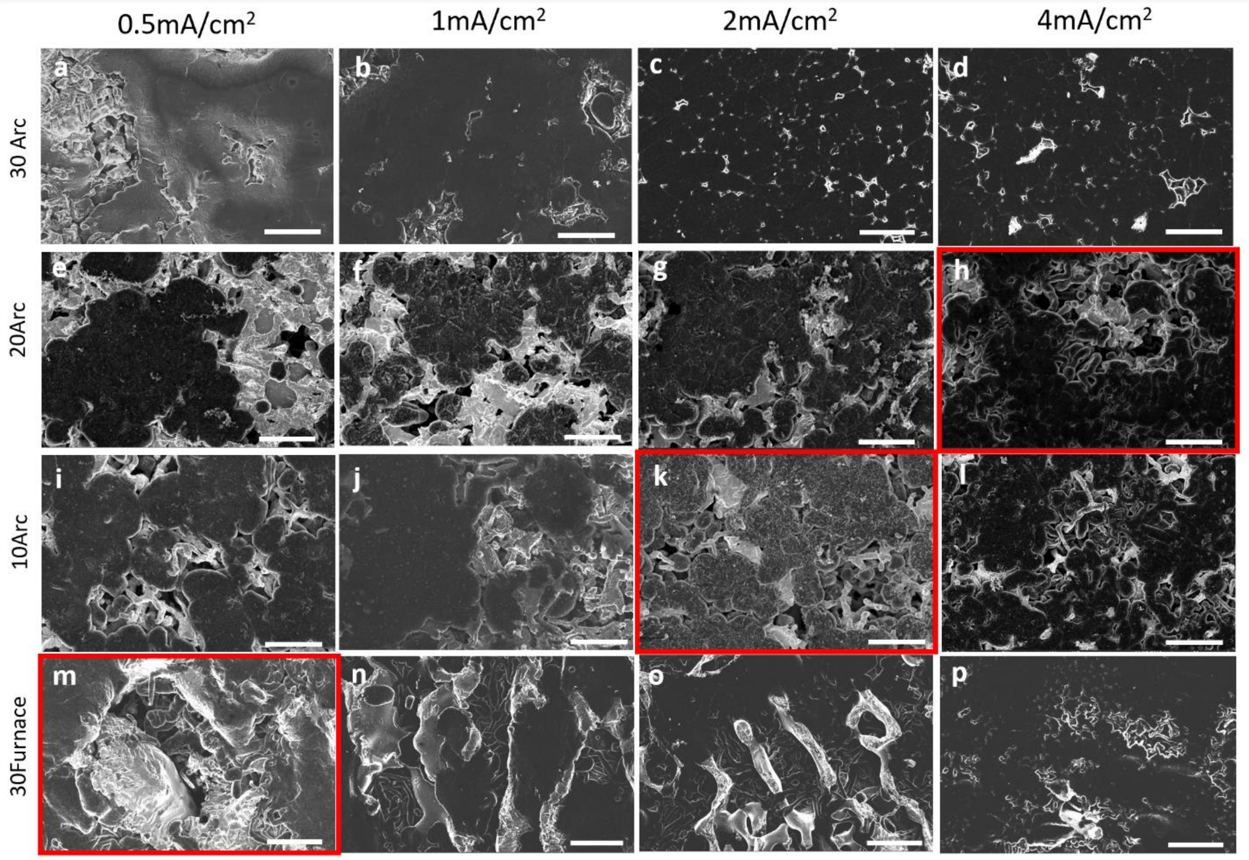

Figure 2.3 Top-view SEM images of the morphology of lithium plated under different current densities onto the porous copper networks with different pore sizes: a-d) 30Arc; e-h) 20Arc; i-l) 10Arc; m-p) 30Furnace. Current densities are indicated on the figure. The critical current densities at which lithium whiskers start to grow are marked with red boxes. All samples were plated to 4 mAh/cm^2 before imaging. The scale bars in all images correspond to 20 μm.

The effect of the surface area on the morphology of the deposited lithium was characterized using top-view SEM images. For each sample, 4 mAh/cm^2 of lithium was plated onto the porous copper using 4 different current densities, each of which are indicated in **Fig. 2.3**. As the surface area decreases with the increase of pore size, the effective local current density per unit surface area of Cu would also increases. It is widely accepted that high local current densities can lead to an inhomogeneous flux of lithium ions during plating, causing the formation of lithium whiskers.[60] By studying the lithium deposition morphology on the porous Cu networks with different surface areas under a range of current densities, the critical current density at which lithium whiskers begins to grow in each sample can be determined.

With the largest effective surface area, which is 29.49 cm^2 in a piece with 0.7 cm diameter and 200 μm thickness, the 30Arc samples produces a dense and smooth lithium deposition morphology throughout the four current densities tested. As the effective surface area decreased to 12.03 cm^2, the 20Arc samples also show relatively dense morphology in most of the current densities tested except at 4 mA/cm^2, which is indicated by the red box in **Fig. 2.3h**. At this current density, lithium whiskers begin to grow on the surface of the pore channels, which means that the local current density becomes too high, inducing inhomogeneous lithium ions transport. As the effective surface area is further decreased, the critical current density also decreased. In the 30Furnace sample, where the effective surface area was only 3.76 cm^2, lithium whiskers were observed at current densities as low as 0.5 mA/cm^2, which means the critical current density might be even lower than that. Based on these observations alone, it seems that the higher the surface area in the porous copper, the better the Li morphology.

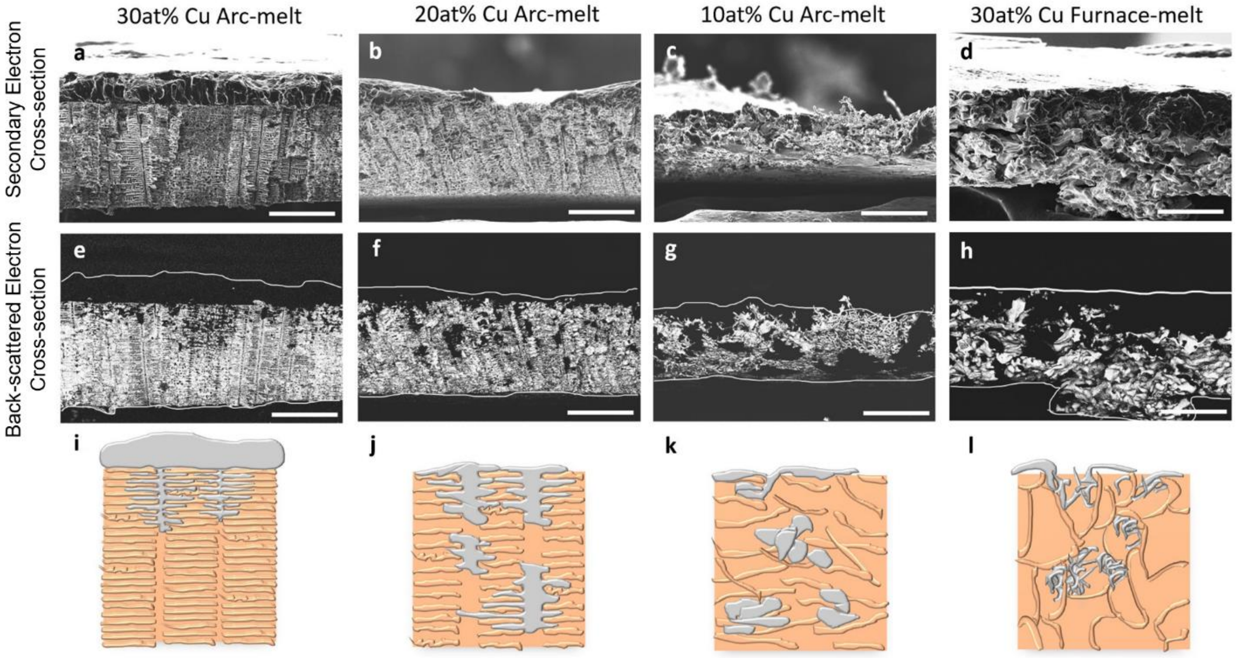

Figure 2.4 Cross-sectional SEM images of the morphology of lithium plated into the porous copper networks with different pore sizes: a-d) Cross-sectional secondary electron SEM images, e-h) back-scattered electron SEM images and i-l) cartoon illustrations of the observed lithium spatial distribution in the cross-section of each porous Cu sample. All samples were plated to 20 mAh/ cm^2. The scale bars in all images correspond to 50 µm.

The effect of the geometric tortuosity and pore size of the porous Cu network on the deposited lithium morphology was studied by cross-sectional SEM images. **Fig. 2.4** shows the distribution of deposited lithium in each porous Cu sample after plating for 20 hours at 1 mA/cm^2. Back-scattered electron (BSE) images (**Fig. 2.4e-h**) give a clear view of how lithium is distributed across the whole porous copper network: the brighter region is copper, the darker region is lithium, and the boundary between vacuum and lithium is marked by white lines. Cartoon schemes were also constructed to better illustrate the observed lithium deposition distribution and morphology in the different porous copper samples (**Fig. 2.4i-l**).

With the smallest pore diameter (~4 µm) and the highest z-directional geometric tortuosity (1.35), the 30Arc samples gave the most inhomogeneous distribution of the deposited lithium within the volume (**Fig. 2.4a, 2.4e, 2.4i**). Most of the deposited lithium accumulated on the top surface on the porous copper, and the space inside the pores, where the lithium was supposed to deposit, was mostly empty. This inhomogeneous distribution of deposited lithium can be attributed to the complex structure of the porous copper, with small pores and high geometric tortuosity hampering lithium ions transport and accessibility to the majority of the structure pores. As we increased the pore size to ~10 µm, which led to a decrease in the z-directional geometric tortuosity to 1.28, the distribution of the deposited lithium in the porous copper changed dramatically (**Fig. 2.4b, 2.4f, 2.4j**). More lithium was deposited inside the pores of the Cu instead of on the top surface. The higher utilization of the empty pores increases the contact area between lithium and the copper, which should lower the local effective current density and result in a more uniform morphology. The further increase in the pore size (~20 µm) and the decrease in the geometric tortuosity (1.03) allowed more lithium to grow inside the pores (**Fig. 2.4c, 2.4g, 2.4k**). The deposited lithium grew in a bulky way and had a clustered morphology inside the porous Cu. In the largest porous Cu (~25 µm), the distribution of the deposited lithium was similar to that in the 10Arc sample. However, the increase of the pore size also led to a decrease of surface area. As a result, the morphology of the deposited lithium changed from bulky to whisker-like (**Fig. 2.4d, 2.4h, 2.4l**). This change of morphology should eventually lead to the formation of inactive metallic lithium and cause the decrease in coulombic efficiency.[6]

To gain further insights into the factors limiting Li deposition in these porous copper structures, a computational study focused on the tortuosity factor was carried out. Such a study was designed to capture the evolution of the tortuosity factor with the increase of Li deposition in the different porous Cu structures. The tomographic structure of each sample was imported into MATLAB and the full whole volume of each sample was used for the calculation. An *in-house* MATLAB®-based algorithm was then used for the stochastic generation of lithium deposited in each porous copper sample. This algorithm favored the deposition of lithium in aggregated form, since that is what was observed experimentally. To further match with the experimental observations, a given amount of lithium was allowed to deposit on the top of the porous Cu and a deposition gradient was applied along the depth from the top to the bottom. Then, the tortuosity factor was determined for each of the resulting structures using the software TauFactor,[75] which relies on Fickian diffusion. Because of the stochastic nature of the lithium deposition simulation, each simulation was repeated between 5 and 10 times to ensure reproducibility and sufficient statistics.

The tortuosity factor results are reported in **Fig. 2.5a** for each porous Cu samples as a function of the plated lithium capacity. It appears that the tortuosity factor follows a gentle exponential rise until a certain threshold where it sharply increases. The larger the pores, the higher the threshold capacity corresponding to the steep rise in the tortuosity factor. The 30Arc sample has the smallest pores, and as a result the tortuosity factor begins to increase rapidly at the lowest capacity for this sample (at around 6 mAh/cm^2). It is noteworthy that the 30Furnace sample shows a higher tortuosity factor than the 10Arc sample until a capacity of 7 mAh/cm^2, the reason for that has been discussed in the previous section. From the 3D images on **Fig. 2.5b**, the large pores of the two structures (10Arc and 30Furnace) do not look to be clogged with lithium at 4 mAh/cm^2. At low capacities, it thus seems that if the pores are large enough to accommodate the lithium deposition, the interconnectivity of the pores and the tortuosity of the empty pores will be the most important parameters. However, at 7 mAh/cm^2, the lithium deposits appear to be significantly denser. Indeed, beyond 7 mAh/cm^2 the 30Furnace structure displays a lower tortuosity factor which suggests that at higher capacities, the pores in the 3D structure might be filled and thus not able to accommodate more Li.

Based on the observations above, the effect of the tortuosity factor can be summarized as following. The narrow and tortuous structures, such as the case in the 30Arc sample, would largely hinder the transport of lithium ions, leading to an inhomogeneous distribution of the deposited lithium. The inhomogeneous distribution would also waste the empty space and surface area provided by the 3D structure and possibly lead to the formation of lithium whiskers after the top surface is fully covered by the deposited lithium. Therefore, as mentioned previously, an increase in surface area does not always lead to a more uniform morphology for the deposited lithium. The increase of surface area and the decrease of pore size can have competing effects. From the data presented here, it appears that the sample with high enough surface area to provide a uniform morphology for lithium deposited at various plating rates and with pore that are large enough to facilitate lithium ion transport is the 20Arc material. The material seems to be near the “sweet spot” in this porous copper system.

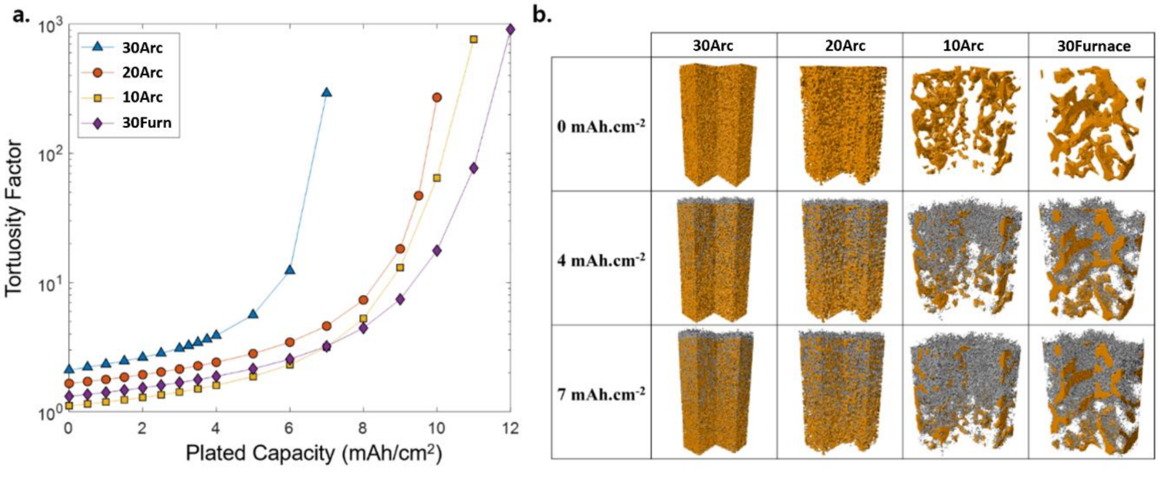

Figure 2.5 Simulation of the tortuosity evolution of the porous copper as Li plating continues: a) Tortuosity factor as a function of the capacity of Li plated into each porous copper structure; b) Porous coppers before (0 mAh/cm^2) and after (4 and 7 mAh/cm^2) Li deposition with the copper in gray and the Li in orange. The whole thickness of the current collectors is displayed with a square base of 100 µm of length. One quarter of each structure was removed for visualization-sake.

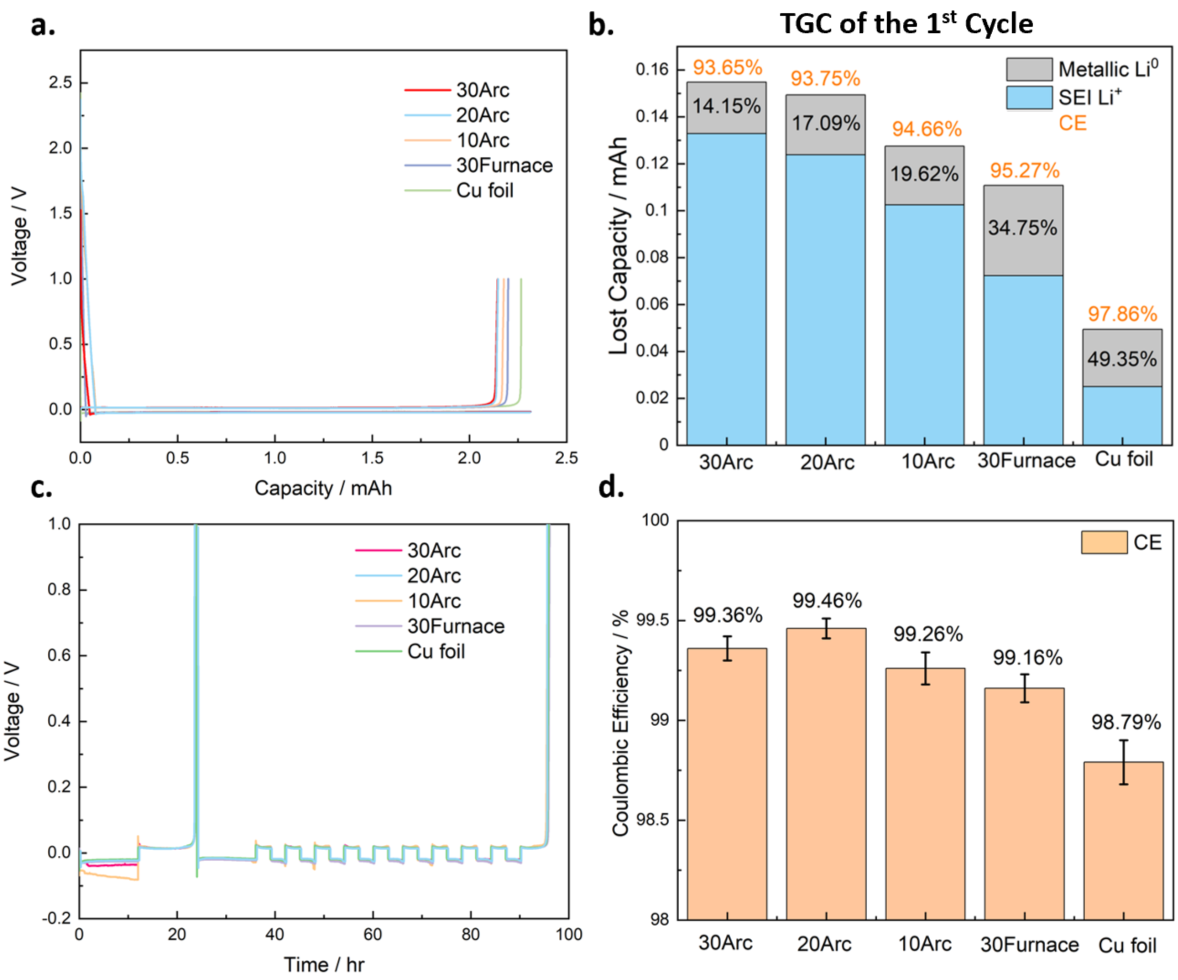

Figure 2.6 The electrochemical performance of the porous coppers: a) Electrochemical potential curve for lithium plating and stripping on each of the porous copper samples. b) TGC quantification of the SEI and inactive metallic lithium fractions for each sample. c) Electrochemical potential curve for CE testing for each porous copper sample. d) The calculated average CE of each porous copper sample from the half plating-stripping testing protocol.

To evaluate our prediction for the performance of the porous copper based on their physical parameters, Li||Cu cells were made to test the CE for lithium plating/stripping. The first cycle CE was calculated by plating 6mAh/cm^2 of lithium onto the porous coppers and stripping at 0.5mA/cm^2. After that, TGC was applied to quantify the amount of SEI Li$^+$ and inactive metallic Li^0 formed on the first cycle. In the TGC experiment, a fixed amount of deionized (DI) water was added to the cycled porous copper electrode, the inactive metallic lithium that was not removed during stripping will react with the DI water and release hydrogen gas. The amount the hydrogen gas quantified through gas chromatography can be directly correlated to the amount of the inactive metallic Li^0 left on the porous copper. It is known that CE values below 100% in each cycle of lithium plating/stripping comes from the combination of SEI Li^+ formation and formation of inactive metallic Li^0. By quantifying the fraction of inactive metallic Li^0, the SEI Li^+ can then be calculated from the CE, and the combination of both values can help us to understand the failure model of each porous copper sample.

As shown in **Fig. 2.6b**, the 30Arc samples showed the lowest CE on the first cycle, which was 93.65%. However, the amount of inactive metallic Li^0 formed was only 0.0219 mAh, which was only 14.15% of the total irreversible capacity, the lowest among the five types of coppers tested. The results show that although the high surface area of the 30Arc helped to improve the morphology of the deposited lithium, which is reflected in low percentage of inactive metallic Li^0, the high surface area also provided more contact surface between the electrolyte and lithium metal, which is thermodynamically unstable and leads to the formation of SEI under most conditions. In addition, during the first cycle due to the presence of CuO_x, Li would first react with this oxides layer and form SEI, which also contributes to the low CE. This is most prominently shown in the first cycle CE of the 30Arc sample, as it has the highest surface area. While the CuO_x is an issue only in the first cycle, the SEI in the high surface area samples remains a problem throughout cycles. For the 20Arc samples, with the decrease in surface area, the amount of SEI also decreased while the formation of inactive metallic Li^0 remained low. Therefore, an increase in CE was observed. As the surface area further decreased, the formation SEI also decreased in the 10Arc and 30Furnace samples. However, due to the low surface area of the 30Furnace samples, some lithium whiskers formed in these samples (**Fig. 2.3m**), increasing the fraction of inactive metallic Li^0. The sample with the highest CE in the first cycle is the 2D copper foil. The high CE in the copper foil comes from two reasons: 1) The low surface area of the copper foil limits the contact area between lithium and electrolyte and the amount of CuO_x that can form, thus leading to lower SEI formation; 2) The stack pressure on the copper foil from the coin cell also helped more lithium be stripped back to the electrolyte, whereas the stacking pressure inside porous copper was nearly zero, so the lithium can more easily detach from the copper substrate during stripping.

Based on the analysis above, it can be concluded that although the high surface area can help lithium to grow in a better morphology, the extra surface area also causes the formation of extra SEI. These competing factors led us to use a more representative way to determine the CE of the lithium plating/stripping. As shown in **Fig. 2.6c**, a half plating and stripping method was utilized to characterize the CE of the lithium plating/stripping. In this method, first, a full lithium plating/stripping cycle was performed to condition the surface of the coppers. Then, 6 mAh/cm^2 of lithium reservoir (Q_P) was plated onto the coppers at 0.5 mA/cm^2, followed by 9 cycles of striping and plating of 3 mAh/cm^2 of the lithium (Q_{half}). At the last step, all the remaining lithium was stripped to the cutoff voltage of 1V (Q_S). The average CE is calculated by $(9Q_{half} + Q_S)/(9Q_{half} + Q_P)\times100\%$. While the conventional CE testing method can tell us the efficiency of each cycle, it will include the capacity lost due to the formation of fresh SEI on cycle. The half plating and stripping technique leaves a layer of lithium reservoir after the first cycle, which can lead the lithium to fill back into the pre-existing SEI layer to minimize its formation. Furthermore, the first formation cycle has also consumed most of the oxides layer on the porous copper, leaving behind a relatively clean surface for Li metal deposition. Using this method, the average CE of the 30Arc, 20Arc, 10Arc, 30Furnace and copper foil was calculated to be 99.36%, 99.46%, 99.26%, 99.16% and 98.79% as shown in **Fig. 2.6d**. The preconditioning and the half plating and stripping technique greatly minimized the formation of SEI in each cycle and the CE is directly reflecting effect of the morphology and the distribution of the deposited lithium. As predicted earlier, the 20Arc shows the highest CE because of its relatively high surface area and also large pore size.

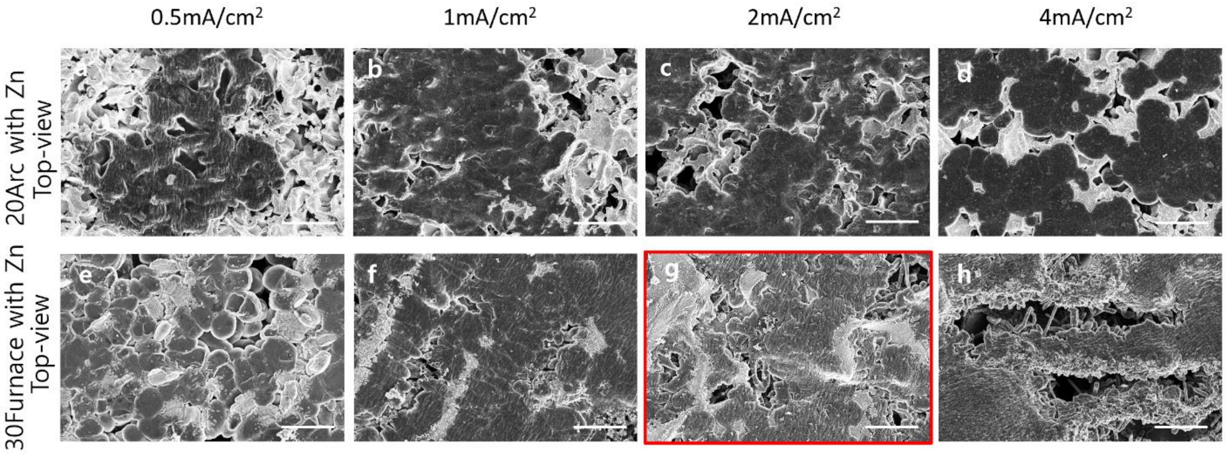

Figure 2.7 Top-view SEM images of the morphology of the lithium plated under different current density onto porous copper with a Zn coating. a-d) 20Arc sample coated with Zn; e-h) 30Furnace sample coated with Zn. The deposited Li is shown in darker contrast, while the brighter contrast shows the porous copper substrate. The critical current density at which lithium whiskers start to grow is marked with a red box. All samples were plated to 4mAh/cm^2. The scale bars in all images correspond to 20 µm.

The last parameter that can affect the performance of a 3D current collector is the surface chemistry. It is known that the electrochemical property of the substrate on which Li is plated can significantly influence the morphology of the Li.[31,62] To quantitatively explore how the improvement in surface chemistry can bring to the performance of the porous copper current collectors, metallic Zn, which has a lower nucleation barrier for Li than Cu,[31] was electrochemically coated onto 20Arc and 30Furnace samples. These two samples were chosen because they showed the best and the worst performance, respectively, based on the data presented above. Plating Zn inside of pores is not generally as easy as plating on top of a film, and indeed, in this case, the thickness of the Zn is greater on the top of the sample. While these interior thickness are much smaller than the overlayer on the top, they still provide nucleation sites for Li plating within the interior of the porous Cu.

To study the role of Zn coating, Li was electrochemically deposited onto the bare porous copper and Zn coated porous copper. The Li metal nucleation overpotential, which is defined as the voltage difference between the bottom of the voltage dip and the flat part of the voltage plateau, is a parameter that represents the energy barrier that Li needs to overcome to nucleate on the substrate.[31] The nucleation overpotentials of 20Arc and 20Arc with Zn are found to be 46.1 mV and 32.5 mV respectively, meaning that the Zn coating successfully lower the nucleation barrier of Li depositing on the substrate, which should potentially lead to a more uniform and dense morphology.

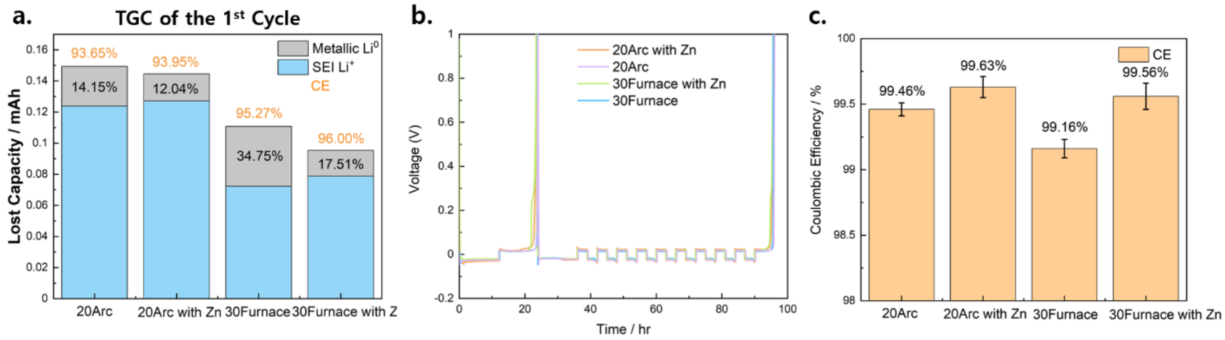

Figure 2.8 The electrochemical performance of Zn coated porous coppers: a) TGC analysis of the SEI and inactive metallic lithium; b) the electrochemical potential curve of CE testing of the porous copper samples; c) The calculated average CE of the Zn-coated porous copper sample from the half plating-stripping testing protocol.

The morphology of deposited Li on the Zn coated porous copper was then studied by SEM. As shown in **Fig. 2.7a-d**, the resulting Li morphology after plating in the 20Arc sample coated with Zn is dendrite free across the whole range of current density tested. This result stands in contrast to the uncoated 20Arc sample, where Li whiskers begin to appear at 4mA/cm^2. An even more dramatic improvement in Li morphology is observed in 30Furnace sample, however. As shown in **Fig. 2.7e-h**, the Li deposited Li on the 30Furnace sample coated with Zn shows a spherical morphology at 0.5 mA/cm^2. Even at this low current density, a whisker morphology was already seen in the uncoated samples. Li whiskers only begin to grow at a much higher current density of 2mA/cm^2.

The porous samples with Zn coatings were further tested for plating/stripping CE using the protocol mentioned previously. The 20Arc sample coated with Zn had an average CE of 99.63 %, which increased from 99.46 % of the uncoated samples, while the 30Furnace sample coated with Zn had a CE of 99.56 %, which increased from 99.16 % of the uncoated samples, as shown in **Fig. 2.8c**. The amount of SEI Li$^+$ and metallic Li^0 in the first cycled was again quantified using TGC (**Fig. 2.8a**). The first cycle CE of the 20Arc samples improved only by a small amount after coating because the lithium morphology in the 20Arc was already dense without the coating, and the surface area was not significantly changed by the coating so that the SEI formed from the reaction between Li and oxides layer did not change much. The absolute amount of inactive metallic Li^0 did markedly decrease, however, presumably because of more effective Li nucleation on the improved surface. This was partly offset by a slight increase in the SEI Li$^+$, likely because the Cu_4Zn is more reactive toward oxygen or water than pure Cu. A more significant improvement was observed in the 30Furnace after coating. The first cycle CE improved from 95.27 % to 96.00 %, while the amount of inactive metallic Li^0 also markedly decreased because of the improved morphology. Again, a slight increase in the SEI Li$^+$ was observed, but change was not large enough to offset the large gains from the reduction in inactive metallic Li^0 due to the improved plating onto the lithophilic surface. The decrease in the inactive metallic Li^0 and improved cycling performance was more obvious in the 30Furnace sample upon coating with Zn than in the 20Arc sample, which proved that tuning the surface chemistry is an effective way to enable a 3D current with low surface area to achieve uniform Li plating.

2.4 Conclusions

In this work, porous copper scaffolds with interconnected micro-channels were synthesized using wet chemical etching and used as 3D current collectors for lithium metal anode. Laboratory X-ray tomography was used to quantify the physical properties of the porous copper materials. The effects of the three key parameters – surface area, tortuosity, and surface chemistry – were carefully studied. Similar to what previous work has mentioned[27], we quantitatively studied why the high surface area was harmful to the performance of the 3D current collectors, as Li metal was not able to plate deep into the pores due to diffusion limitations and more SEI was formed on the first cycle. A moderate surface area is desirable for a 3D current collector, where the local current density will be low enough to suppress the growth of lithium whiskers while keeping the formation of SEI to minimum. The tortuosity of the porous copper mainly influences the diffusion of lithium ions. To facilitate a uniform distribution of deposited lithium across the whole 3D current collector, the pore size should be kept as large as possible while the tortuosity should be minimized. In considering all of these key physical parameters, the 20Arc samples, with a balance of modest surface area and reasonable pore size, was shown to have the best performance among the copper samples tested, while the 30Furnace sample, which has very large pores and low surface area, had the worst.

These two samples were further coated with metallic Zn to evaluate how surface chemistry can influence the performance of 3D current collectors. Upon electrochemical testing, an average lithium plating/stripping CE of 99.56% was achieved in 30Furnace with Zn coated, which improved from 99.16% without coating. However, the CE for the 20Arc sample did not show as much improvement with the Zn coating because the morphology of the Li in 20Arc was already exceptionally good without coating. The results in this work led to several key points: 1) Although the high surface area can lower the local current density and lead to a uniform Li morphology, it will also introduce large amount of SEI formation because of the increase in surface area. 2) The tortuosity of the 3D current collector should be kept at minimum to induce the uniform distribution of Li in the structure. 3) The Zn coating can effectively improve the morphology of the Li, allowing even 3D current collectors with low surface area to achieve uniform Li plating.

Chapter 2, in full, is a reprint of the material “Quantitatively Designing Porous Copper Current Collectors for Lithium Metal Anodes” as it appears in the ACS Applied Energy Materials, Bingyu Lu, Edgar Olivera, Jonathan Scharf, Mehdi Chouchane, Chengcheng Fang, Miguel Ceja, Lisa E. Pangilinan, Shiqi Zheng, Andrew Dawson, Diyi Cheng, Wurigumula Bao, Oier Arcelus, Alejandro A. Franco, Xiaochun Li, Sarah H. Tolbert, Ying Shirley Meng, 2021, 4, 7, 6454–6465. The dissertation author was the primary investigator and author of this paper. The author wrote the paper.

Chapter 3 Pressure-tailored lithium deposition and dissolution in lithium metal batteries

3.1 Introduction

Lithium (Li) metal is the ultimate anode material to break the specific energy bottleneck of Li-ion batteries. However, due to its low Coulombic efficiency (CE), short cycle life and safety issues caused by dendrite growth and inactive Li formation, practical rechargeable Li metal batteries have not yet been commercialized since its inception in 1976 [6,76,77]. It is widely accepted that the morphology is one of the determinantal factors for CE and cycle life of Li metal batteries [78,79]. In order to achieve reversible, dense Li deposition close to the actual density of Li metal (0.534 g/cm^3), tremendous efforts have been devoted to understanding and controlling the Li deposition process by considering the electroplating as a mass-transport controlled process, which is primarily affected by factors including electrolyte properties (cation concentration, solvation structure, etc.), current density and temperature [5,80]. In addition, due to the highly reducing potential of Li, the (electro)chemically formed solid electrolyte interphase (SEI) between the Li metal and liquid electrolyte makes the electroplating a kinetically slow solid diffusion process. Thus, the Li deposition and dissolution are further affected by the SEI properties.

Strategies have been extensively designed to favor at least one of the four governing factors in the past decades, aiming to improve the Li metal anode performance: first, engineering the electrolyte towards large granular Li particle deposition and stable SEI [81–83]; second, utilizing 3D current collectors to increase surface areas and reduce local current density [84,85]; third, creating artificial SEI to facilitate Li ion transport and prevent parasitic reactions [86]; and fourth, applying elevated temperature to enhance the mass transfer for enlarged Li particles growth [87]. However, the multidimensional requirements to commercialize Li metal batteries, including a cell level energy density of 500 Wh/kg and 1000 cycles with 80% of capacity retention under fast charging conditions [88], can barely be achieved by solely using these approaches. Breaking the current bottleneck requires new solutions that can perfect Li deposition and dissolution on top of these achievements.

In addition to promoting the mass transport, pressurizing the electrode stack has been widely used in modern Li-ion batteries to improve cycling performance by minimizing the interfacial and transport impedance. For Li metal anode, it has been shown that increasing uniaxial stack pressure helps to alleviate Li dendrite formation and improve CE and cycling performance [89]. This offers a new possibility to tune the Li morphology beyond the aforementioned strategies. Moli Energy mentioned in their patent in 1985 that Li deposits formed under stack pressure showed a denser morphology with enhanced cycling efficiency [90]. Wilkinson *et al.* [91] examined the effect of stack pressure in Li/MoS_2 prismatic cells and attributed the Li deformation to the tradeoff between the applied pressure and mechanical strength (creep strength and tensile strength) of the Li. Recent work further proved stack pressure can effectively improve the cycling efficiency and cycle life in anode-free cells [92–94], and achieved close-packed morphology [92]. Undoubtably, applying stack pressure has been proven as an effective method to control the Li deposition morphology. The mechanical properties of Li metal have also been widely studied accordingly [95–98]. However, the underlying scientific principle of pressure effects on Li deposition and dissolution behavior at micro/nano scales and how stack pressure can be utilized to precisely control the Li deposition and dissolution, in combination with clear experimental evidence, still need to be systematically quantified and understood. How to achieve an ideal morphology of Li deposits comprising large Li particles seamlessly packed on the electrode, and how to achieve very high reversibility in deposition and dissolution remain ambiguous. Answering these questions by establishing a pressure-morphology-performance correlation with optimized Li morphology will open new opportunities to rationally design for commercially viable high-energy rechargeable Li metal batteries under various environmental and operating conditions.

Here, combining 3D cryogenic focused ion beam-scanning electron microscopy (3D cryo-FIB-SEM), cryogenic transmission electron microscopy (cryo-TEM), titration gas chromatography (TGC) [78], and molecular dynamics (MD) simulation, we elucidated how stack pressure can be applied to precisely manipulate Li deposition and dissolution towards high performance rechargeable Li metal batteries, overcoming the mass-transport bottleneck. Through a systematic study of the stack pressure effects on the physical morphology and chemical components of Li deposits, we identified two ways in which the stack pressure regulates the Li nucleation and growth: first, tuning the favorable Li growth direction at microscale by altering the surface energy at the Li top surface; second, densifying Li deposits at nanoscale by exerting mechanical constraints. We found the stack pressure induces negligible impacts on SEI structure and components. In the stripping process, the stack pressure plays a key role in retaining the electronically conductive pathway and minimizing the inactive Li formation, while electrochemically deposited Li reservoir is key to maintaining the dense Li structure and its reversibility upon cycling. Based on the quantitative understanding, we achieved an ultra-dense Li deposition (99.49% electrode density) with an ideal columnar morphology, minimal surface area, and made it highly reversible upon cycling with minimal inactive Li formation, and thus improved CE (> 99%) at fast charging condition (4 mA/cm^2) and room temperature. Such pressure-tailored highly reversible Li metal anodes can be the final push to unlock the potential of high-energy Li metal batteries for fast charging and wide temperature operation.

3.2 Method

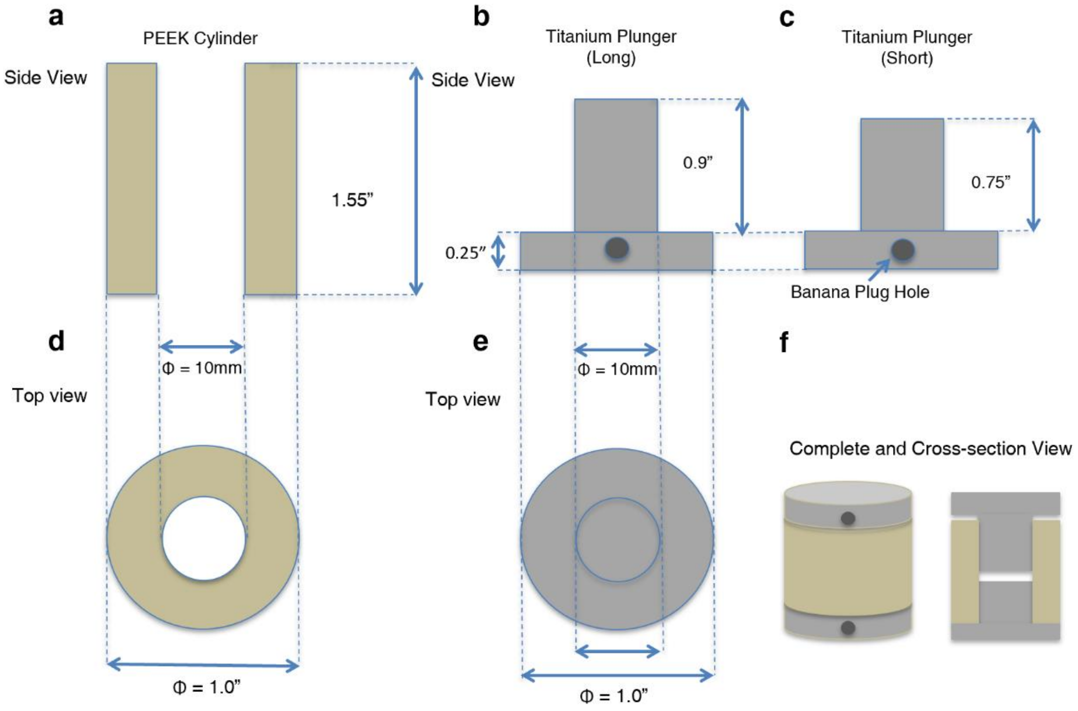

Figure 3.1 Dimensions for the split cell setup. Side views of a) PEEK Cylinder; b) Long Titanium Plunger; c) Short Titanium Plunger. Top view of d) PEEK Cylinder; e) Titanium Plungers. f) Complete and cross-sectional view of the split cell setup.

3.2.1 Split cell

The split cell consists of two parts (**Fig. 3.1**): one polyether ether ketone (PEEK) die (**Fig. 3.1a, d**) mold and two titanium (Ti) plungers (**Fig. 3.1b, c, e**). The Ti plungers have dual purposes in the split cells: 1) to work as current collectors and 2) to apply pressure. Therefore, Ti is chosen as the material for the plungers because of its high electronic conductivity, high mechanical strength, and high stability towards chemical corrosion. One hole is drilled on the bottom of the plungers to provide space for the banana plugs that are connected to the battery cyclers. The PEEK die mold is used as a container to hold the electrochemical cell in place. The total length of the Ti plungers (1.65 inches) is slightly higher than the length of the PEEK die (1.55 inches) so that the PEEK die can freely adjust its position and will not affect the pressure control. All parts required high precision machine polishing so that the friction between the Ti plunger and the inner wall of the PEEK die mold is at a minimum. If the polishing on the PEEK die mold and Ti plunger is not carefully done, extra force might be needed to overcome the friction between the two components, leading to less accurate readings from pressure load cells. Therefore, it is important that the friction between the titanium plungers and the PEEK die does not influence the pressure control while providing a good sealing for the electrochemical cell inside (**Fig. 3.1f**). Furthermore, the split cell design avoids sealing components such as o-rings. The o-ring sealing cannot guarantee completely airtightness, and will further bring uncertainty to the stack pressure value due to friction force. The current design can already provide good sealing for liquid cell cycling for a few days.

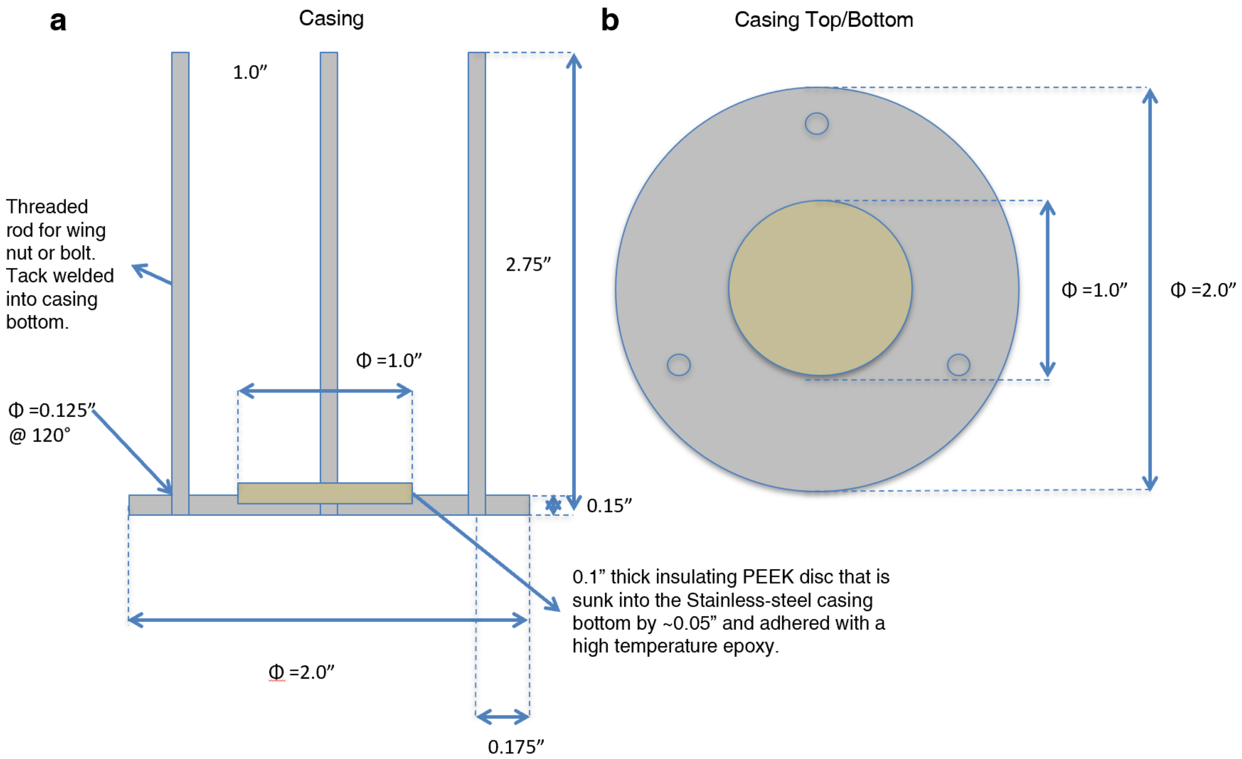

Figure 3.2 Dimensions for the casing for the split cell and load cell. a) Side view of the casing rods and bottom; b) Top view of the Top and Bottom of the casing.

3.2.2 Casing

The casing consists of two parts (**Fig. 3.2**): three threaded rods (**Fig. 3.2a**) and top/bottom plates (**Fig. 3.2b**). The split cell and the pressure load cell are placed uniaxially inside the casing (**Fig. 3.3a**). The top/bottom plates stack the split cell and the pressure load cell. Bolts or wing nuts are used to precisely control the stack pressure exerted by the plates. A thin PEEK disc is sunk into the top/bottom plates at the center where the split cell will sit. The PEEK disc can prevent shorting. All the metal parts of the casing are made of stainless steel.

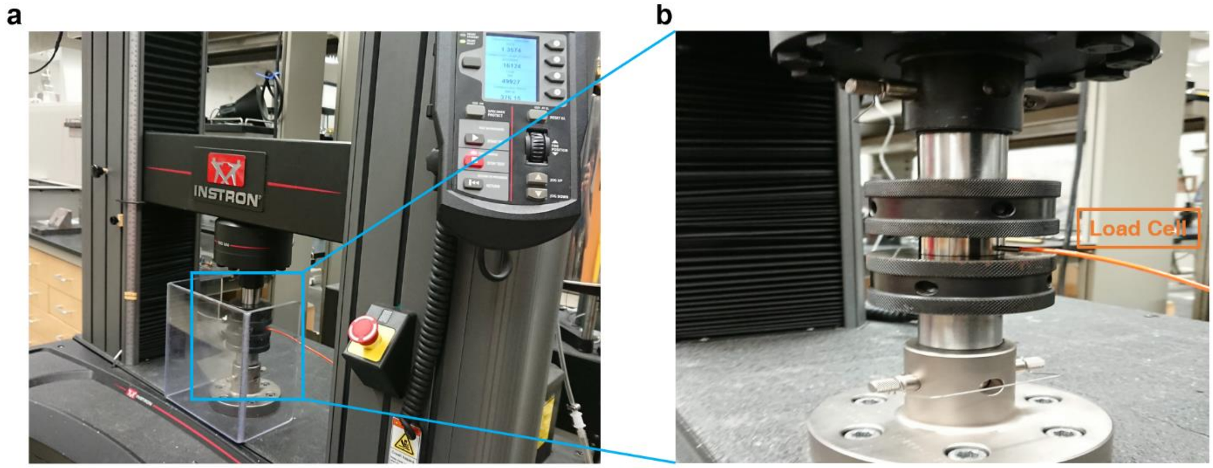

Figure 3.3 Calibration of the load cell: a) the calibration of the load cell using Instron 5982 Universal Testing System. b) Zoom-in image of the load cell.

3.2.3 Load cell calibration

The DYHW-116 load cell (Bengbu Dayang Sensing System Engineering Co, Ltd) and a digital LED display monitor the exerted stacking pressure on the split cell. The load cells have different measuring ranges. Choosing the most suitable range (0 to 1000 kPa is enough for Li metal anode with liquid electrolyte) for the specific testing scenario is beneficial for a higher-pressure resolution. Besides, it is crucial to calibrate the load cell before use since the default reading of the load cell might be way off from the actual pressure that is being measured. To calibrate the load cell, a set of known loads is first applied onto the load cell by using the 100 kN Instron 5982 Universal Testing System (**Fig. 3.3a**). The readings from the load cell are first calibrated at the end of the range of the load cell (i.e., 1000 kPa for the load cell described earlier). Then, the accuracy of the load cell setup can be compared to the load applied by the Instron testing system over the whole range of the load cell to ensure that the calibration is accurate. This calibration method allows to precisely set the load cell readings to correspond to the actual pressure applied to the sample by taking into account the sample area.

3.2.4 Electrochemical testing

The Cu||Li cells were made by sandwiching the Li metal foil (7mm diameter, 50µm thick), Celgard 2325 separator (1/2-inch diameter) and the cleaned Cu foil between the two titanium plungers inside the PEEK die mold. Only minimum amount of electrolyte (~5 µL) was added to the Cu||Li cells to wet the separator. The bisalt electrolyte consists of 4.6 m LiFSI (battery grade; Oakwood Products, Inc.) + 2.3 m LiTFSI (99.95%; Sigma-Aldrich) in DME (anhydrous, >99.5%; Sigma-Aldrich). All salts were dried under vacuum at 120˚C overnight and the solvent was dried by using molecular sieves for three days before making the electrolyte. After the assembly, the split cell and the load cell were put into the cell holder, which provided the uniaxial stacking pressure. The uniaxial stacking pressure was adjusted using the three screws on the cell holder. The screws were carefully adjusted to apply the desired stacking pressure to the split cell while keeping both the split cell and the load cell in vertical position. The cell was tested inside the glovebox using Landt CT2001A battery cycler (Wuhan, China). Various current densities and stacking pressure were applied to conduct the study as indicated in the main text.

Li-Cu pouch cell test: Li-Cu cells were used for cycling performance comparison under different pressures, in order to make sure the Li supply in the working electrode is sufficient so that the influences from other parts of a battery can be excluded. Li chip of 16 mm (diameter) x 0.6 mm (thickness) from MTI as anode and Cu foil as cathode, with flooded bisalt electrolyte, were used for making small Li-Cu pouch cells to perform the cycle life evaluation under 70 and 350 kPa. The cells were discharged (Li plating) at 4 mA/cm^2 for 30 minutes (2 mAh/cm^2), following by charging (Li stripping) at the same current rate to 1 V. The cell was considered as reaching "end of life" once the discharge was automatically cut off by a voltage limit of -0.5 V within 30 minutes (resulting in Li plating less than 2 mAh/cm^2) due to increasing overpotential upon cycling.

3.2.5 Cryogenic Focused Ion Beam Scanning Electron Microscopy (Cryo-FIB-SEM)

The Cu foil with deposited Li was obtained from the split cell and then washed with DME to remove the residual electrolyte in the Ar-filled glovebox. The sample was mounted on a SEM stub (Ted Pella) in the glovebox, then transferred to a FEI Scios DualBeam FIB/SEM system with an air-tight transfer holder to minimize air exposure. Liquid nitrogen (N_2) was used to cool down the sample stage to -180 ^oC to create a cryogenic environment which minimizes beam damage to the sample. Gallium (Ga) ion beam with a voltage of 30 kV, current of 7 nA and dwell time of 100 ns was used to roughly mill down the cross-section of the deposited Li. After the rough milling, the cross-section is cleaned with ion beam at 1 nA. The SEM image of the cross-section was taken using Everhart-Thornley Detector (ETD) at 5 kV and 0.1 nA.

3.2.6 Three-dimensional (3D) reconstruction of cryo-FIB-SEM images

A series of cross-sectional SEM images were taken to reconstruct the 3D bulk structure of the deposited Li. First, a rough cross-sectional milling (30 kV, 7 nA) was done on the deposited Li. After that, the left and right sides of the cross-section were milled away to single out the region of interest (ROI, 14 μm×4 μm×4 μm). Two cross marks were then made by milling near the ROI, one on the top left corner and another one on the left side cross-sectional wall, to serve as correctional landmarks for the automatic slicing and imaging. The ROI and the landmarks were selected in the Auto Slices & View G3 software (Thermo Fisher Scientific) which controls the automatic slicing and imaging. 40 slices (100 nm thick each) of the cross-section were acquired at 30 kV and 0.5 nA and the SEM image of each slice was taken with ETD detector at 5 kV and 0.1 nA. The 40 slices of cross-sectional images were then integrated in the Amira-Avizo software (Thermo Fisher Scientific) to reconstruct the 3D bulk structure of the deposited lithium. The voids and Li volumes were also calculated using the Amira-Avizo software based on contrast difference. The electrode density was calculated based on the ratio of Li metal volume and electrode volume (sum of voids volume and Li metal volume).

3.2.7 Cryogenic Transmission Electron Microscopy (Cryo-TEM)

The Cryo-TEM sample was prepared by peeling the deposited Li under different pressure from Cu foils onto the TEM grid. Both samples at 75 kPa and 350 kPa were tested at current density of 2 mA/cm^2 for plating Li for 5 minutes. TEM samples were slightly rinsed with DME to remove trace Li salts in Ar-filled the glovebox. Once dried, the samples were sealed in airtight bags and plunged directly into a bath of liquid nitrogen. The airtight bags were then cut and the TEM grids were immersed in liquid N_2 immediately. Then the grids were mounted onto a TEM cryo-holder (Gatan) via a cryo-transfer station. In short, the whole TEM sample preparation and transfer process prevents any contact of Li metal with the air at room temperature. TEM characterizations were carried out on JEM-2100F at 200 kV. High resolution TEM (HRTEM) images were taken at a magnification of 500 kx with Gatan OneView Camera (full 4K × 4K resolution) when the temperature of samples reached about 100 K. Fast Fourier transform (FFT) patterns were analyzed using DigitalMicrograph software.

3.2.8 Titration Gas Chromatography (TGC)

TGC method[78] was used to quantify the amount of inactive metallic Li formed after cycling under different conditions. After the Li was plated and stripped under the desired condition, the Cu||Li cell was recovered from the split cell and the Cu foil with residual inactive Li together with the separator were put into a 30 mL bottle without washing. The bottle was then sealed with rubber stopper and metal wires to prevent the generated gas from leaking and minimize safety hazards. The internal pressure of the bottle was then adjusted to 1 atm by connecting the bottle and glovebox environment, whose internal pressure has been adjusted to 1 atm, with an open-ended syringe needle. After taking out the bottle from the glovebox, excessive amount (0.5 mL) of deionized (DI) water was injected into the bottle and the residual inactive metallic Li reacts with the DI water to form H_2 gas. The as-generated gas was then well mixed by shaking and a gas-tight syringe was used to quickly take 30 µL of the gas from the sealed bottle. The gas was then injected into Nexis GC-2030 Gas Chromatograph (Shimadzu) for H_2 measurement. A pre-established H_2 calibration curve was used to calculate the mass of inactive metallic Li from the measured H_2 peak area. With the conversion between mAh and mg of Li shown in the following, the percentage of inactive metallic Li formed after stripping in the total amount of the Li plated can be calculated.

$$1\ \mathrm{C} = 1\ \mathrm{A} \times \mathrm{s} = 1000\ \mathrm{mA} \times 1/3600\ \mathrm{h} = 1/3.6\ \mathrm{mAh}$$

$$1\ \mathrm{C} = 6.25 \times 10^{18}\ \text{electrons} = 1.038 \times 10^{-5}\ \text{mole of electrons}$$

$$\mathrm{Li^+} + \mathrm{e^-} = \mathrm{Li}$$

$$1\ \mathrm{mAh} = 3.7368 \times 10^{-5}\ \text{mole of Li} = 0.2594\ \text{mg of Li}$$

3.2.9 Molecular dynamics (MD) simulation of Li deposition

MD simulations were used to decipher the temporal evolution of Li deposition on Cu surface under applied uniaxial stacking pressures of 0 kPa and 350 kPa, respectively. The

Newton's equations of motion were solved to obtain the temporal positions of Cu and Li atoms. The Cu substrate used in the simulations comprised 25,200 Cu atoms arranged in an *fcc* lattice structure with a domain of 12.77 nm (L) × 25.56 nm (W) × 1.3 nm (H).

An initial energy minimization of Cu surface was performed with 0 and 10^{-8} eV $Å^{-1}$ energy and force cut-off, respectively. The Li deposition was directed to the Cu surface at a deposition rate of 20 Li ps^{-1}. The Li deposition was simulated in an isothermal-isobaric (NPT) ensemble at 300 K with a time step of 1 fs and a cut-off distance of 10 Å under a stipulated uniaxial stack pressure (0 kPa or 350 kPa). The Li-Li and Cu-Cu atomic interactions were simulated with the modified embedded atom method (MEAM) interatomic potentials[99,100], whereas the Li-Cu interactions were modeled with the Lennard-Jones (L-J) 6-12 interatomic potentials with the following L-J potential parameters: ε_{Cu-Li}= 0.047 eV and σ_{Cu-Li} = 2.182 Å. The Li-Cu parameters (ε_{Cu-Li}, σ_{Cu-Li}) were obtained by the Lorentz-Berthelot arithmetic mixing rules:

$$\varepsilon_{Cu-Li} = \sqrt{\varepsilon_{Cu-Cu}\varepsilon_{Li-Li}}$$

$$\sigma_{Cu-Li} = \frac{(\sigma_{Cu-Cu} + \sigma_{Li-Li})}{2}$$

from the available L-J potential parameters for the pure Li[99] and Cu[100] atoms. Large-scale Atomic/Molecular Massively Parallel Simulator (LAMMPS) MD simulation package [101] was used to perform all simulations, whereas the atomic scale trajectory information was visualized by using Open Visualization Tool (Ovito) [102].

The Cu surface area occupied by Li was calculated by summation of the partial area covered by deposited Li within a stipulated distance (here, 1.5 × van der Waal's radius of Li atom (1.82 Å) was used) on the Cu surface. The Li-Li pairwise distribution function (PDF) was generated with a cut-off distance and bin size of 10 Å and 0.1 Å, respectively. The magnitude of the Li-Li PDF at 0 KPa was shifted downwards by a factor of 4.8 compared to that at 350 kPa. Such a difference should account for the empty space in the simulation box when the Li-Li PDF was generated. The surface Li solid mesh was constructed with a virtual probe sphere of radius 3 Å where the virtual probe sphere was used to quantify the amount of Li volume that can be filled within the Li deposit.

Finally, the implications of the MD simulations based on the computational Li deposition rate are also explained in comparison with the experimental Li deposition rate at 2 mA cm^{-2} to give a proper perspective and context of their relevance. To compare the two very different rates in the temporal progression, we use the mass/charge conservation as the basis to explain the relevance. In the MD simulations, a total of 19,031 Li atoms were deposited on the Cu surfaces with a total deposition area of 652.8 nm^2 over 1 ns at 350 kPa. This deposition rate was equivalent to 2.92×10^{15} Li cm^{-2} ns^{-1} in the MD simulation. On the other hand, a total number of Li atoms deposited during experimental study at 2 mA cm^{-2} over 10 minutes is equivalent to 1.25×10^{16} Li cm^{-2} s^{-1}. Therefore, based on the mass/charge conversation principle, the experimental Li deposition rate at 2 mA cm^{-2} for 10 minutes is equivalent to the computational deposition rate of 20 Li ps^{-1} for 4.28 ns in the MD simulation. Thus, the overall morphological evolutions between the experimental observations and MD simulations should be relatively relevant.

Figure 3.4 Quantifying pressure effects on Li metal anode Coulombic efficiency and plating morphology. a) the pressure experiment set-up, and the configuration of Li-Cu cell. b) pressure vs. Coulombic efficiency (first cycle) under various current densities of 1, 1.5 and 2 mA/cm^2, all plating for 4 mAh/cm^2 and stripping to 1 V. At each testing condition, two cells were tested. The error bar represents the standard deviation of the average values of Coulombic efficiency. c) Optical image of deposited Li under high current density (2mA/cm^2), high loading (4 mAh/cm^2), and optimized pressure conditions (350 kPa). d-g) top view and h-k) cross-section of Li deposited under various pressure at 2 mA/cm^2 for 1 hour (2 mAh/cm^2). l-o) cross-section SEM images of Li deposits at 2 mA/cm^2 for 10 min (0.333 mAh/cm^2). The insets represent the schematic illustration of the deposited Li micromorphology under different stack pressures. d, h, l) at 70 kPa (in blue frame); e, i, m) at 140 kPa (in green frame); f, j, n) at 210 kPa (in orange frame); g, k, o) at 350 kPa (in red frame). p) electrode thickness, q) electrode porosity and r) normalized volume of pure deposited Li calculated from 3D cryo-FIB-SEM reconstruction. Scale bars in d-o) are 2 μm. Please note that the actual cross-section thickness should be divided by $sin52^o$ due to the FIB-SEM stage rotation.

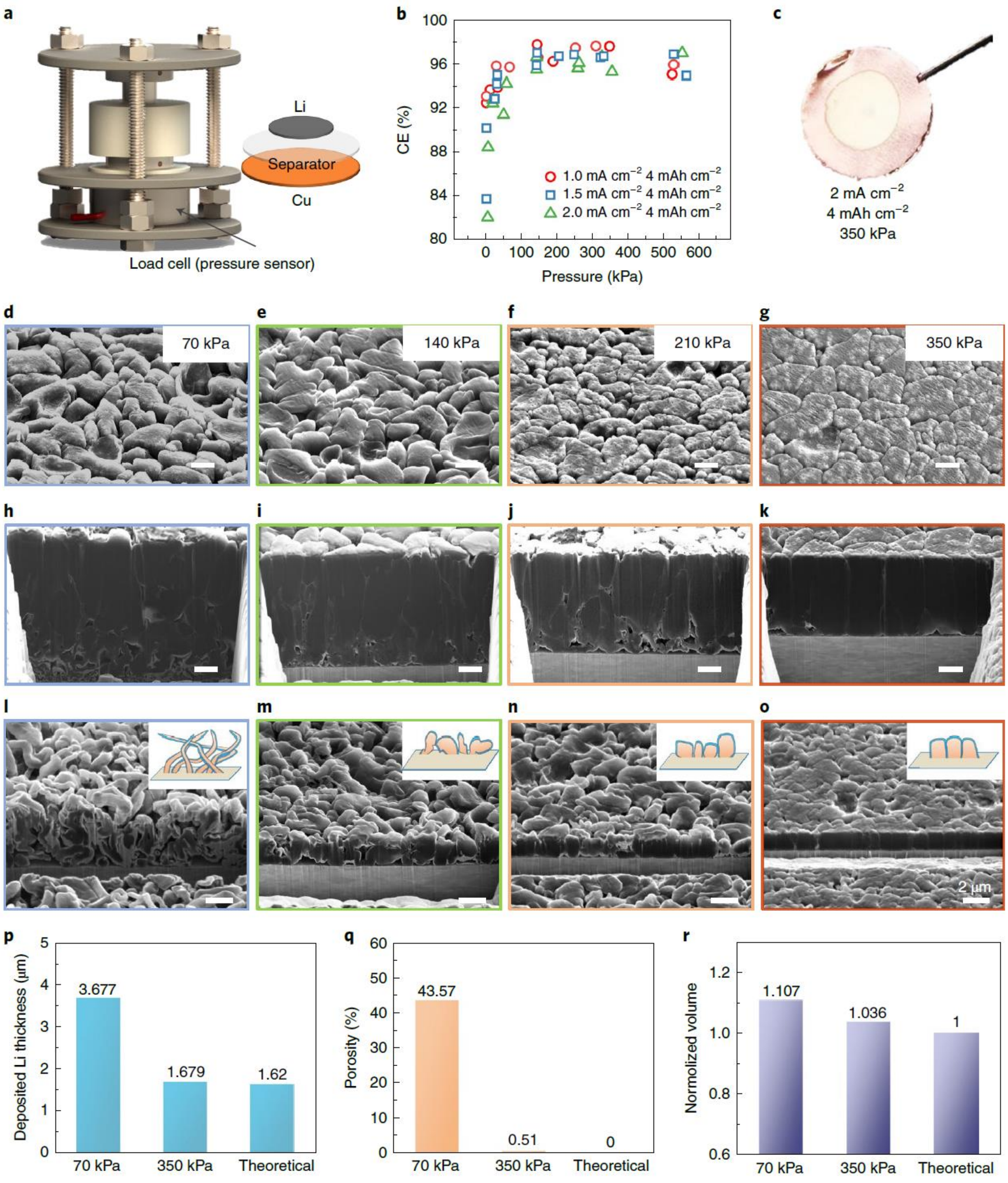
a
Li
Separator
Cu
Load cell (pressure sensor)
b
100
96
92
88
84
80
CE (%)
0
100
200
300
400
500
600
Pressure (kPa)
1.0 mA cm^{-2} 4 mAh cm^{-2}
1.5 mA cm^{-2} 4 mAh cm^{-2}
2.0 mA cm^{-2} 4 mAh cm^{-2}
c
2 mA cm^{-2}
4 mAh cm^{-2}
350 kPa
d
70 kPa
e
140 kPa
f
210 kPa
g
350 kPa
h
i
j
k
l
m
n
o
2 μm
p
Deposited Li thickness (μm)
5
4
3
2
1
0
3.677
1.679
1.62
70 kPa
350 kPa
Theoretical
q
Porosity (%)
60
50
40
30
20
10
0
43.57
0.51
0
70 kPa
350 kPa
Theoretical
r
Normolized volume
1.2
1.0
0.8
0.6
1.107
1.036
1
70 kPa
350 kPa
Theoretical

3.3 Pressure effects on Li deposition

We used a customized split cell with a load cell (**Fig. 3.4a**) to precisely control the uniaxial stack pressure applied to the battery during cycling. The pressure was set as the on-set value for the electrochemical performance testing. **Fig. 3.4b** shows the first cycle CE of Li-Cu cells as a function of applied stack pressure under different current densities from 1, 1.5, to 2 mA/cm^2, using ether-based bisalt electrolyte (4 M lithium bis(fluoro sulfonyl)imide (LiFSI) and 2 M lithium bis(trifluoromethane sulfonyl)imide (LiTFSI) in 1,2-dimethoxyethane (DME)) [57]. At 0 kPa, the CE deceased from 92.5% at 1 mA/cm^2 to 85.5% at 2 mA/cm^2. When the stack pressure is slightly increased to ~35 kPa, the CE increased for all current densities while the CE at 2 mA/cm^2 jumped to 92%. At 350 kPa, the CE was boosted to 98%, 97% and 96% at 1, 1.5 and 2 mA/cm^2, respectively. Increasing the stack pressure above 350 kPa does not further improve the CE, as higher pressure causes severe edge effect (**Fig. 3.5**) [103]. Please note that the optimal pressure for different electrolytes and cell set-up may slightly differ from 350 kPa. **Fig. 3.4c** shows the electrochemically deposited Li at a high current density of 2 mA/cm^2 for 4 mAh/cm^2 exhibits a metallic silver color.

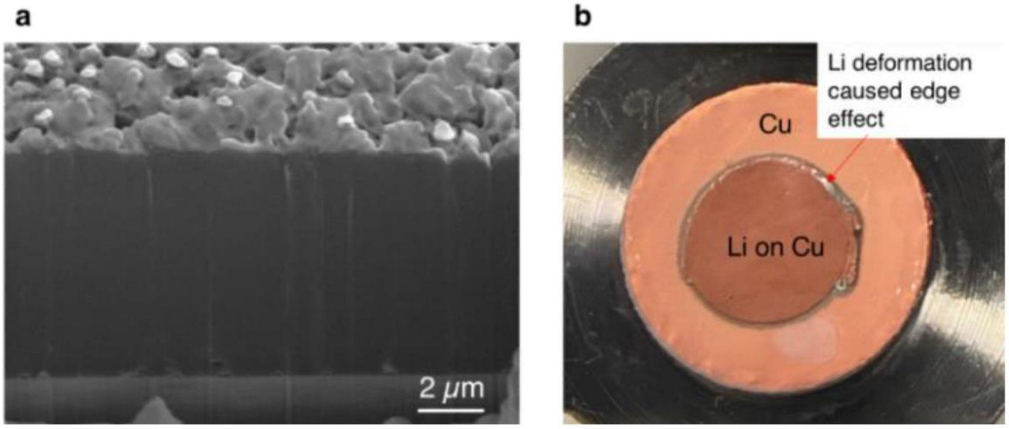

Figure 3.5 The deposited Li morphology under 550 kPa. a) the cryo-FIB-SEM image; b**)** optical image of the plated Li showing squeezed out Li on the edge of electrode.

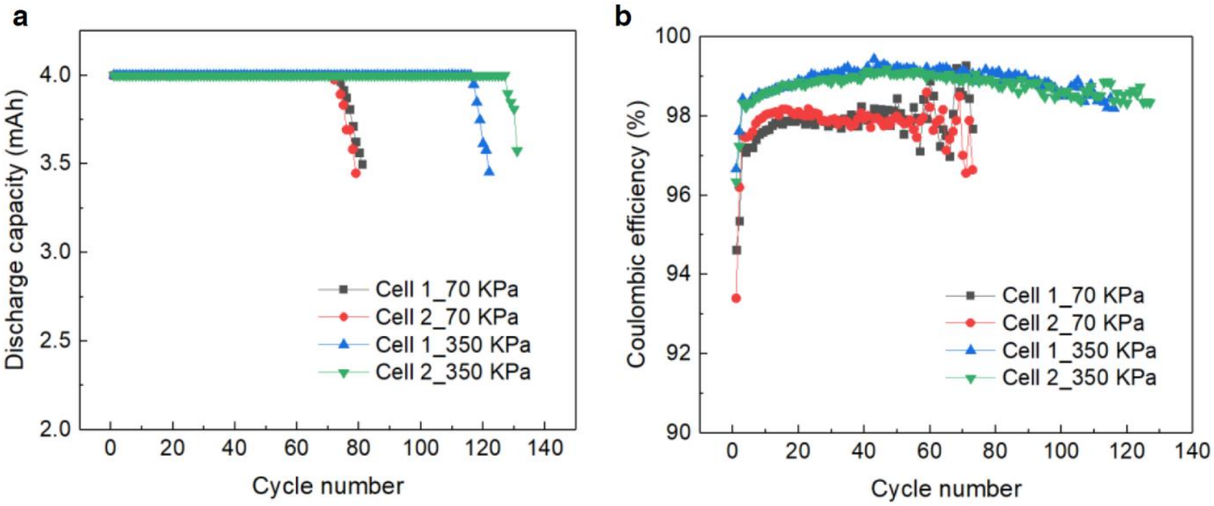

Figure 3.6 Li-Cu pouch cell performances under different stack pressures. a) Discharge capacity *vs.* cycle number. Cells under 70 kPa fail starting from ~73 cycles while almost doubled cycle life (116 -125 cycles) was observed under 350 kPa. b**)** Coulombic efficiency *vs.* cycle number. Average Coulombic efficiency was improved from ~98% to above 99% by increasing pressure from 70 kPa to 350 kPa.

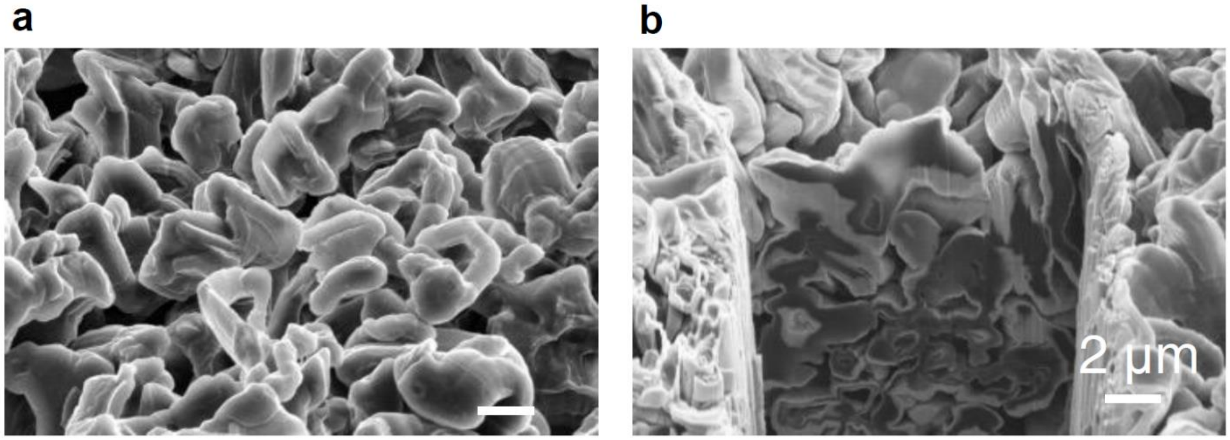

Figure 3.7 Top view a) and cross-section morphology b) of Li deposited under 0 kPa at 2 mA/cm^2 for 1 hour in the bisalt electrolyte at room temperature.

.

Li-Cu pouch cells were used to test the pressure effects on long-term cycling performances. **Fig. 3.6a** shows that a nearly doubled cycle life (116 -125 cycles) was achieved for the cells tested under 350 kPa than those (~73 cycles) under 70 kPa, when setting the overpotential limit to – 0.5 V within 30 minutes as the end-of-life condition. In addition, the average CE was improved from ~98% to above 99% by increasing pressure from 70 kPa to 350 kPa, at a high current density of 4 mA/cm^2 at room temperature (**Fig. 3.6b**).

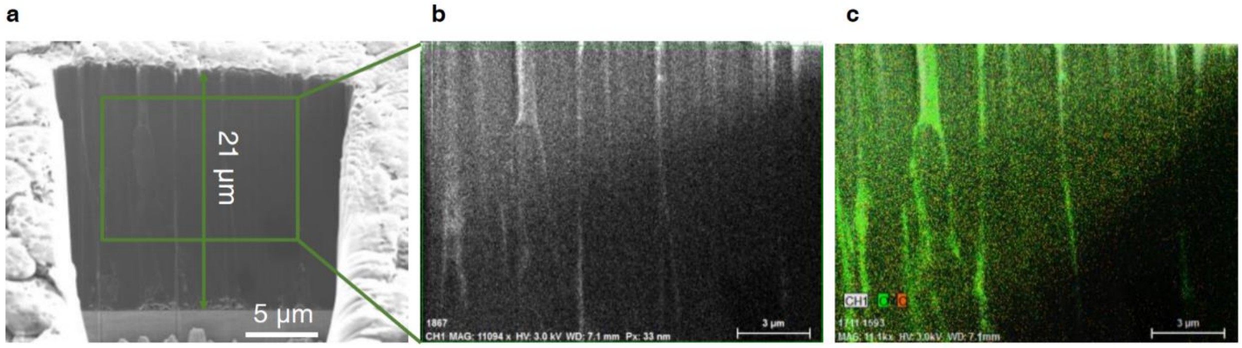

Figure 3.8 Cryo-FIB-SEM images a-b) and EDS mapping c) of 4 mAh/cm^2 of dense Li under 350 kPa at 2 mA/cm^2 in the bisalt electrolyte at room temperature.

We then used cryo-FIB-SEM to examine the deposited Li morphology under four representative pressures: 0, 70, 140, 210 and 350 kPa. A high current density of 2 mA/cm^2 was applied for the one-hour Li deposition (2 mAh/cm^2) morphological study. At 0 kPa, highly porous and whisker-like Li deposits were formed even when using the ether-based electrolyte, as shown in **Fig. 3.7a** (top view) and **3.7b** (cross-section). The Li deposits become notably close-packed with increased pressure from 70 kPa to 350 kPa (**Fig. 3.4d-g**). The cross-section evolution is even more noticeable. As shown in **Fig. 3.4h-k**, along with the increased stack pressure, the electrode thickness obviously decreased. Especially, the cross-section morphology at 350 kPa (**Fig. 3.4k**) shows that the Li deposits form perfect columnar structures with large granular diameter of ~4 μm, near-theoretical thickness (9.64 μm, 2 mAh/cm^2) of ~10 μm and minimum electrode-level porosity, indicating that stack pressure can be used to precisely control the Li deposition morphology. Further increasing the deposition amount to 4 mAh/cm^2, which is required for a practical high-energy battery, the dense, columnar morphology is well maintained (**Fig. 3.8**). We predicted in our previous study that the columnar Li deposits is ideal to improve the CE of Li metal by reducing the isolated metallic Li formation[78]. This study shows that the columnar Li deposits can be achieved by optimizing stack pressure.

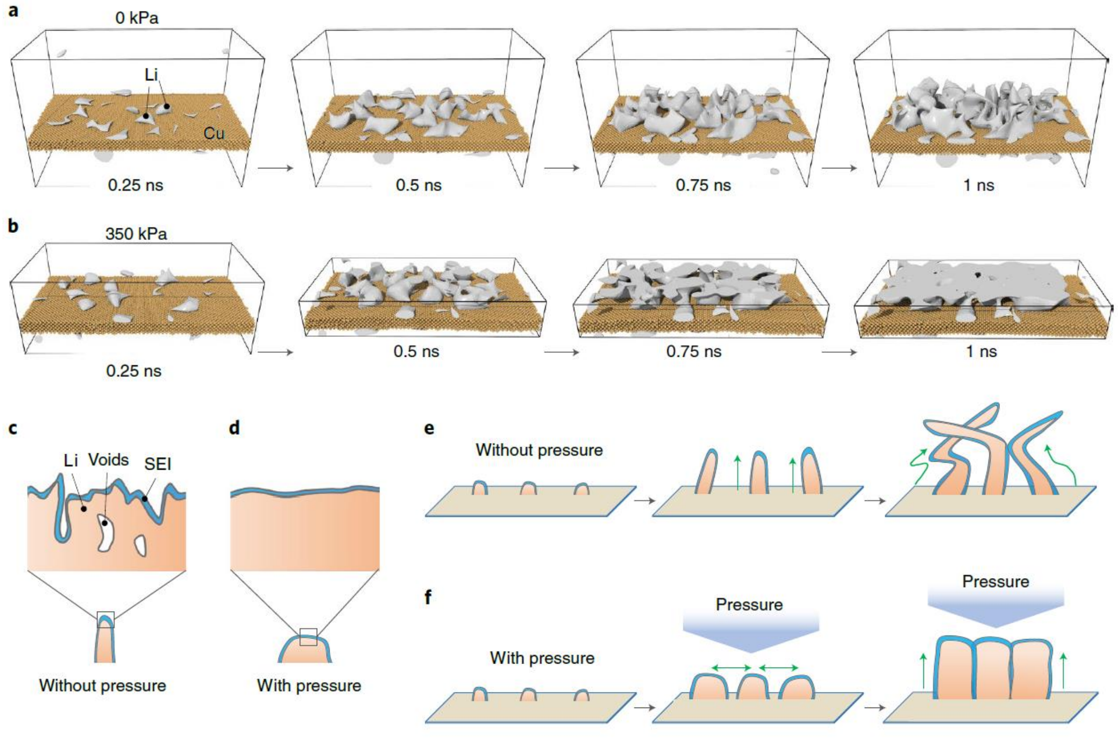

Figure 3.9 MD simulation and schematic illustration of pressure effects on Li nucleation and growth. a, b) the temporal evolution of Li deposition at 0 kPa a) and 350 kPa b) obtained with MD simulations. The cross-section of the Cu surface used for Li deposition is 25.56 × 12.77 nm^2 with a deposition rate of 20 Li/ps. Additional simulation details can be found in Methods and Supplementary Discussion. c, d) schematic illustration of atomic-level morphology of Li under no stack pressure c) and optimal stack pressure d) simulated by MD simulation. e) Li nucleation, initial growth and growth under no stack pressure. f) Li nucleation, initial growth and growth under optimal stack pressure. The green arrows indicate the Li growth direction.

It is worth noting that the bottom section of the Li deposits turns from relatively porous at 70 kPa (**Fig. 3.4h**) to completely dense at 350 kPa (**Fig. 3.4k**), though the top section of the Li deposits at the four different pressures are all dense, indicating the pressure effect plays an important role at the initial stage of Li nucleation and growth. With this assumption, we examined the pressure effects on Li nucleation and initial growth stage with reduced Li deposition loading at 2 mA/cm^2 for 0.33 mAh/cm^2 under 70, 140, 210 and 350 kPa, respectively. As shown in **Fig. 3.4l-o**, the as formed Li nuclei show similar morphology as the bottom part of the one-hour deposits shown in **Fig. 3.4h-k**.

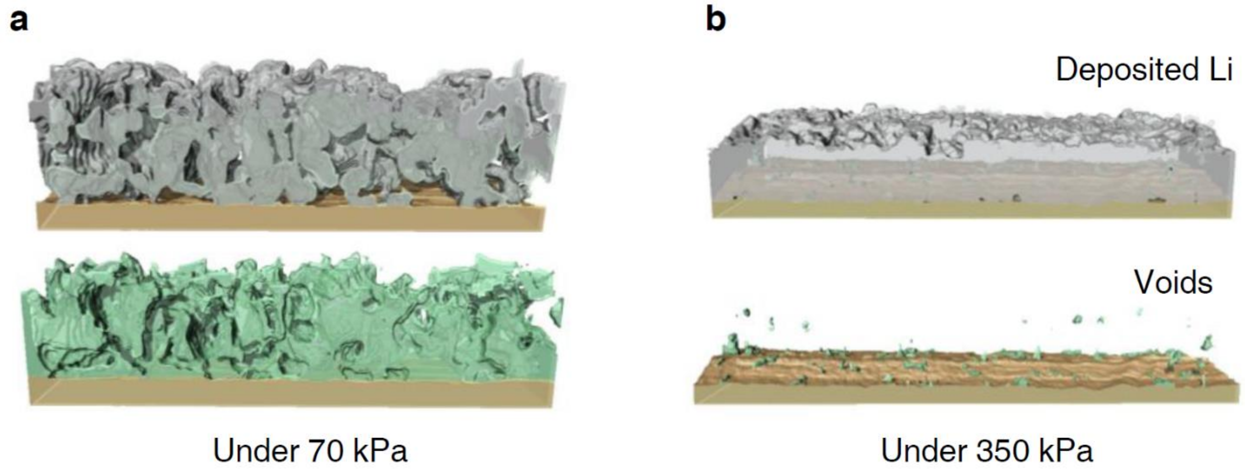

Figure 3.10 Cryo-FIM-SEM 3D reconstruction of deposited Li (grey) and voids (green) from cryo-FIB-SEM image sequences, plating at a)70 kPa and at b) 350 kPa.

We further used cryo-FIB 3D reconstruction to quantify the porosity and volume of Li deposits formed under 70 kPa and 350 kPa (**Fig. 3.10**). Ideally, the total deposited Li (0.333 mAh/cm^2) should exhibit a theoretical thickness of 1.620 µm with zero porosity. When plating at 70 kPa and 350 kPa, the Li layer thickness is measured to be 3.677 µm and 1.697 µm, respectively (**Fig. 3.4p**); the porosity is calculated to be 43.57% and 0.51%, respectively (**Fig. 3.4q**). Based on these numbers, the pure deposited Li volumes at 70 kPa and 350 kPa are normalized as 1.107 and 1.036, respectively, which exceed the theoretical value of 1 (**Fig. 3.4r**). The increased volume is ascribed to the porous electrode structure, where more Li deposits are exposed to liquid electrolyte and form SEI with large surface areas. Eliminating the porosity of Li deposits is essential to minimize the surface exposure to liquid electrolyte that causes extra parasitic reactions which consume electrolyte and active Li. The similar cryo-FIB 3D reconstruction analysis was performed for Li deposits plated for 2 mAh/cm^2 under 70 kPa and 350 kPa (**Fig. 3.11**).

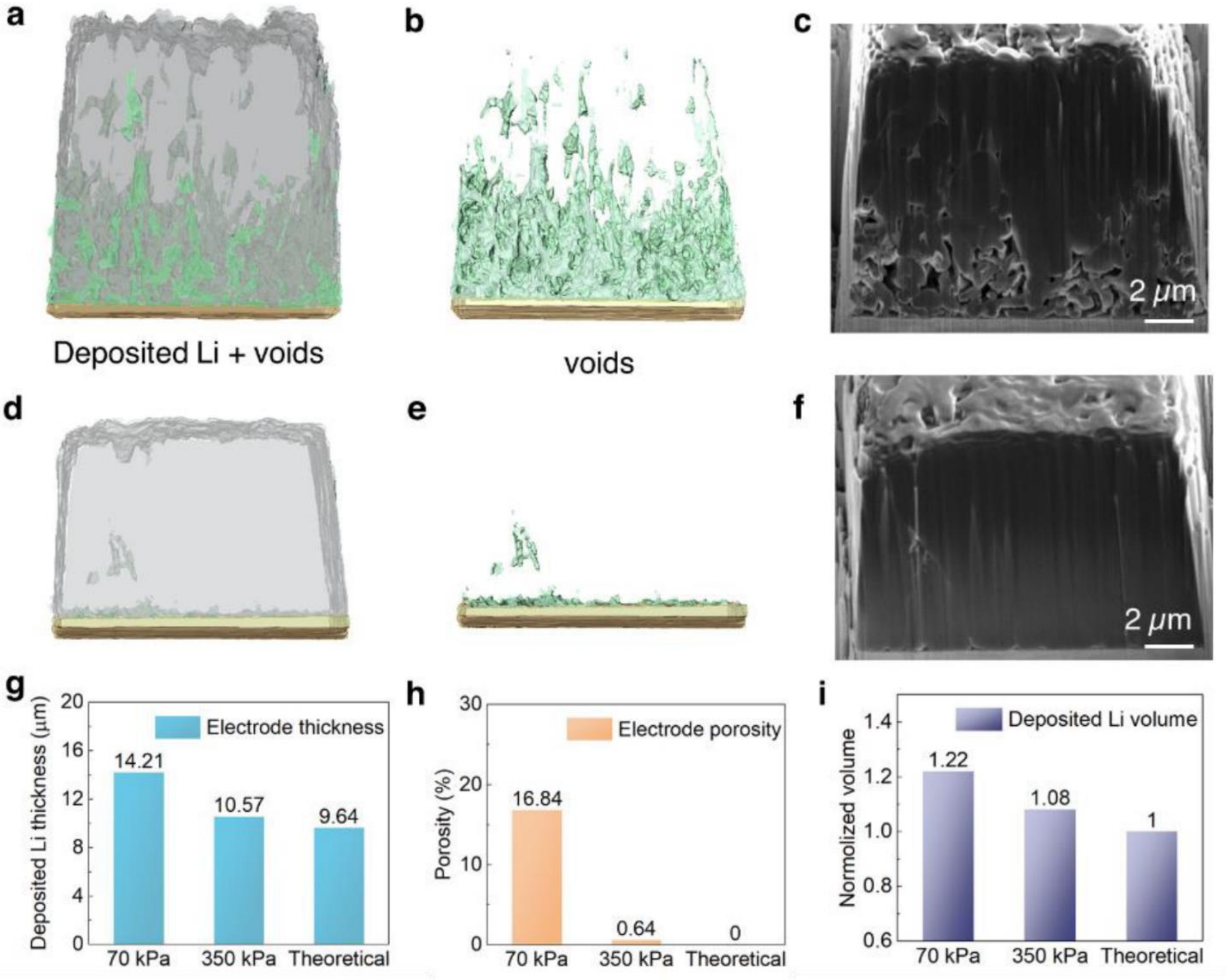

Figure 3.11 3D reconstruction of deposited Li (grey) and voids (green) from cryo-FIB-SEM image sequences, plating at a-c) 70 kPa and at d-f) 350 kPa. g) electrode thickness, h) electrode porosity and i) normalized volume of pure deposited Li calculated from 3D cryo-FIBSEM reconstruction. All plated at 2 mA/cm^2 for 1 hour. Compared to the initial plating stage after fully plating to 1 hour, the major change is that at 70 kPa, the electrode porosity reduces from 43.57% to 16.84%. This is because the top part of the deposited lithium becomes dense in the "fixed-gap" cell set-up where stack pressure gradually increases during the plating process. At 350 kPa, the electrode porosity remains almost unchanged from the initial stage to the fully plated stage, all showing very low porosity. This further supports the proposed lithium growth mechanism under optimized pressure (**Fig. 3.9f**).

Based on the above pressure-tailored Li deposition, we explored the possibility to overcome the mass transport limitations at high rate and low temperature by applying stack pressure: at higher plating rate of 4 mA/cm^2 and room temperature, the densely packed columnar structure is still maintained under 350 kPa (**Fig. 3.12**). At 0°C, very dense Li deposition can be achieved at 2 mA/cm^2 under increased stack pressure of 420 kPa (**Fig. 3.13**). These results indicate that applying an optimized stack pressure is a feasible way that could potentially enable the fast charging and low temperature operation for rechargeable Li metal batteries.

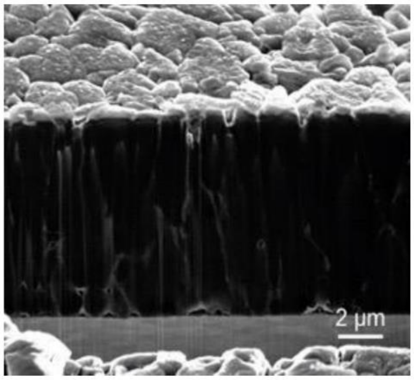

Figure 3.12 Cross-section morphology of Li deposited under 350 kPa at 4 mA/cm^2 for 2 mAh/cm^2 at room temperature.

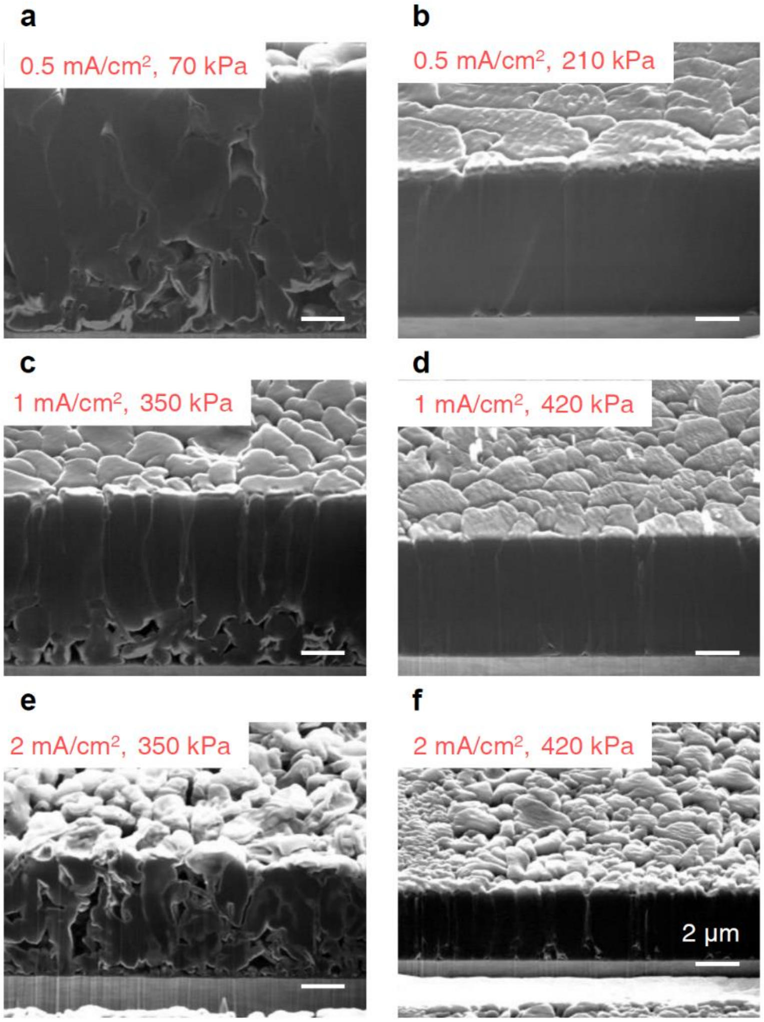

Figure 3.13 Cross-section morphology of Li deposited under various current densities and stack pressure for 2 mAh/cm^2 at 0 ˚C.

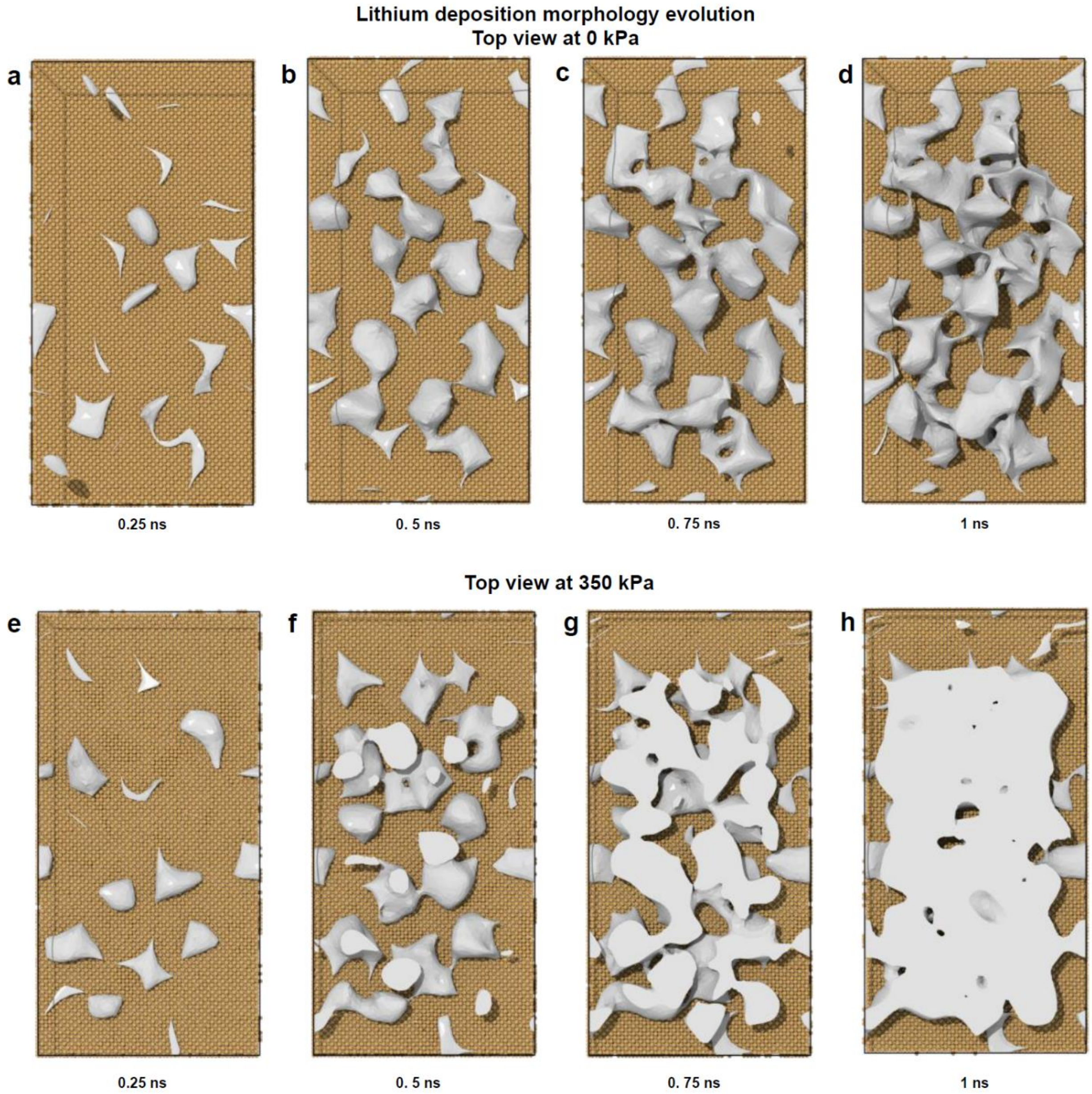

Figure 3.14 MD simulations of the temporal evolution of Li deposition. a-d) at 0 kPa and e-h) at 350 kPa on a Cu current collector surface. The cross-section of the Cu surface is 25.56 × 12.77 nm^2. A deposition rate of 20 Li/ps with a time step of 1 fs was used in the illustration.

MD simulations were applied to reveal the pressure effects on early temporal evolution of Li deposition on Cu surface at nanoscale. The merit and appropriateness of using MD simulation to study this problem is in Supplementary Discussion in Supplementary Information. We compared the scenarios under 0 kPa (**Fig. 3.9a**) and 350 kPa (**Fig. 3.9b**). At 0 kPa, the Li deposition began with randomly distributed Li nucleation sites (0.25 ns in simulation), evolved as isolated reefs (0.5 ns), grew in an uncontrolled fashion (0.75 ns), and led to a porous morphology with poor surface coverage, uneven thickness and poor interconnectivity (1 ns, see top view evolution in **Fig. 3.14**). At 350 kPa, the Li nucleation (0.25ns) and the promoted connectivity of Li nucleation sites (0.5 ns) created a Li deposition with better homogeneity (0.75 ns) and densified layer (1 ns, see top view evolution in **Fig. 3.14**). Better surface area coverage by Li deposits (**Fig. 3.15a**) and higher ordering of the Li deposit under stack pressure is also shown by the subtle differences in the short-range Li-Li pairwise distribution function (**Fig. 3.15b**). MD simulation reveals stack pressure plays an important role in the temporal evolution of the Li deposition by promoting the lateral Li deposition and densifying the individual Li particle through smoothing the surfaces and eliminating the voids at atomic scales (**Fig. 3.9c** and **3.9d**).

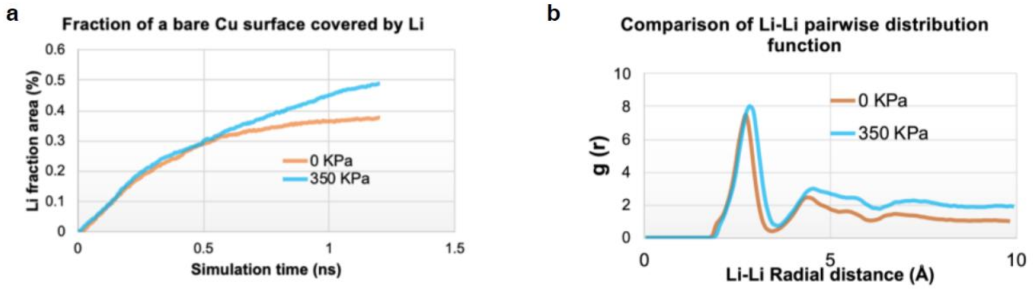

Figure 3.15 a) Comparison of fraction of a bare Cu surface covered by Li at 0 kPa and 350 kPa; b) Comparison of Li-Li pairwise distribution function at 0 kPa and 350 kPa.

Such distinct Li growth behaviors and mechanisms are depicted in **Fig. 3.9e-f**. Without effective uniaxial stack pressure, Li deposit grows freely at the vertical direction, perpendicular to the current collectors (**Fig. 3.9e**). The kinetic regime governs the deposited Li stability and morphology, due to the lower diffusion activation barrier at room temperature[104] and temporal freedom before reaching the favorable *fcc*-hollow sites on the Cu surface. Such free-growing Li whiskers have been extensively observed in previous *in-situ/operando* studies[105,106], where no stack pressure was present in their experimental set-up. Under the stack pressure, the nucleation and initial growth of the Li deposits adopt a lateral growth along the surface of the current collector (**Fig. 3.9f**), due to the free energy change induced by the compressive stress at the electrolyte/separator interface[107]. He *et al* observed the lateral growth phenomenon using *in-situ* TEM with atomic force microscopy (AFM) applied constraint[107]. In our case, at the critical pressure when the resistance at the interface exceeds the surface energy of growing laterally, the Li deposits turn to initially grow laterally to fill the intergranular voids, followed by growing at the interface vertically due to the limitation of space laterally and thus form the columnar structure (**Fig. 3.9f**). In this way, Li deposits with densely packed columnar morphology can be achieved.

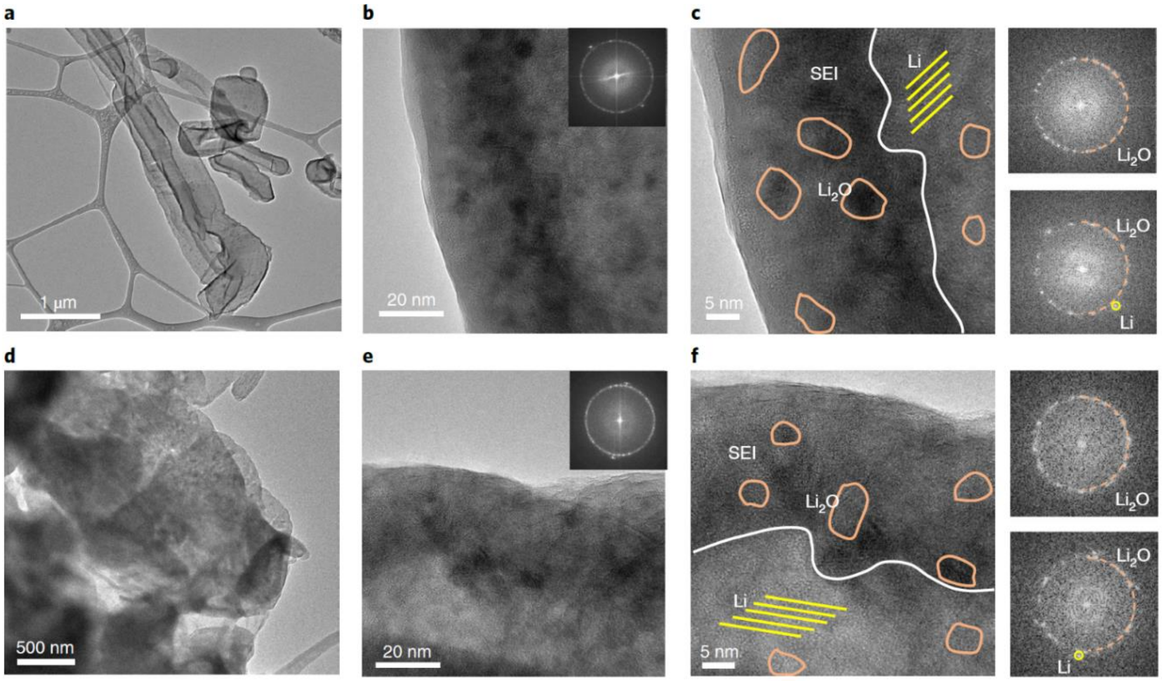

Figure 3.16 Pressure effects on SEI properties by cryo-TEM. a-c) TEM images of Li deposited at 70 kPa. d-f) TEM images of Li deposited at 350 kPa. In c) and f), the circles in orange represent Li_2O nanocrystals in the SEI; the lines in yellow represents crystalline Li metal; the lines in white separates the SEI region and the deposited Li metal region. The top fast Fourier transform (FFT) patterns correspond to the SEI regions, the bottom FFT patterns correspond to the deposited Li metal region. All Li deposited at 2 mA/cm^2 for 5 minutes.

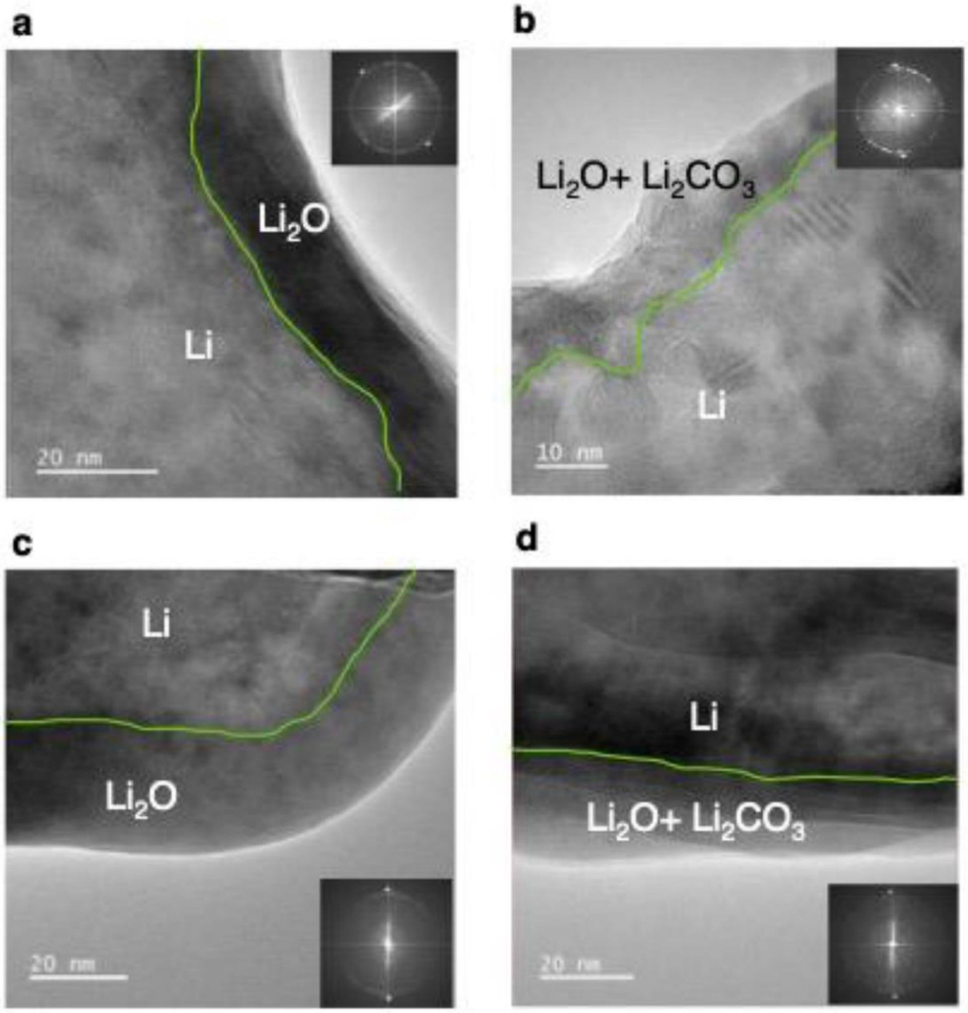

Figure 3.17 Cryo-TEM images of deposited Li a, b) under 70 kPa, and c, d) under 350 kPa.

3.4 Pressure effects on SEI properties

We then used cryo-TEM to investigate the pressure effects on the SEI structure and components. We comparatively studied the Li formed under 70 kPa and 350 kPa, plating at 2 mA/cm^2 for 5 minutes in the ether-based bisalt electrolyte. The Li deposits exhibit a whisker-like morphology at 70 kPa (**Fig. 3.16a**) and large granular morphology at 350 kPa (**Fig. 3.16d**), in accordance with the micro morphology observed by SEM in **Fig. 3.4l and 3.4o**. Under both stack pressure conditions, we observed the SEI structures and components are almost identical. **Fig.**

3.16b and 3.16e compare the nanostructure of the Li deposits under 70 kPa and 350 kPa at large scales. Further zooming in, as shown in **Fig. 3.16c and 3.16f**, the SEI thickness in both samples is 20 - 25 nm, with polycrystalline Li_2O embedded on amorphous matrix, showing a Mosaic-type structure. More representative locations for both samples are shown in **Fig. 3.17**. The cryo-TEM observation indicates the stack pressure has minimum effects on the SEI structures, components, and their distributions. It primarily affects the Li nucleation and growth processes.

3.5 Pressure effects on Li stripping

Pressure effects on Li stripping were systematically examined starting from the ideal columnar Li deposits formed at 2 mA/cm^2 for 1 hour under 350 kPa (**Fig. 3.18a-b**). The stripping rate is 2 mA/cm^2. When no pressure is applied during the striping, there are a lot of voids formed in between individual Li columns that causes liquid electrolyte to penetrate through the electrode (**Fig. 3.18c**). This facilitates the formation of inactive Li as the Li stripping occurs deep at the base of the columnar structure of the Li deposits. After fully stripping the Li to 1 V under no pressure, a significant amount of porous inactive Li remains on the current collector (**Fig. 3.18d**). The CE was only 87% with 12% of the deposited Li remained on the current collector in the form of isolated metallic Li measured by TGC (**Fig. 3.18e**), despite having started with fully dense Li deposits. When a stack pressure of 350 kPa was applied during stripping, Li dissolution was constrained to the top surface only (**Fig. 3.18f**), thus minimizing the exposed surface area and reducing the inactive Li formation, as the electrolyte cannot penetrate into the roots of the dense Li deposits. After fully stripping to 1 V, only 3% of the total capacity remains as the isolated metallic Li on the current collector surface (**Fig. 3.18g**), while the CE is significantly improved to 96% (**Fig. 3.18h**). Noting that SEI only forms during the plating process, therefore, after stripping the quantified SEI amount (1%) in these two samples remain the same (**Fig. 3.18e and 3.18h**), as they all plated at 350 kPa forming identical dense Li. The pressure effect on the stripping process for porous Li deposits also shows the same trend, as shown in **Fig. 3.19**. These results reveal that applying stack pressure during the stripping process helps to keep the electrode columnar structure integrity under large ion flux. It is essential to limit the Li stripping taking place only at the top surface to prevent inactive Li formation.

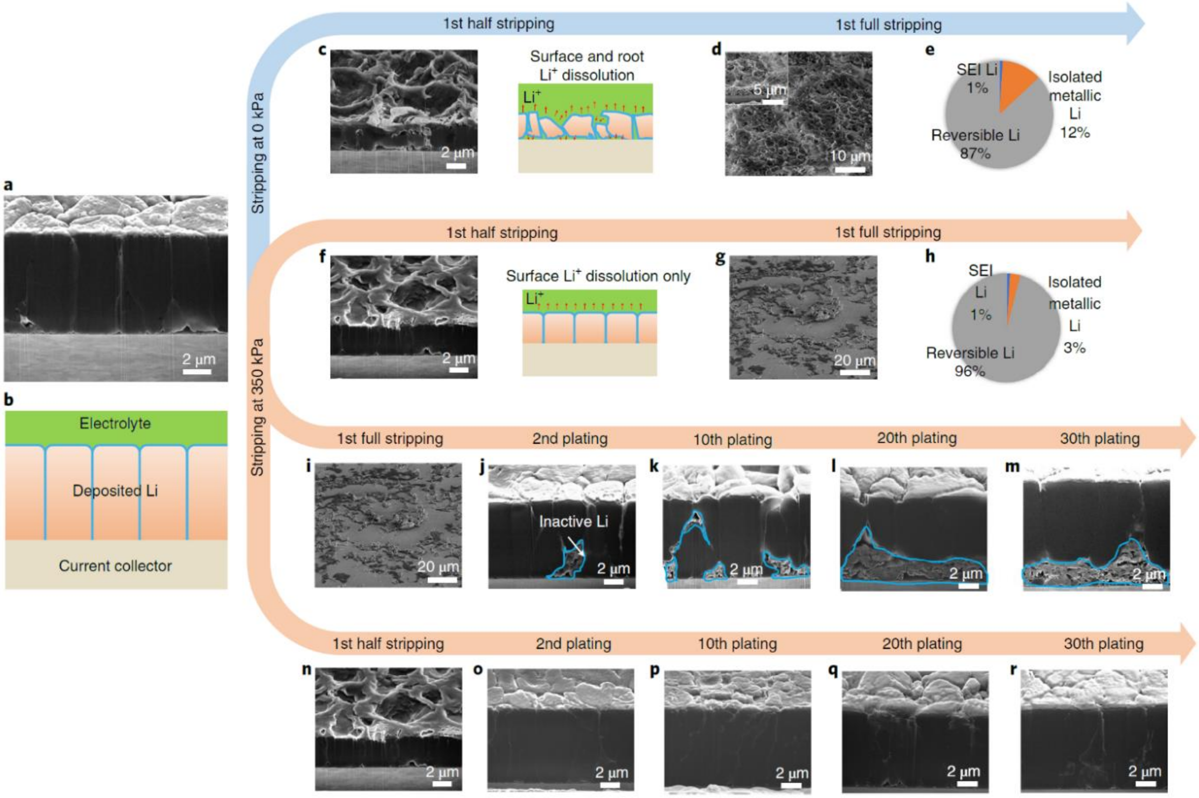

Figure 3.18 Pressure effect on Li stripping process. a, b) cryo-FIB-SEM image and schematic illustration of columnar Li plated at 350 kPa. c-e) Li stripping at 0 kPa: c) cross-section morphology and schematic illustration of half-stripped Li; d) fully stripped Li; e) capacity usage analysis by TGC. f-h) Li stripping at 350 kPa: f) cross-section morphology and schematic illustration of half-stripped Li; g) fully stripped Li; h) capacity usage analysis by TGC. i-r) Li reservoir effect study, plating and stripping under stack pressure of 350 kPa: i-m) Li deposition morphology evolution using full-stripping protocol for 30 cycles. n-r) Li deposition morphology evolution using half-stripping protocol to retain Li reservoir for 30 cycles. All plating and stripping at 2 mA/cm^2, plating for 1 hour, half stripping for 30 min, full stripping to 1V.

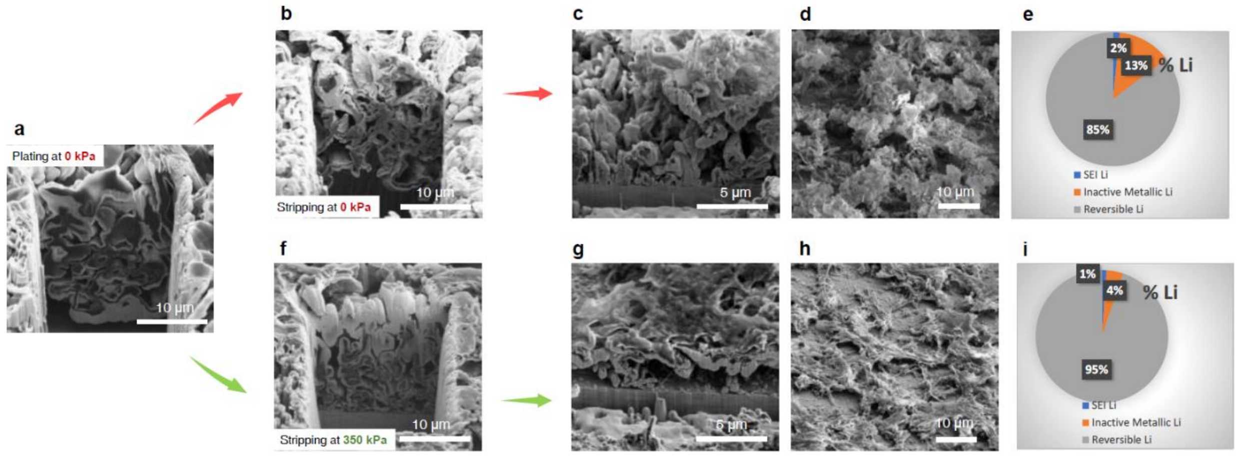

Figure 3.19 Pressure effect on stripping process, plating at 0 kPa. a) cryo-FIBSEM image of Li plated at 0 kPa. b) Li stripping at 0 kPa, cross-section morphology of half stripped Li; c, d) fully stripped Li, cross-section, and top view; e) capacity usage analysis by TGC. f) Li stripping at 350 kPa, cross-section morphology of half-stripped Li; g, h) fully stripped Li, cross-section, and top view; i) capacity usage analysis by TGC. All plating and stripping at 2mA/cm^2, plating for 1 hour, half stripping for 30 minutes, full stripping to 1V.

Though optimal pressure was applied, inactive Li formation is still noticeable after full stripping (**Fig. 3.18i**), due to the inevitable inhomogeneity of electrodeposited Li. When fresh Li is further deposited during the following cycle, the columnar structure is hardly maintained (**Fig. 3.18j**), ascribing to the interference from the inactive Li residue formed in previous cycles. During extended cycles, more and more inactive Li keeps evolving, breaking the dense morphology (**Fig. 3.18k-m**), and consuming electrolyte and fresh Li. Significantly, we found if the electrodeposited Li is not fully stripped in each cycle and is partially maintained as a Li reservoir (**Fig. 3.18n**), the dense, columnar morphology can be well preserved when Li is re-deposited into the reservoir during extended cycles (**Fig. 3.18o-r**). This process is enabled by following the lowest-energy Li diffusion pathway and refilling the existing SEI established during previous cycle. The electrodeposited Li reservoir serves as the re-nucleation sites. In this way, minimum electrolyte and fresh Li will be consumed by subsequent cycling. We further compared the re-plating Li morphology with 1/16, 1/8 and 1/4 of Li reservoir, and identified 1/4 reservoir is essential to maintain the dense morphology (**Fig. 3.20**). This observation also well explains why a Li-reservoir testing protocol always results in higher CE[36], and higher discharge cut-off voltage in a full cell leads to less inactive Li formation[56].

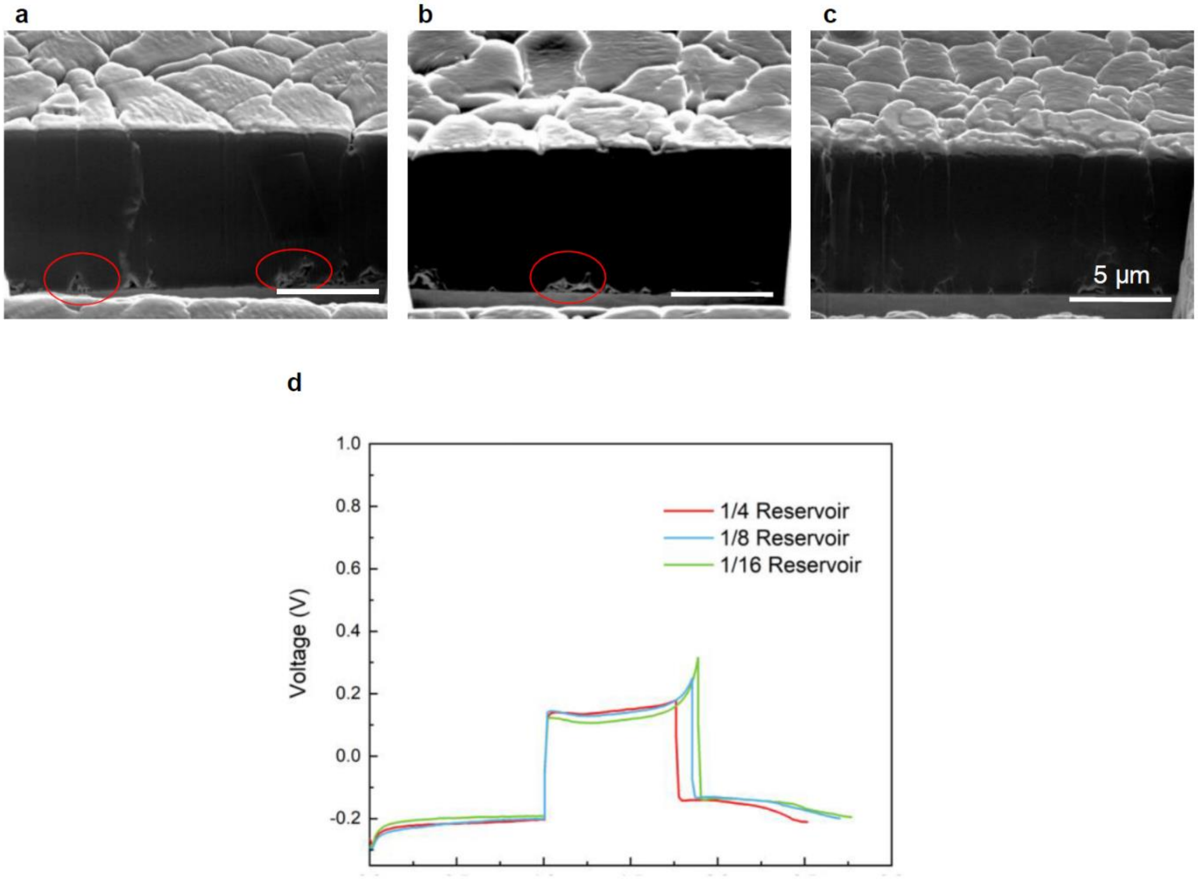

Figure 3.20 Investigating the essential Li reservoir amount for maintaining the dense columnar Li morphology during cycling. a) 1/16 reservoir, b) 1/8 reservoir, c) ¼ reservoir, d) voltage profiles the three conditions. Plating and stripping under 350 kPa, 2 mA/cm^2.

3.6 Conclusions

In summary, we identified that the uniaxial stack pressure can be used as a powerful tuning knob to precisely tailor Li deposition morphology and dissolution geometry. Using multiscale characterization tools, we discovered that applying optimized stack pressure can fine tune Li nucleation and growth direction towards dense deposition, staying away from the dendrite growth caused by mass transport limitations. We achieved the predicted ideal columnar Li deposit with minimal electrode porosity by optimizing the on-set stack pressure at 350 kPa. During the Li stripping process, pressure assures the close interfacing between the dense Li deposits and current collector to prevent the liquid electrolyte from penetrating into the root of the columnar structure, thus dramatically reducing the inactive Li formation. The electrochemically formed dense Li reservoir is the key to maintain the columnar structure reversibly upon extended cycling, greatly improving the cycle life. Such battery electrochemical behaviors under uniaxial stack pressure offer insights towards new design rules and new manufacturing process for practical Li metal batteries and other metal anodes.

Chapter 3, in full, is a reprint of the material “Editors’ Choice—Methods—Pressure Control Apparatus for Lithium Metal Batteries” as it appears in the Journal of Electrochemical Society, Bingyu Lu, Wurigumula Bao, Weiliang Yao, Jean-Marie Doux, Chengcheng Fang and Ying Shirley Meng, 2022, 169, 070537, and “Pressure-tailored lithium deposition and dissolution in lithium metal batteries”, as it appears in the Nature Energy, Chengcheng Fang*, **Bingyu Lu***, Gorakh Pawar, Minghao Zhang, Diyi Cheng, Shuru Chen, Miguel Ceja, Jean-Marie Doux, Henry Musrock, Mei Cai, Boryann Liaw and Ying Shirley Meng, 2021, 6, 987–994. The dissertation author was the primary investigator and author of these two papers.

Chapter 4 Suppressing Chemical Corrosions of Lithium Metal Anodes

4.1 Introduction

With the growing demand of high performance electric vehicles and personal portable devices, lithium (Li) metal anode is crucial for developing high energy density rechargeable batteries (> 500 Wh/kg) due to its high specific capacity (3,860 mAh/g) and low electrochemical potential (–3.04 V versus the standard hydrogen electrode)[3,6,59]. Although extensive studies have been performed to overcome dendrite growth and low coulombic efficiency problems associated with the practical use of Li metal anode[56,62,92], there is a lack of comprehensive understanding of the stability and storage properties of lithium metal anodes in liquid electrolytes, where corrosion plays a critical role[36,37]. Corrosion is a common chemical/electrochemical process that almost all metals will experience when exposed to an oxidating environment[108,109]. During the corrosion, the fresh metal surface will be oxidized, followed by the formation of its corresponding ionic species and the release of electrons[110,111]. The corrosion is usually accompanied by the generation of a passivating layer which blocks the transfer of the electrons and eventually stops the continuous oxidization of the metal[38]. Without the formation of this passivating layer, the corrosion of the metal will continue until the thermodynamic equilibrium is reached when electrochemical potential (μ) difference between the metal and the environment becomes zero[112,113]. In an electrochemical cell, the electrode materials are usually immersed in ion-conducting solvents, which will allow corrosions to take place[114]. Fortunately, in the traditional Li ion batteries (LIBs), a dense and passivating solid–electrolyte interphase (SEI) can be quickly formed during the first a few cycles[115,116], thus preventing the following corrosion of the electrode materials, which enables a stable cycling and storage life for the LIBs.

Several works have shown that the galvanic (electrochemical) corrosion of Li metal will happen when the interface between Li metal and current collector is exposed to the liquid electrolyte[33,39,40], where the exchange of charges will take place[117]. Kolesnikov A. and his co-workers monitored the morphological change of the Li powders casted on the Cu substrate and discovered a continuous shrinkage of the Li near the Li||Cu interface, which was believed to be caused by the Galvanic corrosion between Li and Cu. However, this Li metal and current collector interface can be largely blocked from the electrolyte if a dense Li morphology is achieved during Li plating[92]. Therefore, more research work should be focusing on the chemical stability between Li metal and the liquid electrolytes. It is well known that because of the extremely low standard redox potential of Li (–3.04 V versus the standard hydrogen electrode), Li can immediately react with essentially any electrolyte upon contact[118,119]:

$$\text{n Li} \rightarrow \text{n Li}^{+} + \text{n e}^{-}$$

$$\text{Electrolyte} + \text{n e}^{-} \rightarrow \text{SEI} + \text{soluble electrolyte decomposition products}$$

This simplified reaction pathway depicts the spontaneous chemical corrosion process between Li and the liquid electrolyte. The SEI layers formed during this process, which usually consist of Li_2O, LiF, and other organic compounds, can quickly passivate the Li metal surface[120]. However, due to the inhomogeneity in the solubility and electronic conductivity of these SEI components[41], the continuous decomposition of the electrolyte might still occur on the SEI surface, which is observed in the recent Cryo-STEM work done by Boyle D. T. and his colleagues[34], leading to the further corrosion of the Li metal even after the formation of the initial passivating (SEI) layer. As a result of this continuous chemical corrosion, the corroded Li metal anode will suffer from a loss of active Li^0 material, an increase of cell impedance, and eventually a poor cycling/storage life, which will cause the failure of the cell.

The lifetime of a battery system depends on two key factors: 1) calendar life, the degradation over storage time and 2) cycle life, the degradation over charge-discharge cycles[35]. Despite the fact that tremendous amount of work has been done trying to extend the cycle life of Li metal batteries, few previous works have explicitly considered the key parameters in determining the calendar life of Li metal batteries, as well as the tradeoffs between the calendar life and cycle life. In the extreme case of primary Li battery, where calendar life is the more preferential factor than cycle life, many work has been done to protect the Li metal from degrading during storage by constructing a stable SEI layer for Li protection[121]. However, such artificial SEI can be easily destructed during cycling because of the large volume change of Li plating/stripping. Therefore, it is crucial that the reactivity of the Li is strictly controlled when designing a secondary battery system so that lifetime of it is not limited by neither the calendar life nor the cycle life. Thus, this work focuses on deciphering the key parameters in determining the rate of the chemical corrosion (chemical reactivity) of Li metal in the liquid electrolyte during the extended resting period and find ways to prolong the calendar life of the rechargeable Li metal batteries.

Here, we thoroughly studied the storage properties of the Li metal anode in liquid electrolyte. It is demonstrated that the major source of Li metal mass loss during storage is from the chemical corrosion. To evaluate the chemical stability of Li metal in liquid electrolytes, using the Titration Gas Chromatography (TGC) method[74], we quantify the corrosion trend of plated Li in four representative liquid electrolyte systems: high concentration ether based “Bisalt” electrolyte (4.7m LiFSI + 2.3m LiTFSI in DME)[57], low concentration ether based “Nitrate” electrolyte (1M LiTFSI in DME:DOL with 2wt% $LiNO_3$), carbonate based “Gen 2” electrolyte (1.2M $LiPF_6$ in EC:EMC) and Localized High Concentration Electrolyte (LHCE, LiFSI:DME:TTE in molar ratio of 1:1.2:3)[122]. These four electrolytes are used in this work because they represent the four most popular electrolyte systems studied in the field[123]. The morphological changes of the Li at different stages of corrosion are also recorded by Cryo-FIB/SEM[124]. It is found that the porosity of the plated Li has a significant effect on determining the corrosion rate of the Li in liquid electrolyte. By combining the TGC method and also the three-dimensional (3D) reconstruction of the plated Li by Cryo-FIB/SEM, the porosity of the plated Li is quantified and its corresponding corrosion rate in the liquid electrolyte is calculated. Finally, by using the advanced LHCE and optimized stacking pressure (350 kPa)[125], a ultra-low porosity of Li is achieved. The resulting low porosity Li experiences only 0.8% loss of Li^0 mass after 10 days of immersion in the liquid electrolyte. The fundamental correlation among Li metal porosity, SEI composition and the Li corrosion rate is revealed in this work.

4.2 Method

4.2.1 Electrolyte preparation

Battery-grade lithium bis(fluorosulfonyl)imide (LiFSI) was purchased from Oakwood Products, Inc.; Bis(trifluoromethane)sulfonimide lithium 99.95% (LiTFSI) was purchased from Sigma-Aldrich. All salts were further dried at 120 °C under vacuum for 24 h before use; 1,2-dimethoxyethane (DME) anhydrous, 99.5% was purchased from Sigma-Aldrich; 1,1,2,2-tetrafluoroethyl-2,2,3,3-tetrafluoropropyl ether (TTE, 99%) was ordered from SynQuest Laboratories. Solvents were dried with molecular sieves before use. LiFSI–DME–TTE were mixed in a molar ratio of 1:1.2:3 to prepare the LHCE[122]. All procedures were performed in an argon gas filled glove box (<0.1 ppm O_2, <0.1 ppm H_2O).

4.2.2 Li||Cu coin cells preparation

Copper foil was punched into 1/2 inch diameter pieces (1.27 cm^2) and immersed in 1.0 M HCl solution for 10 minutes. The Cu pieces were then rinsed with deionized water and acetone and finally dried under vacuum. The washed Cu pieces was assembled in the coin cell as the working electrode while the Li metal (0.1 mm thick, China Energy Lithium Co., Ltd.) was the reference and counter electrode. Celgard 2325 separator was used as the separator and soaked in 55 µL of electrolyte. All cell makings were performed in an argon gas filled glove box (<0.1 ppm O_2, <0.1 ppm H_2O).

4.2.3 Pressure controlled split cells

A custom-made split cell that consists of two titanium plungers (1/2-inch diameter) and one polyether ether ketone (PEEK) die mold (1/2-inch inner diameter) is used for the pressure controlled Li plating. All parts used for the split cell were carefully machine polished so that the resistance between the titanium plunger and the inner wall of the PEEK die mold is at minimum while providing a good sealing for the electrochemical cell inside. Cu pieces used in the cells were cleaning in the same way as described in the previous section. The Cu||Li cells were made by sandwiching the Li metal foil (7 mm diameter, 50 µm thick, China Energy Lithium Co., Ltd.), Celgard 2325 separator (1/2 inch diameter) and the cleaned Cu foil between the two titanium plungers inside the PEEK die mold. Only minimum amount of electrolyte (~5 µL) was added to the Cu||Li cells to wet the separator. After the assembly, the split cell and the load cell were put into the cell holder, which provided the uniaxial stacking pressure. The uniaxial stacking pressure was adjusted by the three screws on the cell holder. The screws were carefully adjusted to apply the desired stacking pressure to the split cell while keeping both the split cell and the load cell in vertical position. The cell was tested inside the glovebox using Landt CT2001A battery cycler (Wuhan, China). Various current densities and stacking pressure were applied to conduct the study as indicated in the main text.

4.2.4 Li metal corrosion

The corrosion of Li metal was conducted in two ways. 1) For Li deposited in Li||Cu coin cells, after the electrochemical testing, the coin cells were taken off from the cycler and sealed in a plastic bag to avoid any external electric circuit. After the desired resting time, the coin cells were dissembled in an Ar-filled glovebox and prepared for postmortem characterizations. 2) For Li deposited in split cells, after the electrochemical testing, the split cells were dissembled and deposited Li was immersed in flooded electrolyte and kept in an Ar-filled glovebox. After the desired resting time, the deposited Li was recovered from the electrolyte and prepared for postmortem characterizations.

4.2.5 Cryogenic Focused Ion Beam- Scanning electron Microscopy (Cryo-FIB/SEM)

The copper foil with deposited Li was recovered from the split cell and then washed with DME to remove the residual electrolyte in the Ar-filled glovebox. The sample was mounted on a SEM stub (Ted Pella) in the glovebox, then transferred to a FEI Scios DualBeam FIB/SEM system with an Air-tight transfer holder to minimize air exposure[124]. Liquid N_2 was used to cooled down the sample stage to -180˚C to create a cryogenic environment which helps minimize beam damage to the sample. Gallium ion beam with a voltage of 30 kV, current of 7 nA and dwell time of 100 ns was used to roughly mill down the cross-section of the deposited lithium. After the rough milling, the cross-section is cleaned with ion beam at 1 nA. The SEM image of the cross-section was taken using Everhart-Thornley Detector (ETD) at 5 kV and 0.1 nA. A series of cross-sectional SEM images were taken to reconstruct the three-dimensional (3D) bulk structure of the deposited lithium. First, a rough cross-sectional milling (30 kV, 7 nA) was done on the deposited Lithium. After that, the left and right sides of the cross-section were milled away to single out the region of interest (ROI). Two cross marks were then made by milling near the ROI, one on the top left corner and another one on the left side cross-sectional wall, to serve as correctional landmarks for the automatic slicing and imaging. The ROI and the landmarks were selected in the Auto Slices & View G3 software (Thermo Fisher Scientific) which controls the automatic slicing and imaging. 40 slices (100 nm thick each) of the cross-section were acquired at 30 kV and 0.5 nA and the SEM image of each slice was taken with ETD detector at 5 kV and 0.1 nA. The 40 slices of cross-sectional images were then integrated in the Amira-Avizo software (Thermo Fisher Scientific) to reconstruct the 3D bulk structure of the deposited lithium. The voids and lithium volumes were also calculated using the Amira-Avizo software.

4.2.6 X-Ray Photoelectron Spectroscopy (XPS)

X-ray photoelectron spectroscopy (XPS) was performed using a Kratos AXIS Supra. All samples were dried under vacuum without washing. During sample transfer, the sample was sealed in an air-tight container without air exposure. An Al anode source at 15 kV with a 10^{-8} Torr vacuum level was applied for measurement. The step size for Survey scans was 1.0 eV, followed by high-resolution scans with a step size of 0.1 eV. C 1s peak at 284.6 eV was used for calibration. The etching condition used was Ar^+ mono mode, 5 keV voltage.

4.2.7 Titration Gas Chromatography (TGC)

TGC method[74] was used to quantify the amount of inactive metallic lithium formed after resting in the liquid electrolytes for certain periods of time. After the resting, the Cu foil substrate together with the residue Li was collected and was put into a 30 mL bottle without washing. The bottle was then sealed with rubber stopper and metal wires to prevent the generated gas from leaking and minimize safety hazards. The internal pressure of the bottle was then adjusted to 1 atm by connecting the bottle and glovebox environment, whose internal pressure has been adjusted to 1atm, with an open-ended syringe needle. After taking out the bottle from the glovebox, excessive amount (0.5 mL) of deionized (DI) water was injected into the bottle and the residual inactive metallic lithium reacts with the DI water to form H_2 gas. The as-generated gas was then well mixed by shaking and a gas-tight syringe was used to quickly take 30 μL of the gas from the sealed bottle. The gas was then injected into Nexis GC-2030 Gas Chromatograph (Shimadzu) for H_2 measurement. A pre-established H_2 calibration curve was used to calculate the mass of inactive metallic lithium from the measured H_2 peak area. With the conversion between mAh and mg of Li shown in the following, the percentage of inactive metallic lithium formed after stripping in the total amount of the lithium plated can be calculated.

$$1\ \text{C} = 1\ \text{A} \times \text{s} = 1000\ \text{mA} \times 1/3600\ \text{h} = 1/3.6\ \text{mAh}$$

$$1\ \text{C} = 6.25 \times 10^{18}\ \text{electrons} = 1.038 \times 10^{-5}\ \text{mole of electrons}$$

$$\text{Li}^+ + \text{e}^- = \text{Li}$$

$$1\ \text{mAh} = 3.7368 \times 10^{-5}\ \text{mole of Li} = 0.2594\ \text{mg of Li}$$

The normalized corrosion rate is calculated as the following:

Normalized corrosion rate (μg/day) =

mass loss from the previous measure point (μg)/ time interval from the previous measure point (day)

At least three cells are tested for each measure point by TGC.

4.3 Quantifying Li metal corrosion rates in liquid electrolytes by TGC

First, 0.318 mAh of Li is plated onto a 1.27 cm^2 of Copper (Cu) substrate at a rate of 0.5 mA/cm^2 in a coin cell setup with 55 μL of Bisalt, Nitrate and Gen 2 electrolyte. A relatively thin layer of Li (1.2 μm theoretical thickness) is used to accommodate the calibrated range of the TGC method for high accuracy Li metal quantification. After plating, the deposited Li metal with the Cu substrate is kept in coin cell with the corresponding electrolytes with the open circuit condition (without linked to a cycler). After a certain period of storage time, the cells are disassembled and TGC method is used to quantify the mass of metallic Li^0 remained on the Cu substrate (**Fig. 1a**). The Li mass retention (%) as a function of storage time is shown in **Fig. 1b, 1f and 1j**. For Li plated in all three electrolytes, there is a sudden drop of Li^0 mass in the first 24 hours of resting (**Fig. 1c, 1g and 1k**). A similar trend is also found by Boyle D. T. and his colleagues in their recent work[34], where a fast drop of second cycle coulombic efficiency (CE) is observed after 24 hours of cell resting. After that, the corrosion rates of Li plated in Bisalt and Nitrate electrolytes relatively slow down, which fluctuate at around 0.5 μg/day during 5 weeks of resting. However, a more drastic loss of Li^0 mass is observed in the Gen 2 electrolyte. The continuous corrosion of Li causes a 60.8% loss of Li^0 mass after 5 weeks of resting, especially after 2 weeks of resting when a sudden increase of corrosion rate is observed (**Fig. 1j**).

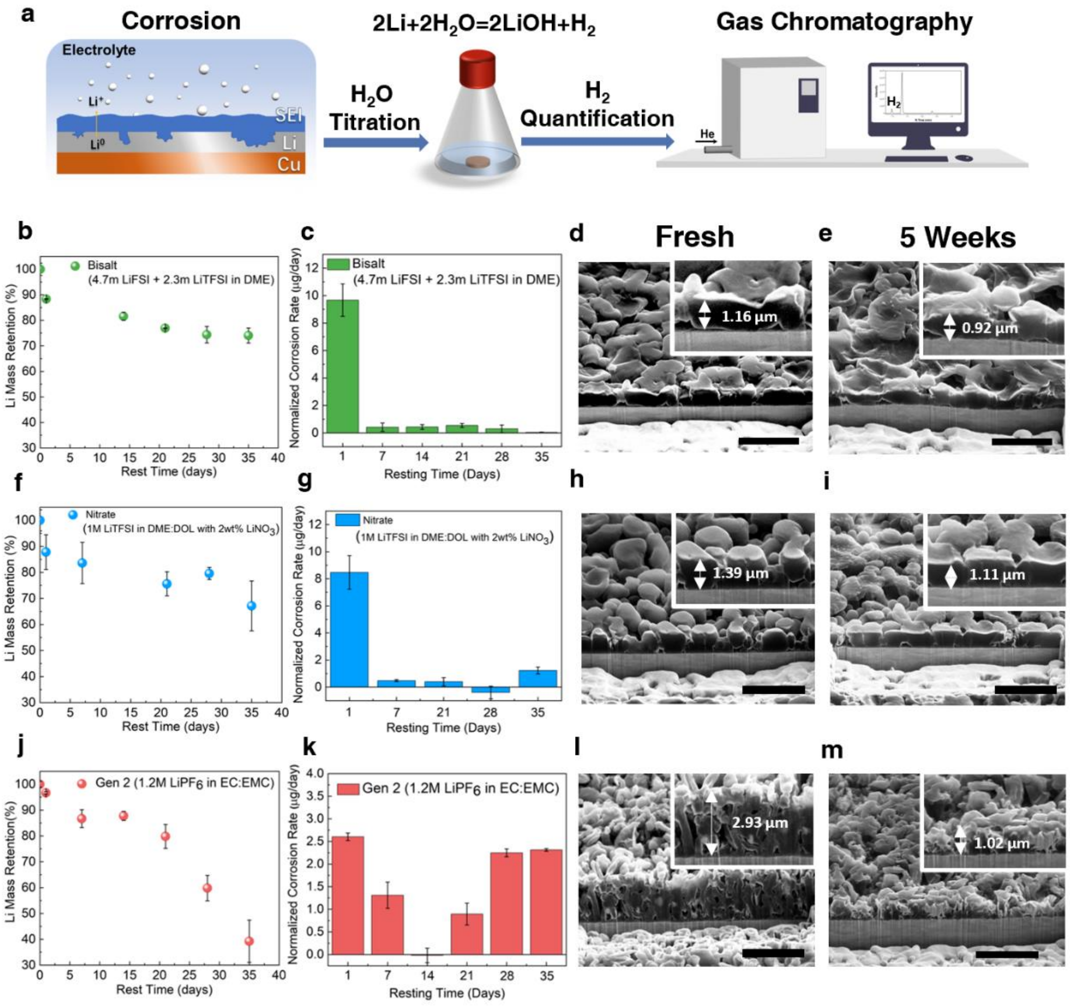

Figure 4.1 The trends of Li metal corrosion in liquid electrolytes. (a) the quantification of Li corrosion by the TGC method. (b-e) The trend of Li metal corrosion in high concentration ether based “Bisalt” electrolyte: (b) the Li mass retention (%) and (c) the normalized corrosion rate of Li (µg/day) as a function of resting time; The SEM images of the Li morphology (d) before and (e) after 5 weeks of resting. (f-i) The trend of Li metal corrosion in ether solvent based “Nitrate” electrolyte: (f) the Li mass retention (%) and (g) the normalized corrosion rate of Li (µg/day) as a function of resting time; The SEM images of the Li morphology (h) before and (i) after 5 weeks of resting. (j-m) The trend of Li metal corrosion in carbonate solvent based “Gen 2” electrolyte: (j) the Li mass retention (%) and (k) the normalized corrosion rate of Li (µg/day) as a function of resting time; The SEM images of the Li morphology (l) before and (m) after 5 weeks of resting. Total amount of 0.318 mAh of Li is plated at a rate of 0.5 mAh/cm^2 with 55 µL of electrolyte amount in all samples. The scale bars represent 5 µm.

The morphological study by Cryo-FIB/SEM further confirmed the corrosion trend obtained by TGC. The Li morphology in Bisalt and Nitrate electrolyte does not experience a significant change before and after 5 weeks of resting in open circuit (**Fig 4.1d-e and 4.1h-i**). The Li retains mostly its granular shape even after the resting period, although there is a decrease of Li thickness in both cases, which corresponds to the loss of Li^0 mass. As expected, a sharp change in the morphology of Li plated in the Gen 2 electrolyte is observed by Cryo-FIB/SEM (**Fig. 4.1l-m**). The freshly deposited Li in Gen 2 electrolyte exhibits a whisker-like morphology, while the corroded Li shows a porous and powder-like morphology. There is also a substantial decrease of Li thickness from 2.93 µm to 1.02 µm, which again agrees with the loss of Li^0 mass quantified by TGC. The three different electrolyte systems, Bisalt, Nitrate and Gen 2, show two drastically different corrosion trends: Bisalt and Nitrate electrolytes show a fast corrosion rate during the first 24 hours, but stabilizes quickly afterward, while Gen 2 shows a continuous corrosion rate throughout the 5 weeks of resting period. A similar corrosion trend study is also done for commercial ultra-thin (50 µm) Li foils (**Fig. 4.2**). It is found that the 50 µm Li foil without Cu substrate lost more active Li^0 mass after one week of immersion than that of the one with Cu substrate, because it has more contact surface area with the electrolyte, further confirming the hypothesis that once the Li||Cu interface is blocked from the electrolyte, the chemical corrosion will not take place in an extensive rate. Whereas in the case of electrochemically deposited Li, since the electrolyte systems tested so far are based on fundamentally different chemistries, the resulted Li might have different SEI components and porosity. Therefore, there might be two possible reasons for the difference in the corrosion trends from the three electrolyte systems: 1) Li metal surface chemistry (SEI); 2) Li metal porosity.

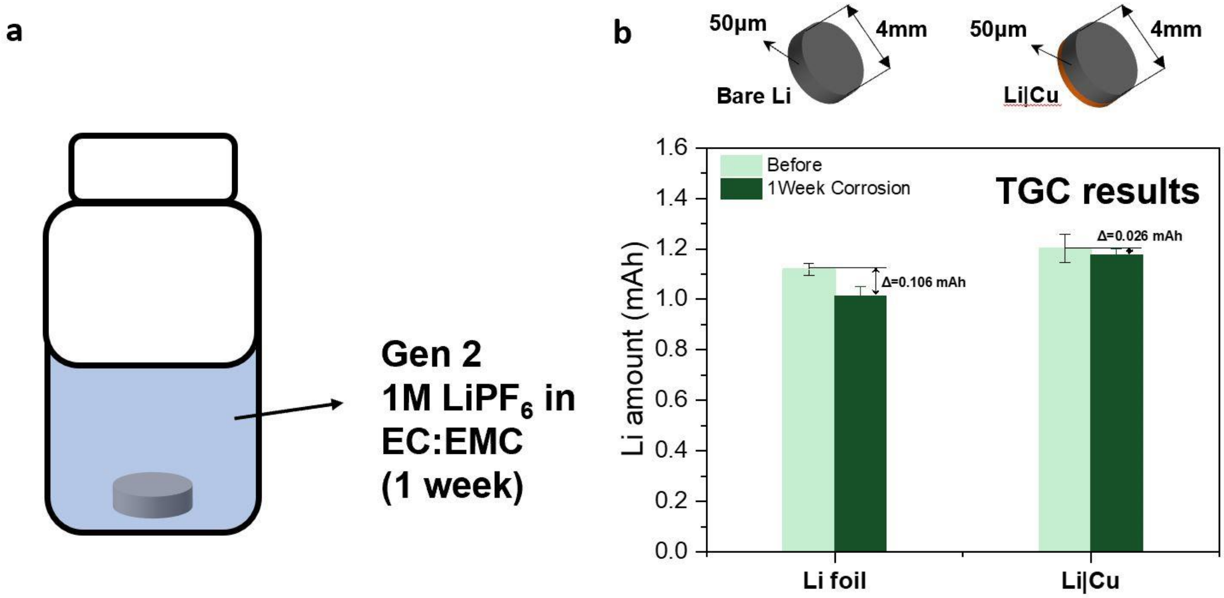

Figure 4.2 The effect of Cu substrate on the Li corrosion rate. (a) schematics of the corrosion test of the pristine Li foil; (b) the quantification results of Li foil before and after immersion in Gen 2 electrolyte (1M $LiPF_6$ in EC:EMC) after one week. Two types of 50 µm thin Li foil, with and without Cu substrate, were punched into 4mm pieces. The punched thin Li foils were then immersed in Gen 2 for one week before taking TGC measurement. It was shown that the Li foil without Cu substrate lost more active Li^0 mass after one week of resting, because it has more contact surface area with the electrolyte.

To elucidate either surface chemistry or porosity dominates the corrosion rate resulting from the three electrolyte systems, X-ray Photoelectron Spectroscopy (XPS) with depth profiling is performed on the freshly deposited and corroded Li metal to verify the interphases chemical information (**Fig. 4.3**). We identified that the fresh SEI components in all three electrolyte systems are almost identical. In both Bisalt and Nitrate samples, the change of C-F implies the presence of Li salt (LiTFSI and LiFSI) on the surface of the Li, which can be confirmed by 533 eV peak in O 1s and (C-F at 293 eV and C-S=O at 289 eV) eV peaks in C 1s as well. Other than the Li salts, Li-F, Li_2O and typical organic species such as C-O/C=O/ROLi can be well located, which is consistent with previous literature results[74,122] **Fig. 4.3c** demonstrates the results from Gen 2 sample, which is quite like the Bisalt samples considering the major components include Li-F, Li_2O and typical organic species in the freshly deposited samples. After 3 weeks of resting, in the

Bisalt samples, there is an accumulation of Li salt in the surface of the Li, while other SEI components still preserve well in the surface layers. Similar to the Bisalt case, SEI components in the Nitrate sample also preserve well after 3 weeks of resting. However, in the Gen 2 case, the Li_2O content mostly disappears after 3 weeks of resting. The surface layers mainly consist of LiF after the corrosion. The results of Gen 2 samples show that the SEI layers have undergone a significant change during the resting period (highlighted by blue and violet hades), which correspond to the corrosion trend of the Li deposited in Gen 2 where a fast corrosion rate is observed throughout the 5 weeks of resting (**Fig. 4.1j**). Based on the results so far, it can be observed that in the case of Bisalt and Nitrate electrolytes, where ether-based solvents are used, the SEI components are much more stable than that of the Gen 2 electrolyte. Although XPS depth profiling can provide us valuable information about the SEI components evolution during the corrosion period, the exact SEI structure of the Li deposited from each electrolyte remains unclear. Furthermore, the deconvoluted inorganic SEI components generated in the three electrolyte systems are mostly Li_2O, LiF, Li_2CO_3. There is no big difference in the inorganic parts of the SEI layers among the three electrolytes. The reason for the high stability of SEI layers generated in the ether-based electrolyte might be the organic parts in the SEI layers (**Fig. 4.4**). More work should be done to carefully examine the nano-structure and the organic components of the Li SEI, which might be the key in determining the stability of the SEI layers. The importance of a stable SEI layer also reflected in the slow corrosion trend in the Bisalt and Nitrate samples. Therefore, we believe that the SEI layers need to be strong enough to survive the corrosion process to mitigate the continuous mass loss of Li in liquid electrolyte.

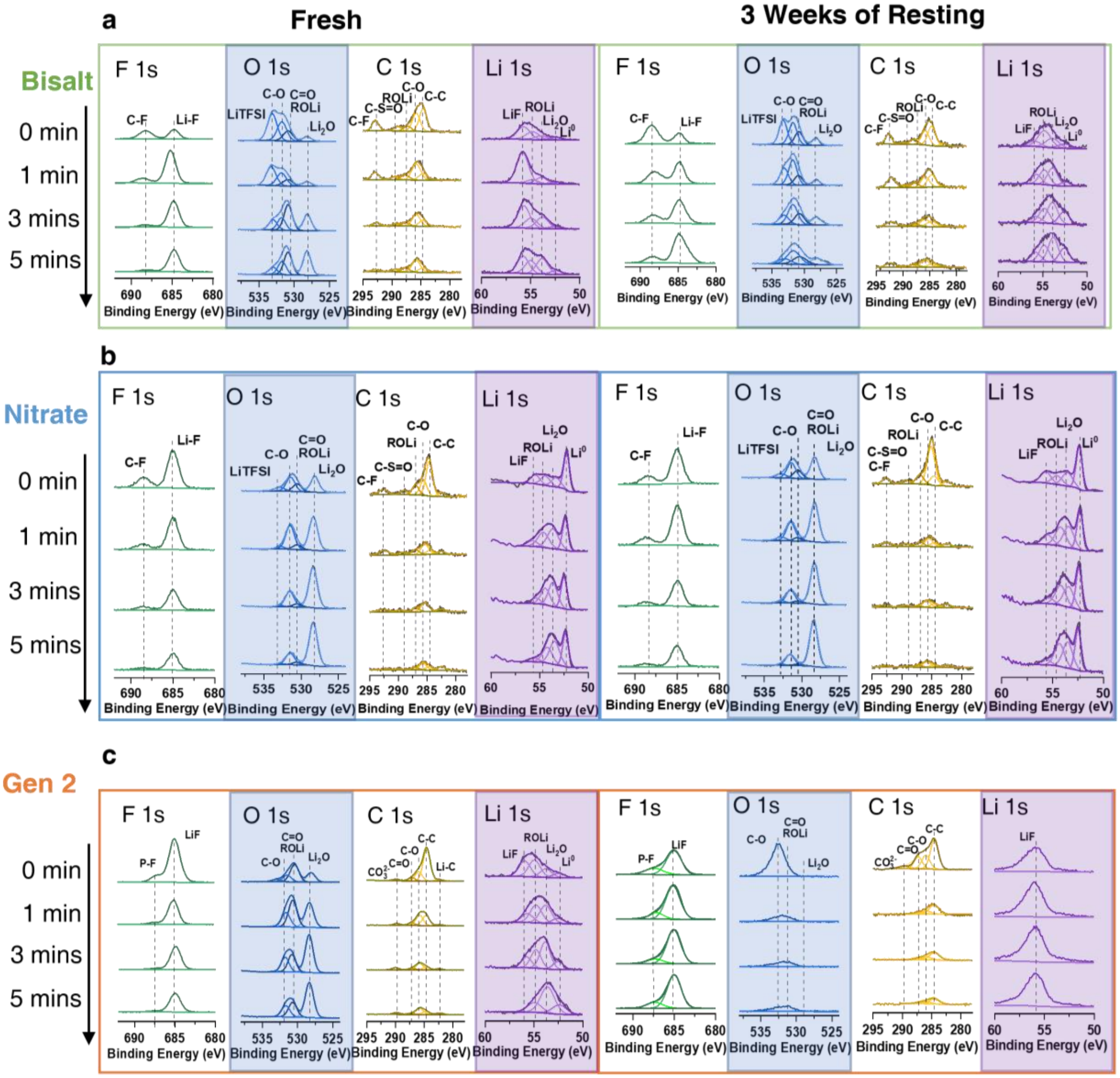

Figure 4.3 The XPS depth profiling of deposited Li metal. Chemical evolution of F 1s, O 1s, C 1s, and Li 1s of (a) Bisalt electrolyte and (b) Nitrate electrolyte (c) Gen 2 electrolyte before and after 3 weeks of resting in its corresponding electrolyte.

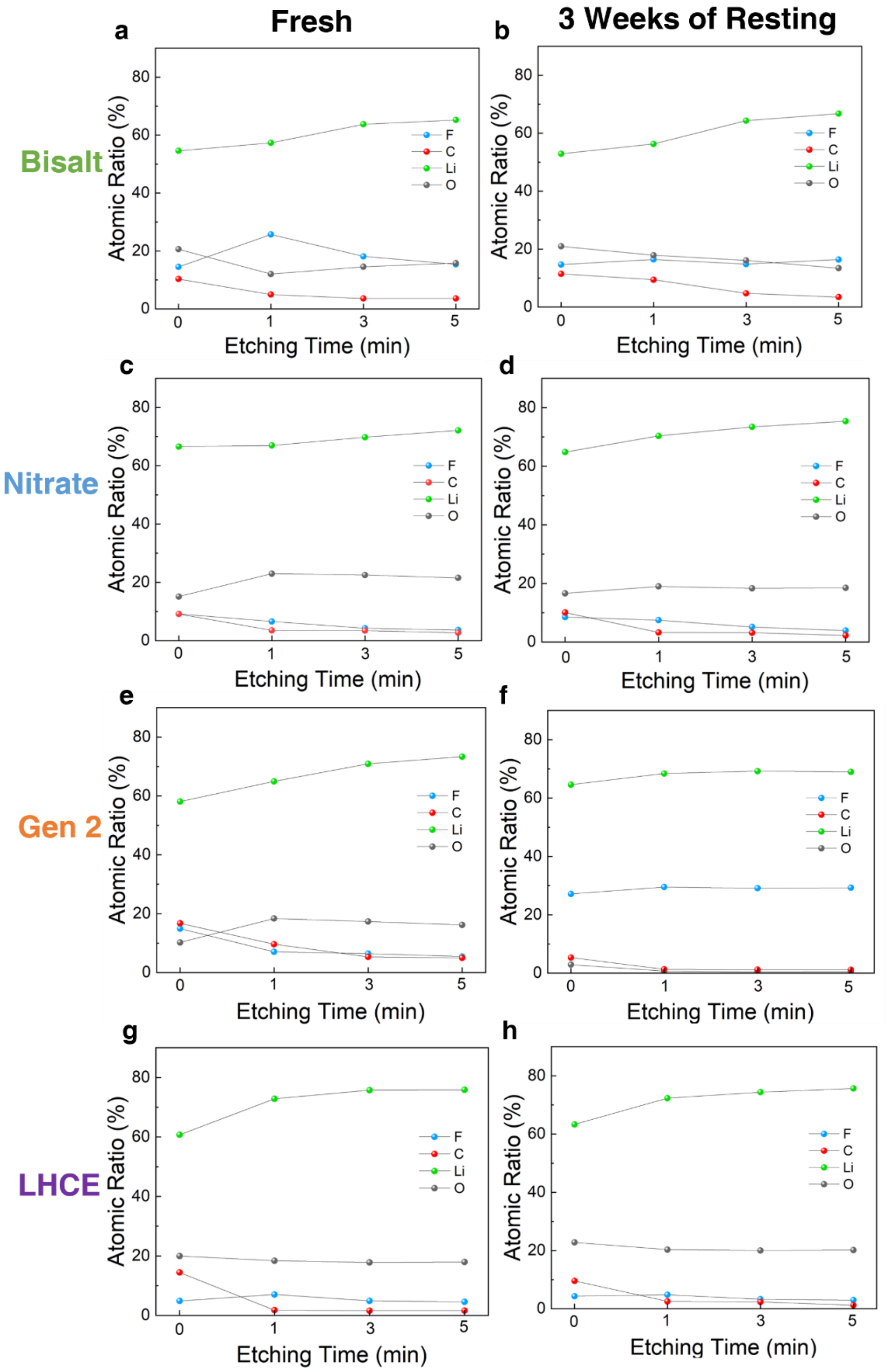

Figure 4.4 Quantified elemental ratios of SEI components at different etching times for Li metal in Bisalt after (a) freshly deposited and (b) after 3 weeks of resting, in Nitrate after (c) freshly deposited and (d) 3 weeks of resting, in Gen 2 after (e) freshly deposited and (f) 3 weeks of resting, and in LHCE after (g) freshly deposited and (h) 3 weeks of resting.

4.4 Effect of porosity on the Li corrosion rate

Our previous work has shown stacking pressure could effectively control the porosity of deposited Li[125]. To investigate the effects of Li porosity on the corrosion rate, a split cell together with a pressure sensor is used for controlling the stacking pressure during Li plating (**Fig. 4.5a**), which can help us to obtain deposited Li with different porosities. Similar to the previous case, 0.318 mAh of Li is plated onto Cu substrate at a rate of 0.5 mAh/cm^2 in Gen 2 electrolyte. However, the electrode size is changed from 1.27 cm^2 to 0.385 cm^2 to accommodate the smaller size of the split cell. Two different stacking pressures, coin cell pressure (150 kPa) and optimized Li plating pressure (350 kPa), are applied during the Li plating process. The plated Li with the Cu substrate is recovered from the split cell and immersed in flooded electrolyte (~1mL) for corrosion study. **Fig. 4.5b** shows the Li^0 mass retention (%) of the Li plated under two pressures. The lower porosity of the Li plated under 350 kPa helps to suppress the Li corrosion rate. The metallic Li^0 lost about 18% of its original mass as a contrast to 29.2% in the case of coin cell pressure. When comparing the improved Li corrosion trend to that of Li plated in Bisalt electrolyte under coin cell pressure, it is found that the two corrosion trends are similar (**Fig. 4.5c**), meaning that with the optimized stacking pressure applied during Li plating, the resulting low porosity Li can have a limited corrosion rate even in conventional carbonate electrolyte. The cryo-FIB/SEM images also illustrated the morphological change of the Li plated under different pressures before and after corrosion. From the top-view and cross-sectional images of the Li plated under coin cell pressure, the resulting Li is in whisker-like morphology (**Fig. 4.5d and 4.5h**). However, just after 7 days of immersion in Gen 2 electrolyte, there is a noticeable shrinkage in both the plated Li's thickness and the diameter of whiskers. On the contrary, the morphology of Li plated under 350 kPa pressure did not show a significant change. The Li retained its dense morphology after 7 days of immersion, especially in the cross-section. The only noticeable change happens on the top surface of the dense Li where some flower-like materials begin to form on the surface. The effect of porosity on corrosion rate for low concentration ether-based electrolyte (LCE,1M LiTFSI in DME:DOL) is also conducted (**Fig. 4.6**). A similar fast corrosion trend of the Li plated in the Gen 2 (**Fig. 4.6a, 4.6c**) is also observed in the Li plated in the LCE, where porous Li whiskers are grown (**Fig. 4.6b, 4.6d**). With the results so far, it can be seen that the Li corrosion only takes place at the interface between Li and the electrolyte. Even when Li is deposited in the ether-based electrolyte (LCE), which is believed to generate more stable SEI, because of the high porosity of the deposited Li, the corrosion rate of Li in LCE is considerably higher than that of the Bisalt and Nitrate electrolytes. Therefore, the porosity of the plated Li should play a major role in controlling the corrosion rate of Li.

To validate if the Li electrode porosity is the dominating factor of corrosion rate, we selectively deposited Li in Gen 2 electrolyte, with a range of stacking pressure applied during Li plating to plate Li with different porosities. Cryo-FIB/SEM is used to obtain the 3D reconstruction of the plated Li and calculate its porosity (**Fig. 4.5l-o**). The as-plated Li is then immersed into the Gen 2 electrolyte and rest for three weeks. The Li^0 mass loss is used for calculating the corrosion rate of the Li using the following equation[113]:

$$R = \frac{\Delta m}{A_S T}$$

where Δm is the change in mass, A_s is the electrode area, and T is the corrosion time. The detailed calculated parameters are listed in **Table 4.1** in the supporting information. As shown in **Fig. 4.5p**, the calculated Li corrosion rate directly correlates with the plated Li's porosity. The results further validated our hypothesis that the porosity of the plated Li is the major factor in determining the Li corrosion rate.

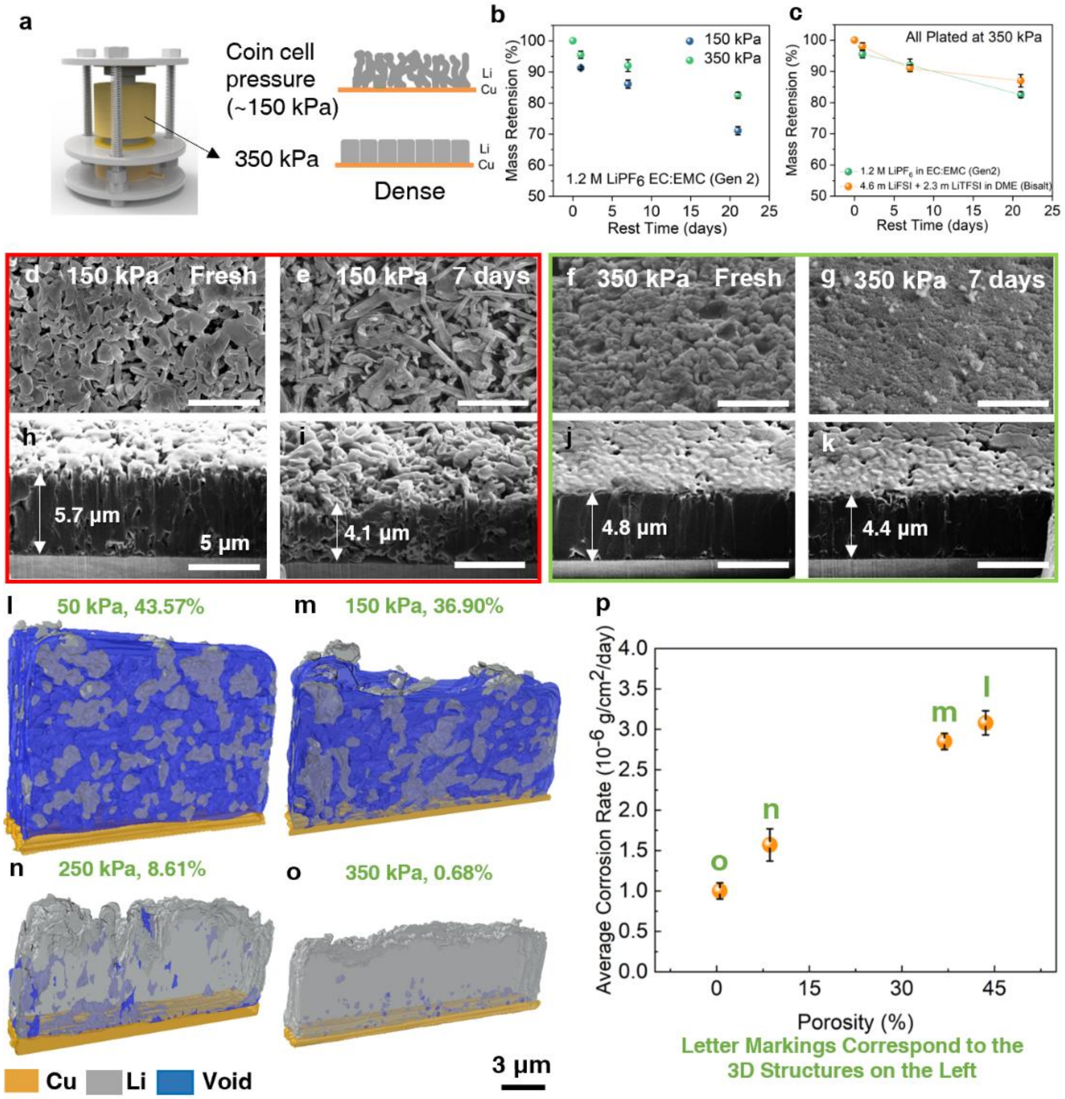

Figure 4.5 The effect of morphology control on limiting the corrosion of Li in liquid electrolyte. a) Schematics of stacking pressure control set up. (b) Trend of Li^0 mass retention (%) of Li plated under 2 different stacking pressure (coin cell pressure and 350 kPa pressure) in Gen 2 electrolyte. (c) The comparison between Li^0 mass retentions (%) of Li plated in Gen 2 electrolyte with 350 kPa and in Bisalt electrolyte in coin cell. (d-k) The top-view and cross-sectional SEM images of the deposited Li metal in Gen 2 electrolyte: under coin cell pressure after (d, h) freshly deposited, (e, i) after 7 days of resting and under 350 kPa pressure after (f, j) freshly deposited, (g, k) after 7 days of resting. The 3D reconstruction of deposited Li metal plated under different stacking pressures resulting in different Li porosities: (l) 50 kPa and 43.57% porosity; (m) 150 kPa and 36.90% porosity; (n) 250 kPa and 8.61% porosity and (o) 350 kPa and 0.51% porosity. The Li metal corrosion rate as a function of Li porosity: (p) The Li metal corrosion rate and its correlation with the porosity of the freshly deposited Li. All Li is plated in Gen 2 electrolyte. Total amount of 0.318 mAh of Li is plated at a rate of 0.5 mA/cm^2 for all samples.

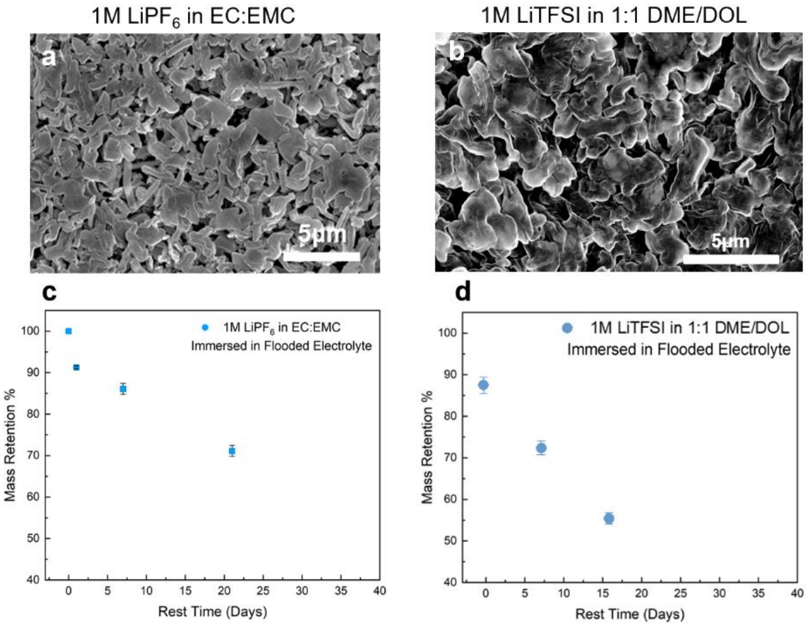

Figure 4.6 The effect of surface area on corrosion rate. The top-view SEM images of plated Li in (a) Gen 2 electrolyte; (b) 1M LiTFSI in DME:DOL; The Li^0 mass retention (%) as a function of resting time in (c) Gen 2 electrolyte; (d) 1M LiTFSI in DME:DOL; Total amount of 0.318mAh of Li is plated at a rate of 0.5mAh/cm^2 in all samples.

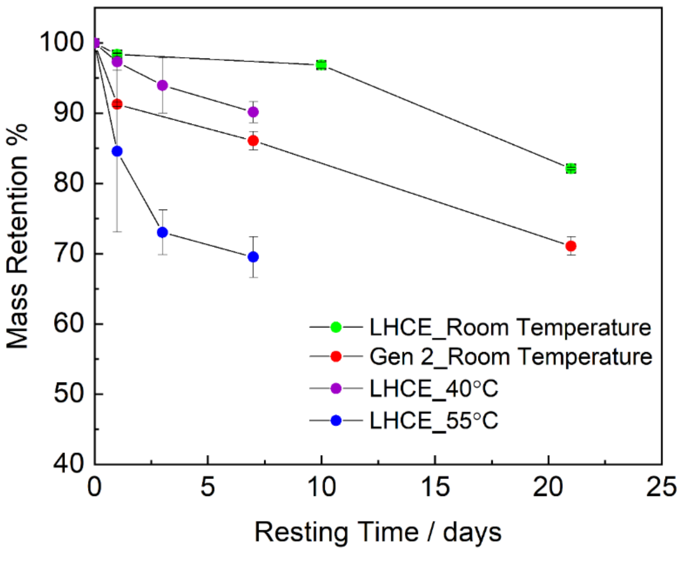

Figure 4.7 Trend of Li^0 mass retention (%) of Li deposited in Gen 2 and LHCE at various temperatures.

Table 4.1 The detailed quantification of Li^0 mass loss and its corresponding corrosion rate.

Sample	Porosity	Mass loss (After 3 weeks)	Corrosion rate ($g/cm^2/day$)
High porosity (Coin cell)	43.57%	$2.49*10^{-5}$ g	$3.08*10^{-6}$
Medium porosity (150 KPa)	36.90%	$2.30*10^{-5}$ g	$2.85*10^{-6}$
Low porosity (250 KPa)	8.61%	$1.27*10^{-5}$ g	$1.57*10^{-6}$
Dense (350 KPa)	0.51%	$0.81*10^{-5}$ g	$1.00*10^{-6}$

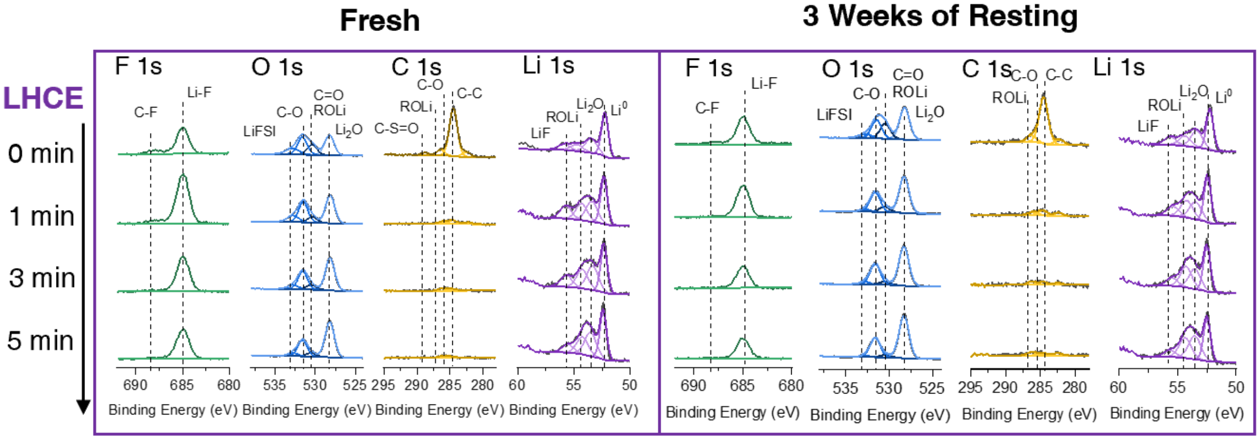

Figure 4.8 The XPS depth profiling of F 1s, O 1s, C 1s, and Li 1s of Li deposited in LHCE before and after 3 weeks of resting.

4.5 Suppressing Li metal corrosion: advanced electrolyte and optimal stack pressure

With the results so far, it can be concluded that the controlling interface between Li and electrolyte is the key in suppressing the chemical corrosion of Li in liquid electrolytes: the contact area needs to be minimized while maintaining a robust SEI layer. To further demonstrate the feasibility of limiting the Li corrosion by controlling the porosity of Li, a novel electrolyte system, the localized high concentration electrolyte (LHCE)[122], with LiFSI:DME:TTE in a molar ratio of 1:1.2:3 is used to plate Li under different stacking pressures. By applying the optimized stacking pressure of 350 kPa during Li plating, ultra-low porosity was achieved for deposited Li, which results in less than 0.8% of metallic Li loss after 10 days of resting in LHCE electrolyte (**Fig. 4.9a**). The corrosion of the metallic Li is significantly mitigated by minimizing the contact area between

Li and electrolyte. As shown in **Fig. 4.9b and 4.9c**, the dense Li morphology is well retained even after 21 days of immersion in the LHCE electrolyte. In addition to the dense morphology, the SEI layers of the Li deposited in LHCE is also quite stable. After three weeks of resting, there is no observable changes in the SEI components (**Fig. 4.8**). Even at elevated temperature of 40℃, the corrosion rate of Li is lower than that of Gen 2 electrolyte (**Fig. 4.7**). However, when the resting ambient temperature is raised to 55℃, a fast corrosion rate is observed for LHCE (**Fig. 4.7**). More work needs to be conducted to find out ways to mitigate the corrosion of Li metal at elevated temperatures.

Overall, the strategies of suppressing the Li corrosion in liquid electrolytes should focus on three parts. First and most importantly, an optimized stacking pressure should be applied during Li plating to achieve a dense and uniform Li morphology. Since the corrosion of Li requires contact with the liquid electrolyte, by limiting the surface area (porosity) of the plated Li, the corrosion rate of Li during resting period can be effectively mitigated. Second, a dense and stable interface should be constructed during plating, which can be achieved mainly by using an advanced electrolyte system such as LHCE. A stable interface can further block the charge exchange between Li and the liquid electrolyte, thus limiting the corrosion of the plated Li. Lastly, more work should be done to design a dense but flexible surface coating that can be tightly applied on Li surface and retain its structural integrity during cycling[126], and possibly further mitigate the corrosion of Li metal at elevated temperatures. In this way, the total blockage of charge transfer between Li and liquid electrolyte can be achieved throughout the resting period, and the corrosion of Li metal can be further mitigated.

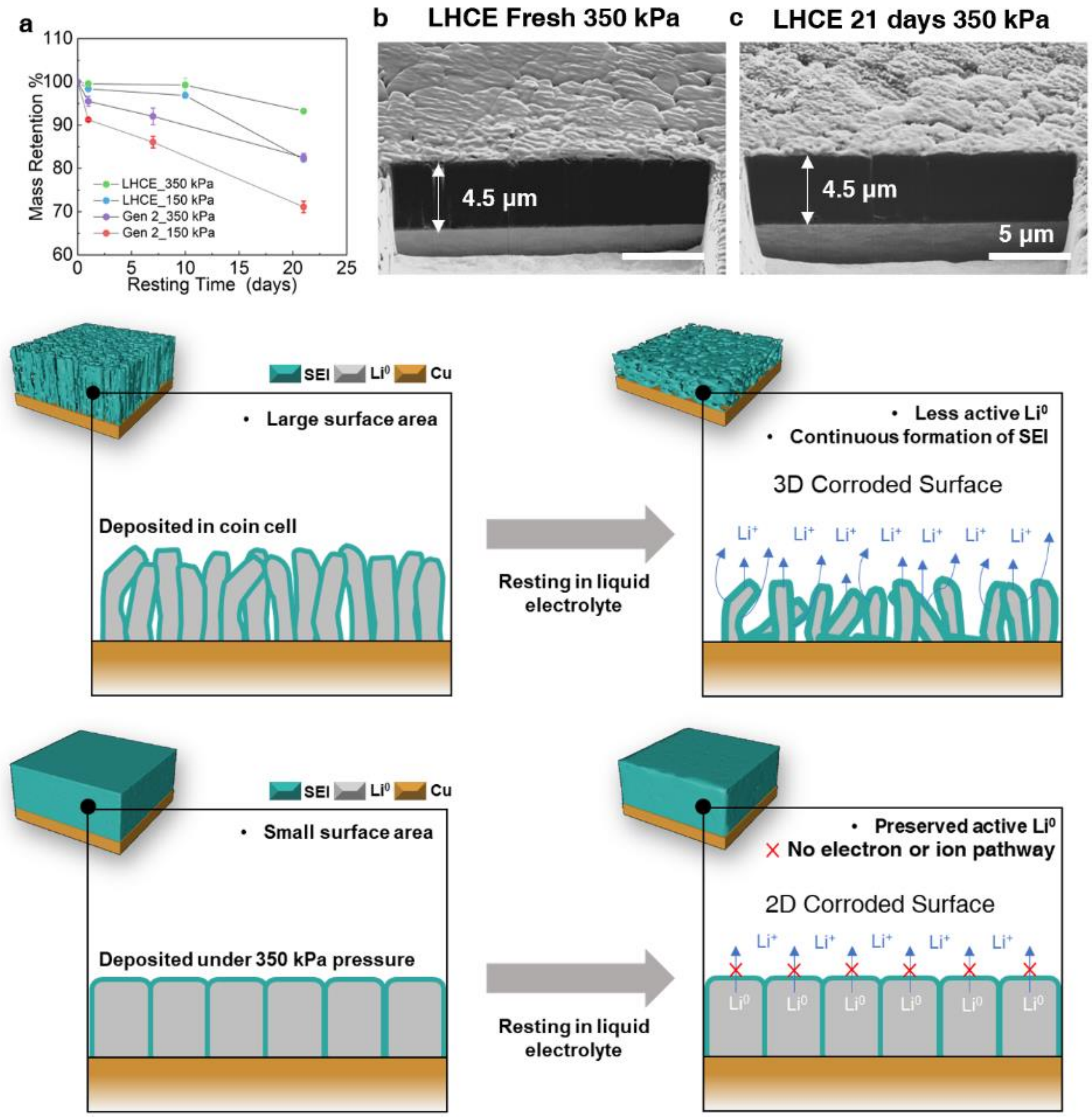

Figure 4.9 Controlling the corrosion of Li metal in liquid electrolytes. (a) Trend of Li^0 mass retention (%) of Li deposited in Gen 2 and LHCE (LiFSI:DME:TTE in molar ratio of 1:1.2:3) under coin cell and 350 kPa pressure. Cross-sectional images of Li plated in LHCE under 350 kPa pressure (b) after freshly deposited and (c) after 21 days of resting. (d) Schematics of possible ways to suppress the Li metal corrosion in liquid electrolyte. Total amount of 0.318 mAh of Li is plated at a rate of 0.5 mA/cm^2 in all samples. The schematics of the relationship between the Li morphology and its corrosion trend. The high porosity Li whiskers plated in coin cell setup will have a high contact surface area with the liquid electrolyte, inducing continuous chemical corrosion of Li. The low porosity Li plated under optimized stacking pressure has only a 2D contact surface area with the liquid electrolyte, which largely limits the chemical corrosion of Li in the liquid electrolyte.

4.6 Conclusion

We systematically studied the corrosion rate of Li in liquid electrolytes regarding: 1) Li surface chemistry; and 2) Plated Li porosity. For the Li surface chemistry, it was found that the major SEI components mainly consist of LiF, Li_2O, and organic Li containing species for plated Li in both ether and carbonated based electrolytes. The plated Li with a well-controlled porosity shows drastically decreased corrosion rate even in Gen 2 electrolyte, illustrating that the most crucial parameter in determining the corrosion rate of Li is the contact surface area between Li and liquid electrolyte, which is the porosity of the Li. By using advanced electrolyte (LHCE) and optimized stacking pressure (350 kPa) for Li deposition, the ultra-low porosity Li is plated, which only has a 2D contact surface area with the liquid electrolyte. The low contact surface area helped the dense Li to stabilize in the liquid electrolyte and the Li loses only about 0.8% of its active mass after 10 days of immersion in liquid electrolyte. The work here has shown that by controlling the contact area between Li and liquid electrolyte can help to effectively suppress the corrosion of Li.

Chapter 4, in full, is a reprint of the material "Suppressing Chemical Corrosions of Lithium Metal Anodes" as it appears in the Advanced Energy Materials, Bingyu Lu, Weikang Li, Diyi Cheng, Bhargav Bhamwala, Miguel Ceja, Wurigumula Bao, Chengcheng Fang, Ying Shirley Meng, 2022, 2202012. The dissertation author was the primary investigator and author of this paper. The author wrote the paper.

Chapter 5. Key Parameters in Determining the Reactivity of Lithium Metal Battery

5.1 Introduction

With the rapid growth in the demand of high performance electric vehicles and personal portable devices, lithium (Li) metal has been a popular candidate as the anode material for developing high energy density rechargeable batteries (> 500 Wh/kg) due to its high specific capacity (3,860 mAh/g) and low electrochemical potential (–3.04 V versus the standard hydrogen electrode)[3,6,59]. Although extensive studies have been performed to prolong the cycle life of Li metal anode[56,62,92], the potential safety hazard brought by metallic Li in the high energy density batteries is still one of the biggest obstacles before its commercialization with large-scale[127]. The first attempt to commercialize Li metal cells in the 1980s ended up as a failure when multiple cases of cells catching on fire were reported[128]. Since then, the safety concerns of using Li metal as the anode material for high energy cells have never ceased[129].

The safety hazards at cell level is determined by the reactivity of each cell component and the interplay among them[130]. As for commercial Li-ion battery, there has been tremendous work studying the key factors in determining the reactivity of Li-Gr[42–44]. By utilizing accelerating rate calorimetry (ARC) and X-ray diffraction (XRD), Dahn et al discovered that the lithiated Graphite ($Li_{0.81}C_6$) starts to decompose with electrolyte at temperatures as low as 90°C[45]. In situ synchrotron XRD and mass spectrometry (MS) were applied by Amine et al to study the role of robust SEI in protecting lithiated graphite from thermal decomposition. Based on the current literature, it can be concluded that the lithiated graphite (Li-Gr) at material level is far from a safe and stable material, but can be implemented in state-of-the-art battery packs with proper engineering and optimizations[46–48]. As a highly reactive alkali metal, Li has always been considered unsafe for practical battery operations[131,132]. Various attempts have been made to design a safe rechargeable

Li metal cell. Novel electrolyte with non-flammable solvents is one of the most effective ways to prevent the cell from catching on fire[49–51]. Fire-retarding localized high concentration electrolytes (LHCEs) have also been developed using non-flammable solvents or diluents, such as trimethyl phosphate or 2,2,2-trifluoroethyl-1,1,2,2-tetrafluoroethyl ether (HFE)[52,53]. Recently, Yin and his colleagues developed a new type of liquefied gas electrolyte with fire extinguishing merit[51]. With the development of electrolyte, the Li metal anode is marching towards a commercial reality with safe operation.

Although these works have been done focusing on preventing cells from catching on fire, it is still unclear how reactive Li metal is in nature, not to mention a direct comparison with other anode materials under similar state of charge. It is commonly believed that the pristine Graphite and Si are much safer than Li metal when assembled in a cell. However, in practical applications, the battery is mainly in the charge state in which the anode is lithiated, and its chemical stability is reduced significantly. Therefore, the reactivity of Li metal should be compared with that of Li-Gr and Li-Si, instead of the pristine ones. More work needs to be done to identify the key parameters in controlling the reactivity of Li metal in a battery system and provide designing principles for safe Li metal battery (LMB). There are multiple ways to define the metal reactivity under different cirtumstances.[55] For instance, a metal is considered highly reactive when 1) it causes large negative enthalpy of formation, ΔH_f, during a oxidation reaction, or 2) requires small sublimation energy and ionization energy during oxidation or hydration[55]. Since the anode at charged state is full of electrons to be released, which can also react with water and oxygen violently[56], it is important to *quantitatively* compare the reactivity of different anode materials in a well-controlled cell system.

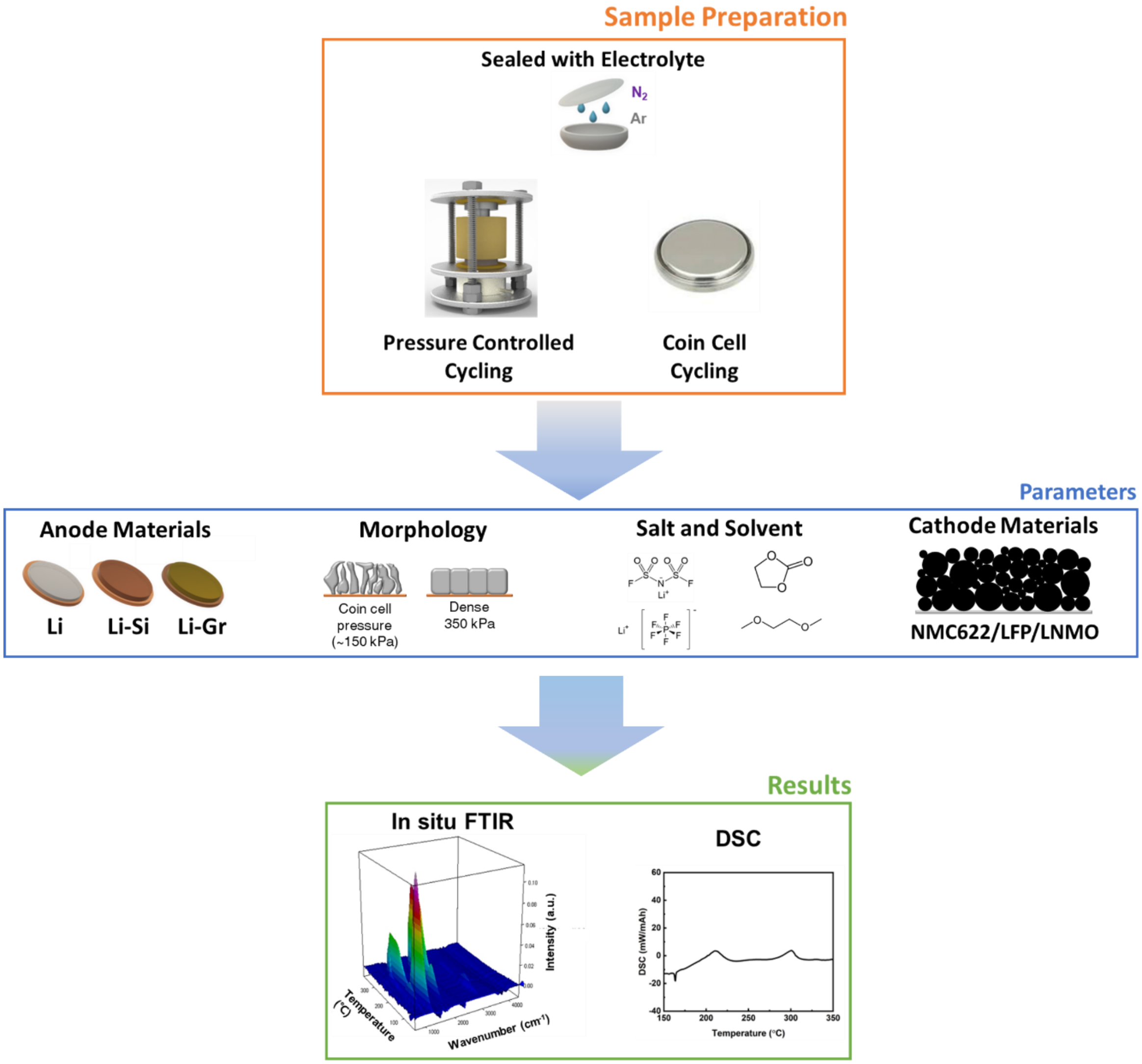

Figure 5.1 The schematics of the sample preparation and experimental process.

Here, we quantitatively compare the reactivity of Li-Gr, Li-Si, and plated Li metal (plated-Li) in two different electrolytes by utilizing the differential scanning calorimetry (DSC) coupled with in situ Fourier-transform infrared spectroscopy (FTIR). We further explored the effect of Li morphology on the reactivity by precisely tuning the external stack pressure during the plating process. It was found that the thermal response of plated-Li metal in a well-designed system can be on the same magnitude as that of Li-Gr and Li-Si. Furthermore, the influence from the cathode on the Li metal reactivity is also analyzed. Finally, a guideline for designing safer Li metal cells is provided.

5.2 Methods

5.2.1 Electrolyte preparation

Battery-grade lithium bis(fluorosulfonyl)imide (LiFSI) was purchased from Oakwood Products, Inc.; Bis(trifluoromethane)sulfonimide lithium 99.95% (LiTFSI) was purchased from Sigma-Aldrich. All salts were further dried at 120 °C under vacuum for 24 h before use; 1,2-dimethoxyethane (DME) anhydrous, 99.5% was purchased from Sigma-Aldrich; 1,1,2,2-tetrafluoroethyl-2,2,3,3-tetrafluoropropyl ether (TTE, 99%) was ordered from SynQuest Laboratories. Solvents were dried with molecular sieves before use. LiFSI–DME–TTE were mixed in a molar ratio of 1:1.2:3 to prepare the LHCE. The carbonate electrolyte, 1.2 M Lithium hexafluorophosphate (LiPF6) dissolved in ethylene carbonate (EC): diethyl carbonate (DEC) (1:1 by weight) with 10% fluoroethylene carbonate (FEC) was purchased from Gotion. The All-F electrolyte was directly made by Gotion with formula provided by UCSD. All procedures were performed in an argon gas filled glove box (<0.1 ppm O_2, <0.1 ppm H_2O).

5.2.2 Electrochemical Testing

For Li||Cu cells, the cleaned Cu pieces was assembled in the 2032 coin cell as the working electrode while the Li metal (0.1 mm thick, China Energy Lithium Co., Ltd.) was the reference and counter electrode. Celgard 2325 separator was used as the separator and soaked in 55 µL of electrolyte. The Graphite and Silicon half cell were cycled at room temperature at a rate of C/20 during the first cycle and C/10 for subsequent cycles. The Graphite half cells are cycled between 0.05V to 2V while the Silicon half cells are cycled between 0.05V and 1.5V. For the full cell testing, the Graphite and Silicon electrode was paired with an LFP, NMC622, coated NMC622 or

LNMO cathode and assembled in a 2032 type coin cell. The full cells were charged at room temperature at a rate of C/10 to 3.8V for LFP, 4.4V for NMC622 and coated NMC622 and 4.85V for LNMO. All cell makings were performed in an argon gas filled glove box (<0.1 ppm O_2, <0.1 ppm H_2O).

5.2.3 Pressure controlled split cells

A custom-made split cell that consists of two titanium plungers (1/2-inch diameter) and one polyether ether ketone (PEEK) die mold (1/2-inch inner diameter) is used for the pressure controlled Li plating. The Cu||Li cells were made by sandwiching the Li metal foil (7 mm diameter, 50 μm thick, China Energy Lithium Co., Ltd.), Celgard 2325 separator (1/2 inch diameter) and the cleaned Cu foil between the two titanium plungers inside the PEEK die mold. Only minimum amount of electrolyte (~5 µL) was added to the Cu||Li cells to wet the separator. After the assembly, the split cell and the load cell were put into the cell holder, which provided the uniaxial stacking pressure. The uniaxial stacking pressure was adjusted by the three screws on the cell holder. The screws were carefully adjusted to apply the desired stacking pressure to the split cell while keeping both the split cell and the load cell in vertical position. The cell was tested inside the glovebox using Landt CT2001A battery cycler (Wuhan, China). Various current densities and stacking pressure were applied to conduct the study as indicated in the main text.

5.2.4 Cryogenic Focused Ion Beam- Scanning electron Microscopy (Cryo-FIB/SEM)

The copper foil with deposited Li was recovered from the split cell and then washed with DME to remove the residual electrolyte in the Ar-filled glovebox. The sample was mounted on a SEM stub (Ted Pella) in the glovebox, then transferred to a FEI Scios DualBeam FIB/SEM system with an Air-tight transfer holder to minimize air exposure[124]. Liquid N_2 was used to cooled down the sample stage to -180˚C to create a cryogenic environment which helps minimize beam damage to the sample. Gallium ion beam with a voltage of 30 kV, current of 7 nA and dwell time of 100 ns was used to roughly mill down the cross-section of the deposited lithium. After the rough milling, the cross-section was cleaned with ion beam at 1 nA. The SEM image of the cross-section was taken using Everhart-Thornley Detector (ETD) at 5 kV and 0.1 nA.

5.2.5 ALD coating for NMC

For the ALD process, the calendared cathode was first stored in a 60 ℃ oven overnight to remove the moisture, then transferred to the ALD chamber. The deposition of Al_2O_3 requires trimethylaluminum (TMA) as the precursor and water as the reactor. The carrier gas was nitrogen in 300 mbar, and the reaction temperature was 100 °C. The deposition rate was 1.0 Å per cycle. The surface layer thickness on the electrodes was controlled through the number of cycles performed. To ensure the precursor gas could spread into the electrode, a pre-injection of TMA for 6 seconds was applied. In the rest of the cycles, the TMA dose time was 0.6 s, followed by 1 s TMA purge, and the moisture dose time was 0.2 s, followed by 1 s purge. A vacuum-drying process at 80 °C for at least 24 h was then applied to the surface-modified electrode before any electrochemical testing to remove any residual moisture.

5.2.6 Differential scanning calorimetry - Fourier-transform infrared spectroscopy (DSC-FTIR)

The DSC-FTIR measurement was done on NETZSCH STA 449 F3 Jupiter with an in-line coupled system of Bruker ALPHA II FTIR. The cycled electrodes were first retrieved from the coin cells and seal in a Cu backed Al pan with controlled amount of electrolyte (~3 g/Ah). All sample preparations were performed in an argon gas filled glove box (<0.1 ppm O_2, <0.1 ppm H_2O). The Al pan was pierced by a needle after loading into the DSC chamber so that the evolved gas could be analyzed by the in-line FTIR. During the DSC-FITR measurement, the temperature was ramping up at a rate of 10°C/min to 400°C. All DSC-FTIR measurement were done under Ar and N_2 environment.

Table 5.1 The boiling point of all the electrolyte solvents used in the study.

Solvent	Boiling Point (˚C)
DME	85.0
TTE	93.2
DEC	127.0
EC	243.0
FEC	212.0
FEMC	90.0

5.3 DSC of Li anodes after 1 cycle

Three anodes including Gr, Si and bare Cu (no excess Li) were charged with the controlled lithiation/plating amount of 3 mAh/cm^2 for Gr or 5 mAh/cm^2 for Si and bare Cu in the half cell, as shown in **Fig. 5.1**. Instead of 5 mAh/cm^2, 3 mAh/cm^2 capacity is chosen for the Gr because it is the most widely available capacity among commercialized Li-ion cells. The prepared anodes were sealed in a DSC pan with controlled amount of electrolyte (E/C ratio ~ 3mg/mAh), and then transferred into the DSD-FTIR station for thermal analysis. Detailed experimental designs can be found in Supplementary information. **Fig. 5.2** shows the DSC curves of Li-Gr, Li-Si, plated-Li in the carbonate-based electrolyte (Carbonate, 1.2 M Lithium hexafluorophosphate ($LiPF_6$) dissolved in ethylene carbonate (EC): diethyl carbonate (DEC) (1:1 by weight) with 10% fluoroethylene carbonate (FEC)). In addition, plated-Li in LHCE (Lithium bis(fluorosulfonyl)imide (LiFSI), 1,2-dimethoxyethane (DME) and 1,1,2,2-Tetrafluoroethyl-2,2,3,3-Tetrafluoropropyl Ether (TTE) with molar ratio 1:1.2:3) was also prepared. In both Li-Gr and Li-Si, most heat-absorbing peaks are associated with the evaporation of electrolyte solvents such as DEC and EC (**Fig. 5.2a, b, Table 5.1**). No significant heat-releasing peaks exist in the Li-Gr and Li-Si samples when heated up to 400°C. However, when the plated-Li in the Carbonate is heated during the DSC measurement, two heat-releasing peaks overlap with the evaporations of DEC and EC solvents, respectively (**Fig. 5.2c**). When Li melted at around 180°C, a sharp heat-absorbing peak appeared. The exothermic reactions might be caused by the melted Li quickly reacting with the remaining EC solvent and $LiPF_6$ salt. **Fig. 5.2d** shows the DSC curves of the plated-Li in LHCE electrolyte. The DME and TTE solvents are mostly evaporated before 100°C because of the low evaporation points, rather than reacting with the Li. A sharp Li melting peak is also shown around 180°C in **Fig. 5.2d**, which indicates that the Li was mostly melted rather than oxidized during the heating process. A small oxidation peak can be observed after the complete melting of Li, which is associated with the decomposition of electrolyte salts (details in **Fig. 5.3**).

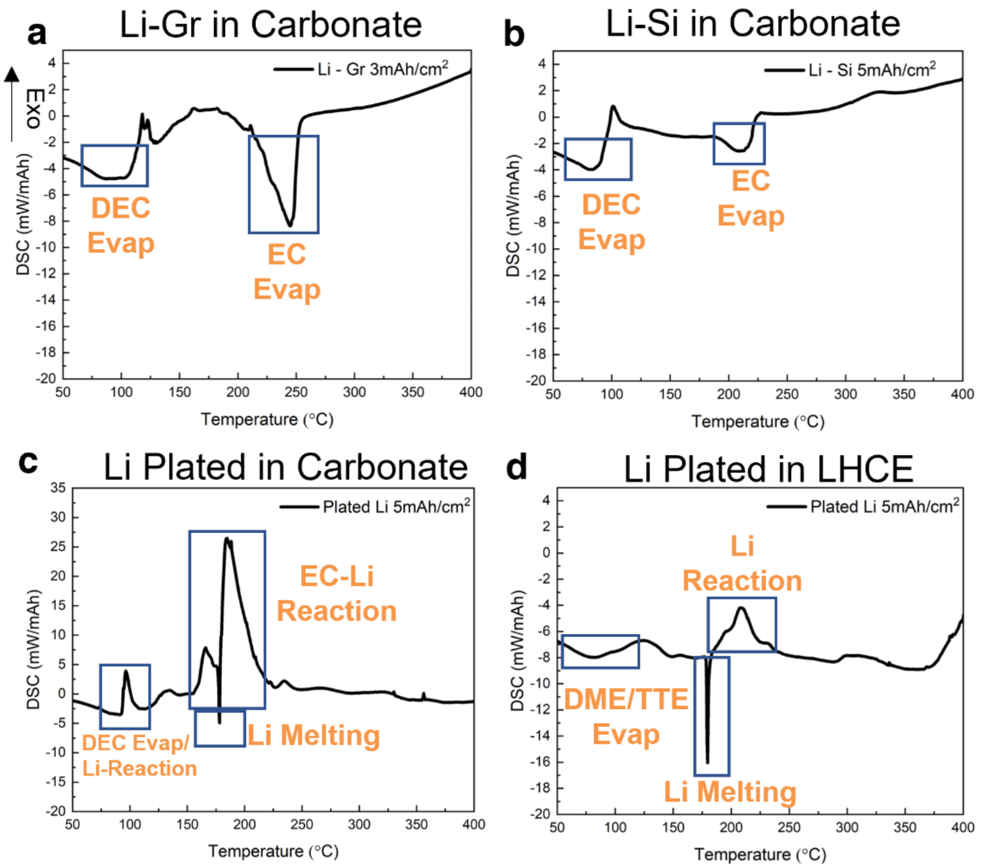

Figure 5.2 The DSC curves of the Li anodes after 1 cycle: (a) Li-Gr, (b) Li-Si, (c) Li metal plated in Carbonate and (d) Li metal plated in LHCE. Graphite and Si anodes are lithiated to the desired capacity in half cell setup with the rate of C/20. Li metal is plated in Li||Cu coin cell to the desired capacity at a current density of 0.5mA/cm^2.

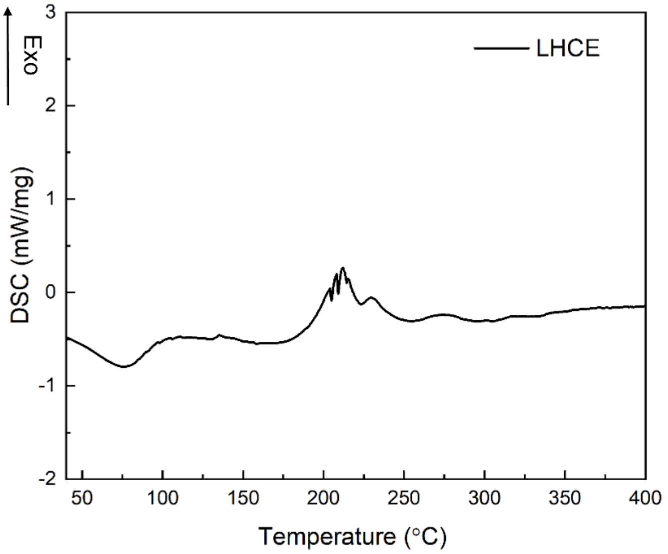

Figure 5.3 The DSC profile of LHCE by itself.

5.4 DSC of Li anodes after 10 cycles

The reactivity of the three types of anodes is also studied after 10 cycles. **Fig. 5.4a-c** shows the DSC curve and the morphology of the lithiated Graphite anode after 10 cycles. Similar to the 1st cycle charged Graphite samples, most of the DSC peaks are associated with the evaporation of the electrolyte solvents, with the exception of two exothermic peaks during the solvent evaporation. As shown in **Fig. 5.4b and c**, there seems to be some SEI accumulation on the Graphite surface as the layered surface morphology of graphite has disappeared after 10 cycles. The small heat releasing peaks (at around 100˚C and 230˚C) might be associated with the oxidation of the Li-Gr electrode during the solvent evaporation process. Similar trend is found in the 10-cycled Si anode (**Fig. 5.4d-f**), where two exothermic peaks (at around 100˚C and 230˚C) are also found during the same temperature range. The SEI accumulation is also obvious on the Si surface (**Fig. 5.4e-f**). The accumulation of SEI and trapped Li in the Gr and Si electrode after 10 cycles might contribute to the two small heat releasing peaks observed in the DSC. Overall, the reactivity of lithiated Si and Graphite is relatively low as no large exothermic peaks are observed during the heating process. **Fig. 5.4g** shows the DSC curve of the plated-Li in LHCE electrolyte after 10 plate-strip cycles. As the inserted images and SEM images are shown (**Fig. 5.4h-i**), because of the superior performance of the LHCE, the deposited Li is still shiny, and the Li particles are bulky after 10 cycles. In addition to that, most of the electrolyte solvents are evaporated before the Li melting point. As a result, the thermal response of the Li in LHCE is still relatively low, with only 39.8J/mAh of heat released during the heating process, which is in the same magnitude as the Li-Gr and Li-Si cases. However, for the plated-Li in Carbonate, there is a large amount of mossy Li accumulated on the electrode surface (**Fig. 5.4k-l and insert of 5.4j**). Because of the low cycling Coulombic efficiency

(CE) of the Carbonate, there is a significant amount of nano-size inactive Li accumulated on the electrode, which can be seen as the mossy Li (**Fig. 5.4l**)[74]. The accumulation of these nano-size inactive Li eventually caused an explosion of the DSC Pan during the heating process. Based on the results so far, it can be seen that both the electrolyte and the morphology of Li play significant roles in controlling the reactivity of Li.

5.5 In situ FTIR for gas analysis

In situ FTIR is used to decipher the gas evolution during the DSC of Li metal to study the effects of electrolyte on the plated-Li. **Fig. 5.5a** shows the FTIR spectra of the gas generated during the heating process of plated-Li with Carbonate. Before 130°C, most of the peaks are associated with the evaporation of DEC (boiling point: 127°C). The spectra have two main peaks located at 1268 cm^{-1} and 1771 cm^{-1}, representing O-C-O symmetric stretch and C=O stretch on the DEC molecules, respectively[133]. EC's evaporation occurs at higher temperatures because of the higher boiling point of 243°C. The peaks associated with EC are located at 1090 cm^{-1} and 1875 cm^{-1}, representing O-C-O asymmetric stretch and C=O stretch on the EC molecules respectively[133]. There is no other obvious peak detected during the in situ FTIR study for the plated-Li with Carbonate samples. The overlapping temperature ranges between Li melting and solvent boiling can be part of the reasons why the Li show large exothermic peak during the DSC measurement (**Fig. 5.2c**).

Contrary to the Carbonate, because of the low boiling point of TTE (93.2°C) and DME (85°C), the solvents in the LHCE electrolyte evaporated before 120°C (**Fig. 5.5b**). As a result, the oxidation of Li is caused mainly by the residue organic components and electrolyte salts, as shown by N=O and $C_xH_yF_z^+$ fragment peaks in the FTIR spectrum at 200°C. The DSC of the pristine LHCE also confirms this observation (**Fig. 5.3**). The results so far confirm that the electrolyte solvents are the main reasons for the thermal instability of Li metal cell. However, the future of electrolyte design not only should study the fire-retarding features of the solvents, but also needs to focus on the thermal stability of the electrolyte salts, as the decomposition products from the salt will also oxidize the melt Li and interact with the delithiated cathode, which can lead to the release of heat or even fire[54].

5.6 Effect of Li morphology on the Li reactivity

The effects of Li morphology on the Li reactivity are also studied. A split cell setup (**Fig. 5.6a**) is used to control the morphology of the plated Li by tuning the external stacking pressure[125]. As shown in **Fig. 5.6b-c**, even with the Carbonate electrolyte, which is known for producing Li whiskers, the plated Li can achieve nearly 100% dense morphology. With the improved morphology, the Li porosity is significantly reduced, as shown in **Fig. 5.6e**. The plated-Li shows a relatively slow oxidation process instead of a sudden heat release as in **Fig. 5.6d**. Based on the results, it can be concluded that both the electrolyte and Li morphology play crucial roles in controlling the Li reactivity. Most of the oxidation of Li takes place between Li and electrolyte. If the Li can be plated in a nearly 100% dense morphology, the contact surface area between Li and the electrolyte can be significantly reduced so that the oxidation of Li metal by the electrolyte can also be largely slowed down.

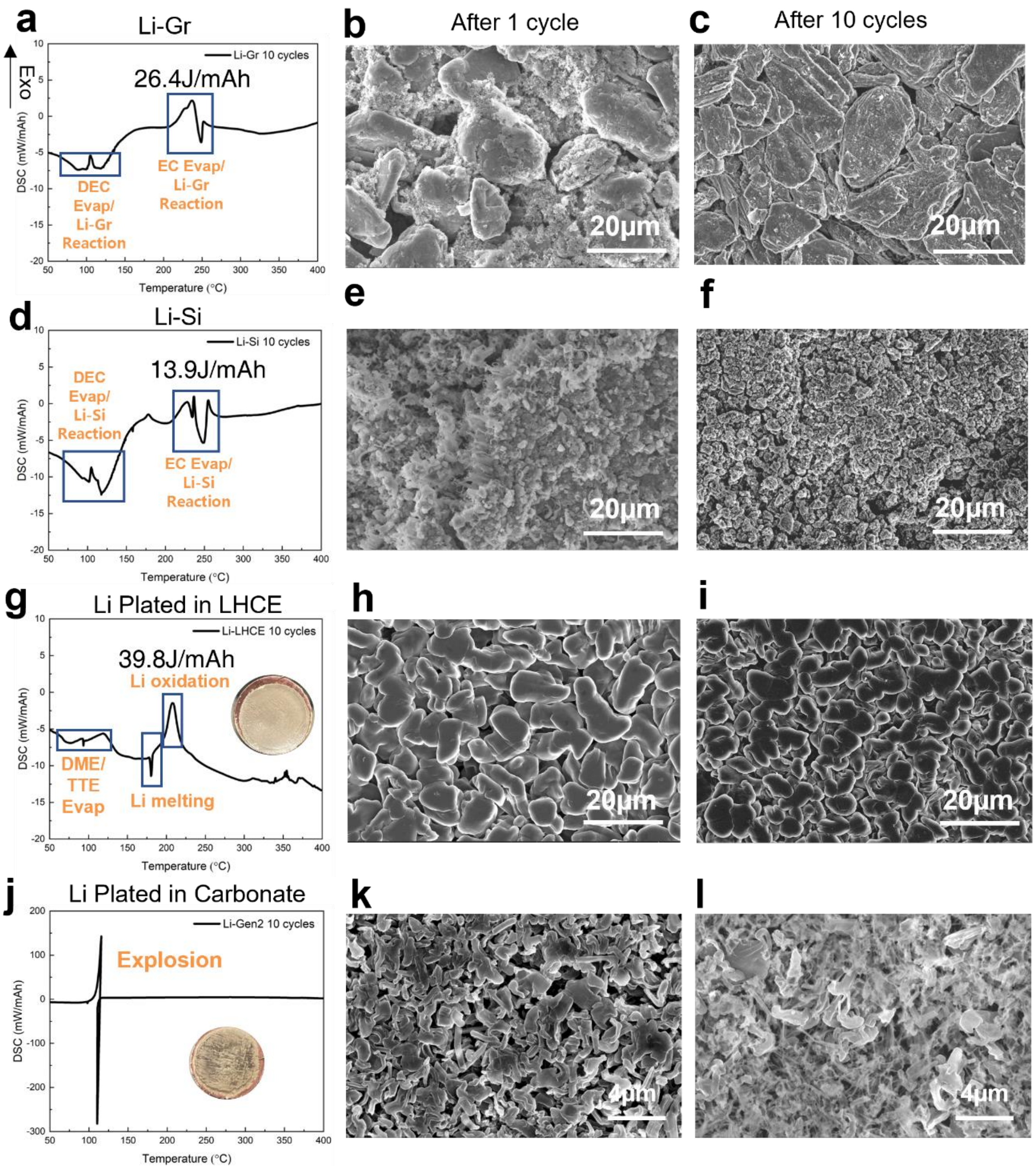

Figure 5.4 The DSC curves of the Li anodes after 10 cycles: (a) Li-Gr, (d) Li-Si, (g) Li plated in LHCE and (j) Li plated in Carbonate after 10 cycles. The SEM images of anode morphology after 1 cycle and after 10 cycles: (b-c) graphite, (e-f) Si, (h-i) Li plated in LHCE and (k-l) Li plated in Carbonated. Inserts: the digital images of Li plated on the Cu after 10 cycles. The amount of heat release from the oxidation peak of each DSC curve is labeled in the corresponding figures. Graphite and Si anodes are cycled in half cell configuration at rate of C/20 and Li metal anodes are cycled in Li||Cu cells at rate of 0.5mA/cm^2.

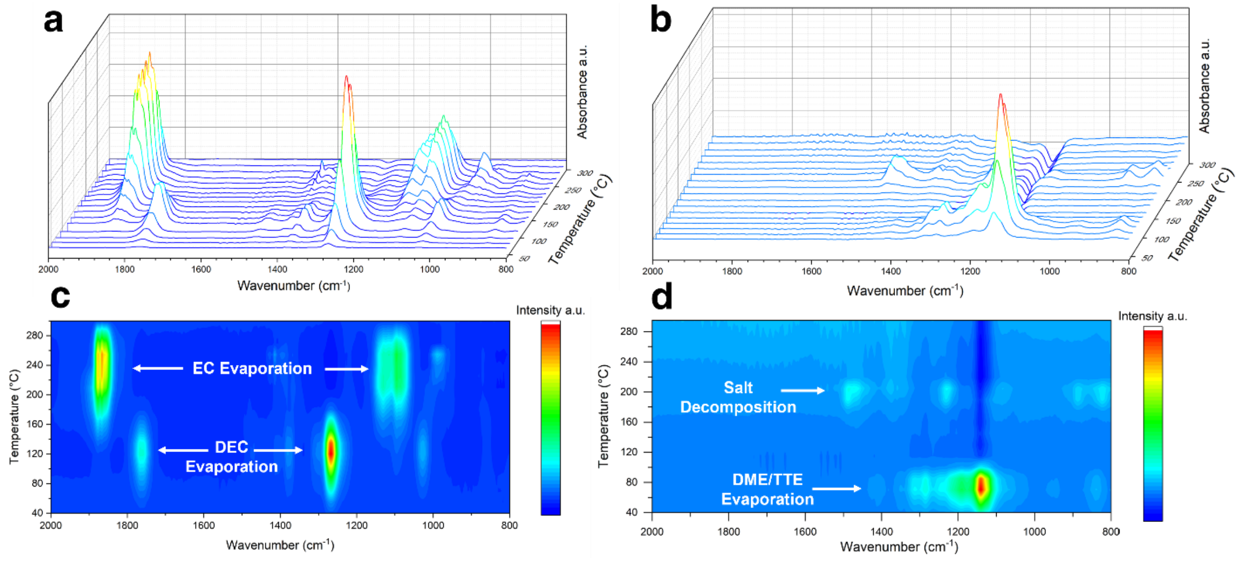

Figure 5.5 The in situ FTIR spectra of plated Li with electrolyte: (a) Carbonate and (b) LHCE at different temperatures. The 2D intensity mapping of the in situ FTIR spectra of (a) plated Li with Carbonate and (b) plated Li with LHCE at different temperatures

5.7 LMB full cell reactivity analysis

The reactivity of Li metal full cell is also analyzed. With the knowledge gained so far, we utilized split cell setup to cycle the Cu||NMC622 full cell with LHCE to achieve uniform Li morphology. After the charging cycle, the cell is dissembled at 4.4V, and all the cell components are sealed into a Al Pan for DSC measurement. **Fig. 5.7a** shows the DSC curve of delithiated NMC622 with electrolyte and separator. The delithiated NMC622 will decompose at around 220°C and 300°C to release O_2, which agrees with the literature results[134]. In addition to that, the decomposition of LiFSI salt is also observed at around 220°C, which overlaps with the decomposition of NMC622. When the delithiated NMC622 is coupled with plated Li, the released oxygen from the decomposed cathode and LiFSI salt will react with Li violently and cause a huge amount of heat release (**Fig. 5.7b**). Even if the Li morphology and the electrolyte are optimized, the O_2 released from the cathode is still detrimental to the full cell level safety. To further evaluate the impact of O_2 on the anode safety, DSC of Li-Gr, Li-Si and plated Li is done in air (**Fig. 5.8**).

It was found that even though there is limited heat release from Li-Gr at lower temperature range (lower than 400℃), the carbon material started to burn in air because of the presence of O_2. The plated Li shows limited heat release because oxidation of Li in air was rather a slow process. Therefore, no sudden release of heat was observed (**Fig. 5.8c**). To minimize the impact of cathode on the Li metal full cell safety, we adopted $LiFePO_4$ (LFP) as the cathode material because of its stability under high temperatures. Although there is still some oxidation of Li caused by the decomposition of electrolyte salts (**Fig. 5.3**), the reduced release of O_2 indeed helps to improve the overall safety of the Li||LFP full cell, which releases only half of the heat as the Li||NMC622 did (**Fig. 5.7d**). To further minimize the impact from salt decomposition and O_2 release from the cathode, $LiNi_{0.5}Mn_{1.5}O_4$ (LNMO) cathode with all fluorinated electrolyte (All-F electrolyte, 1M $LiFP_6$ in FEC: Methyl 2,2,2-Trifluoroethyl Carbonate (FEMC), 3:7 by weight) is adopted for this purpose. As shown in **Fig. 5.7e-f**, the ultra thermal stability of both the cathode and electrolyte lead to an extraordinarily stable Li metal full cell. There is no obvious release of heat from the DSC test of the Li||LNMO full cell after charging to 4.85 V. The effect of surface coating on the cathode is also investigated in this work. An thin layer (~2nm) of Al_2O_3 is coated onto the NMC622 cathode through Atomic Layer Deposition (ALD) method[135]. With the applied coating, we hope to stop the interactions between the electrolyte salt and the delithiated cathode to mitigate the decomposition of the cathode[54]. In **Fig. 5.9**, the thermal stability of the Li||coated NMC622 full cell is tested with LHCE. The DSC shows that even with the Al_2O_3 coating, the thermal stability of the full cell did not improve much. However, it is known so far that the LiFSI salt in the LHCE electrolyte will decompose at around 220˚C, which might contribute to this instability. Therefore, the more stable All-F electrolyte is used in the Li|| coated NMC622 full to study whether the thermal stability of the NMC622 is truly improved or not. As shown in **Fig. 5.7g-h**, no significant thermal stability improvement is observed in the Al_2O_3 coated-NMC622 sample compared to the uncoated one. The intrinsic instability of delithiated NMC622 will cause the release of O_2 and lead to a catastrophic heat generation when coupled with Li.

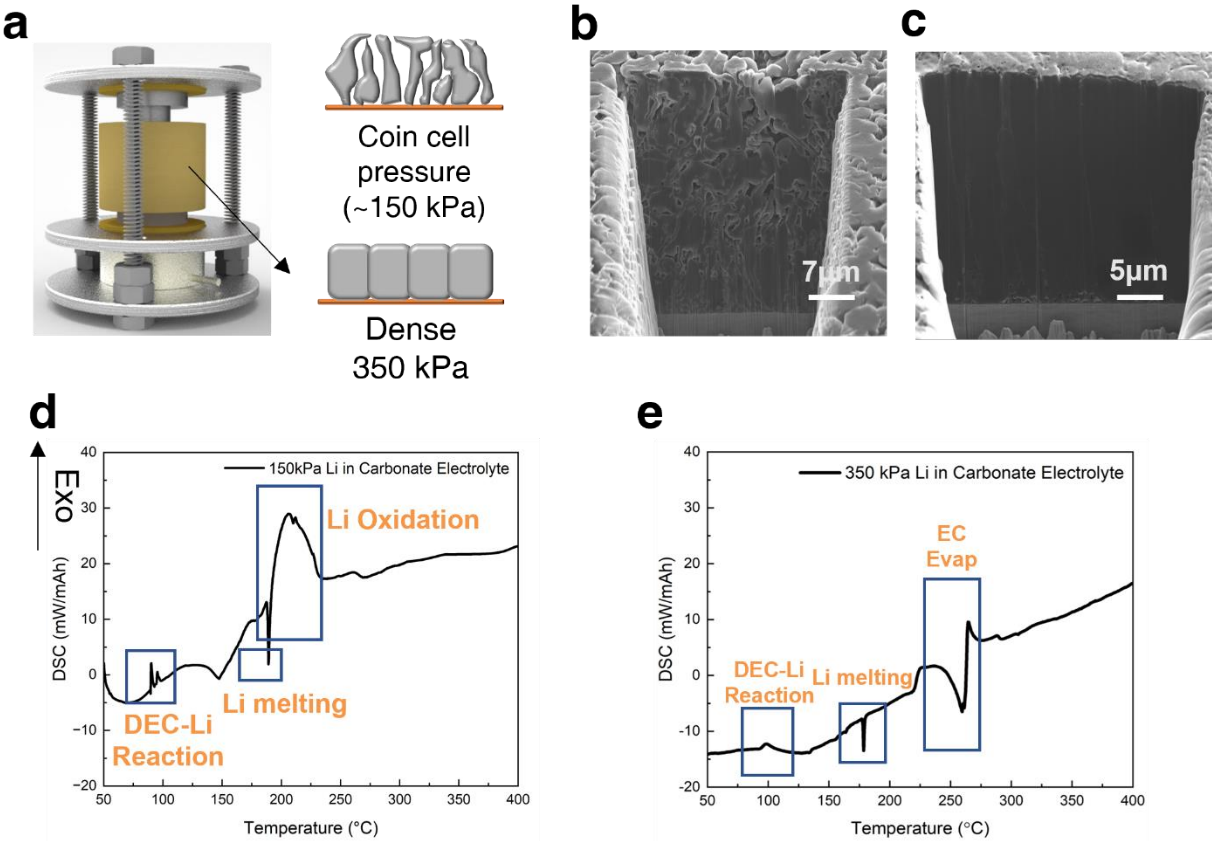

Figure 5.6 The effect of Li morphology on the Li reactivity: (a) The split cell setup for controlling the stack pressure on Li plating. The cross-sectional morphology of Li plated under (b) 150 kPa stack pressure (c) 350 kPa stack pressure. DSC curve of Li plated under (d) 150 kPa stack pressure and (e) 350 kPa stack pressure. All Li is plated to 5mAh/cm^2 at rate of 0.5mA/cm^2.

Figure 5.7 The DSC curves of Li metal full cells with different cathodes: (a) delithiated NMC622 with separator and LHCE, (b) plated Li with delithiated NMC622, separator and LHCE, (c) delithiated LFP with separator and LHCE, (d) plated Li with delithiated LFP, separator and LHCE, (e) delithiated LNMO with separator and All-F electrolyte, (f) plated Li, delithiated LNMO with separator and All-F electrolyte, (g) delithiated coated NMC622 with separator and All-F electrolyte and (h) plated Li, delithiated coated NMC622 with separator and All-F electrolyte. All cells are cycled at C/20 with corresponding electrolyte.

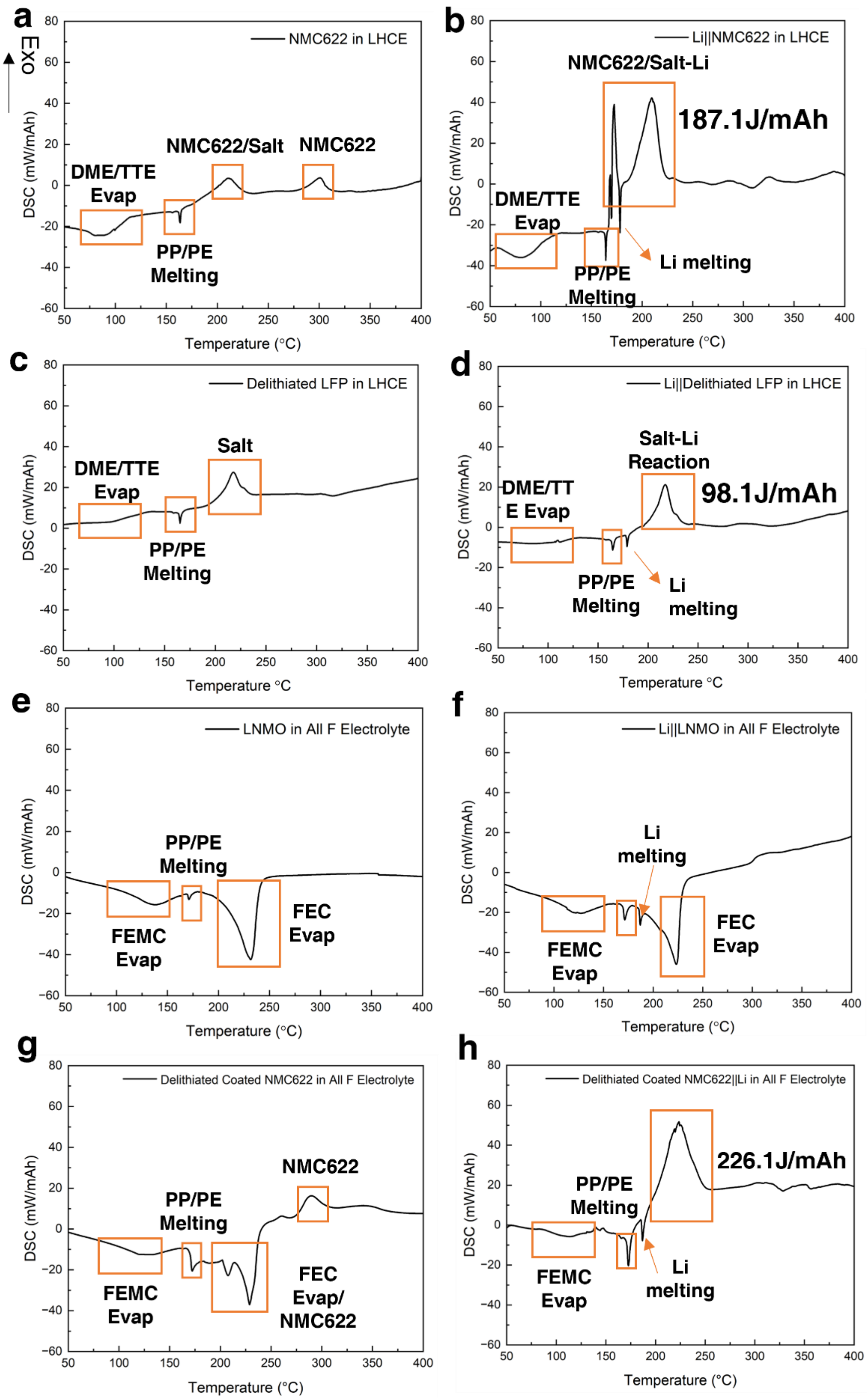
a
Exo
NMC622 in LHCE
DME/TTE Evap
PP/PE Melting
NMC622/Salt
NMC622
DSC (mW/mAh)
Temperature (°C)
b
Li||NMC622 in LHCE
NMC622/Salt-Li
187.1J/mAh
DME/TTE Evap
PP/PE Melting
Li melting
DSC (mW/mAh)
Temperature (°C)
c
Delithiated LFP in LHCE
Salt
DME/TTE Evap
PP/PE Melting
DSC (mW/mAh)
Temperature °C
d
Li||Delithiated LFP in LHCE
Salt-Li Reaction
98.1J/mAh
DME/TTE Evap
PP/PE Melting
Li melting
DSC (mW/mAh)
Temperature °C
e
LNMO in All F Electrolyte
PP/PE Melting
FEMC Evap
FEC Evap
DSC (mW/mAh)
Temperature (°C)
f
Li||LNMO in All F Electrolyte
Li melting
FEMC Evap
FEC Evap
DSC (mW/mAh)
Temperature (°C)
g
Delithiated Coated NMC622 in All F Electrolyte
NMC622
PP/PE Melting
FEMC Evap
FEC Evap/ NMC622
DSC (mW/mAh)
Temperature (°C)
h
Delithiated Coated NMC622||Li in All F Electrolyte
226.1J/mAh
PP/PE Melting
FEMC Evap
Li melting
DSC (mW/mAh)
Temperature (°C)
80
60
40
20
0
-20
-40
-60
50
100
150
200
250
300
350
400

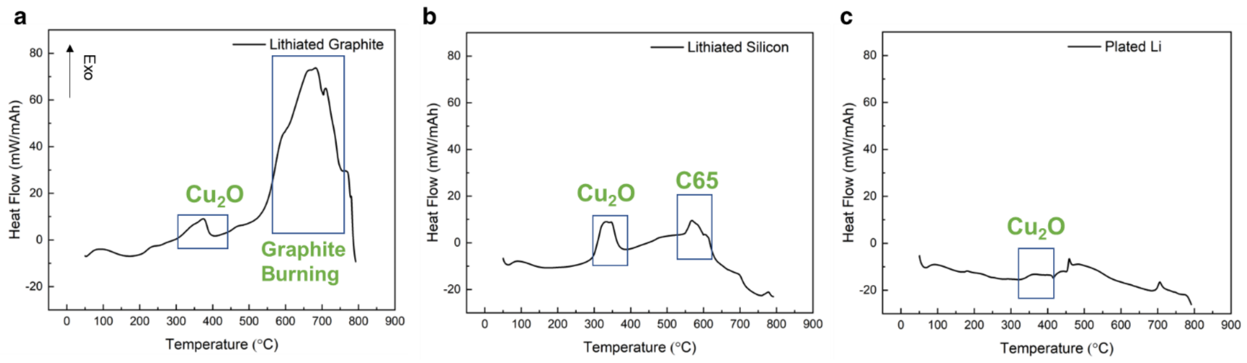

Figure 5.8 The DSC profiles of three lithiated anode in air: (a) Li-Gr (b) Li-Si and (c) plated-Li in Carbonate. All DSC is done in air. Graphite and Si anodes are cycled in half cell configuration at rate of C/20 and Li metal anodes are cycled in Li||Cu cells at rate of 0.5mA/cm^2. Carbonate electrolyte is used for all cells.

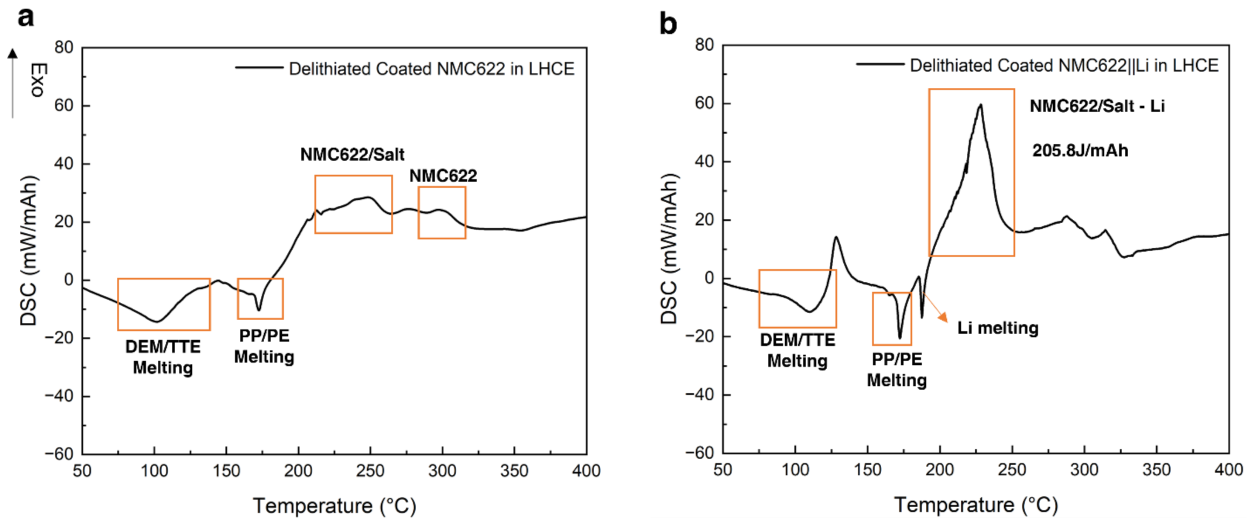

Figure 5.9 The DSC profiles of coated NMC622 cathodes: (a) delithiated coated NMC622 with separator and LHCE and (b) plated Li, delithiated coated NMC622 with separator and LHCE. All cells are cycled at C/20 with corresponding electrolyte.

5.8 Conclusion

In conclusion, the reactivity of Li-Gr, Li-Si, and plated Li are compared using integrated DSC and in situ FTIR techniques. It is found that the reactivity of plated Li in the cell is highly related to its morphology and the electrolyte composition. With dense morphology and novel electrolyte, the reactivity of plated Li in the cell can be drastically suppressed to the same level as that of Li-

Gr and Li-Si anodes. Therefore, it is crucial to plate Li in dense morphology to minimize its surface area and utilize thermal-stable electrolytes for safe operation of Li metal cells. Moreover, the crosstalk influence from the cathode thermal decomposition may cause a safety hazard when Li metal anode is used. By switching to more thermally stable cathode materials such as LFP and LNMO, the thermal stability of the Li metal full cell can be largely improved. In addition to that, the decomposition of the electrolyte salt also needs to be strictly controlled. Lastly, the cycle number and cell environment all contribute to the Li metal reactivity. It is important to control the accumulation of inactive Li and Li morphology even after extended cycles. The key parameters in controlling the reactivity of Li metal discovered in this work can be applied to the future research of Li metal anode for practical Li metal full cells.

Chapter 5, in full, is an unpublished material “Key Parameters in Determining the Reactivity of Lithium Metal Battery”, Bingyu Lu, Diyi Cheng, Bhagath Sreenarayanan, Weikang Li, Bhargav Bhamwala, Wurigumula Bao, Ying Shirley Meng. The dissertation author was the co-primary investigator and author of this paper.

Chapter 6 Conclusion and Future Perspectives

6.1 Conclusion – paving the way for the commercialization of LMB

As tremendous amount of efforts have been put on the prolonging the cycle life of LMB, it is also important to consider other crucial performance aspects, such as calendar life and safety properties, of the LMB before the commercialization of the LMB. In the previous chapters, it is shown that the chemical stability of the Li metal anode is the most significant parameter to consider when designing a LMB system. With a chemically stable Li metal anode, the assembled LMB demonstrated long calendar life as well as outstanding safety properties. The chemical stability of the Li metal anode depends on the several parameters: 1) morphology; 2) interphase and 3) compatibility between electrolyte and cathode.

To control the Li morphology in the liquid electrolyte, two different ways have been demonstrated in the Chapter 2 and 3. First is the utilization of porous copper current collectors. It is shown that by increasing the surface area of the current collector, the local current density on the current collector would decrease, which in turn can help Li to deposit at a slower rate and obtain a denser morphology. However, there is always an optimum range of the specific surface area for different types of current collectors, as too high of the surface area would also induce higher amount of SEI formation. The second method is to utilize external stack pressure to densify the Li metal during the plating/stripping process. Since Li metal is a relatively soft metal, with yield strength of ~500 kPa, it is possible to apply a moderate amount of stack pressure to help Li metal to be plated into a densely packed morphology. As shown in the Chapter 3, with the application of the pressure apparatus, the resulting plated Li has a nearly 100% dense morphology, and its reversibility is also demonstrated up to 30 cycles. The stack pressure can densify the Li deposits since its initial growth stages (nucleation). With these densified Li nucleus, the Li continues to grow in a densely packed manner and results in a ultra-dense Li metal. With the dense morphology, the deposited Li will only have a 2D contact surface area with the electrolyte, which can largely mitigate the side reaction between these two components.

The interphase between the Li metal and the liquid electrolyte is mainly consisted of the decomposition products of the electrolyte. Therefore, the stability of this interphase is largely controlled by the composition of the electrolyte. In Chapter 4, it is shown that by utilizing advanced electrolyte system such as LHCE, the resulting SEI is much more stable than the counterparts of the carbonate-based electrolytes. Through XPS depth profiling, it can be seen that the reasons for the major difference in the SEI formed in the carbonate-based electrolytes and the LHCE is the organic compounds. More work should be done to study the optimization of the organic components in the SEI layers.

The overall stability of LMB is dictated by the harmony between the anode, cathode and the electrolyte. As shown in chapter 5, even after optimizing each individual components in a LMB, if the interaction between these components can trigger a detrimental reaction, it will compromise the safety of the LMB. For example, the LiFSI salt used in the most advanced LHCE electrolyte can cause a thermal reaction with the LFP cathode, which is considered to be one of the most thermally stable cathodes. These synergetic effects can cause a catastrophic result on the overall safety performance of the LMB. Therefore, when designing a safe LMB, the compatibility of each battery components should be considered.

6.2 Large scale uniform Li metal plating with precise stack pressure control

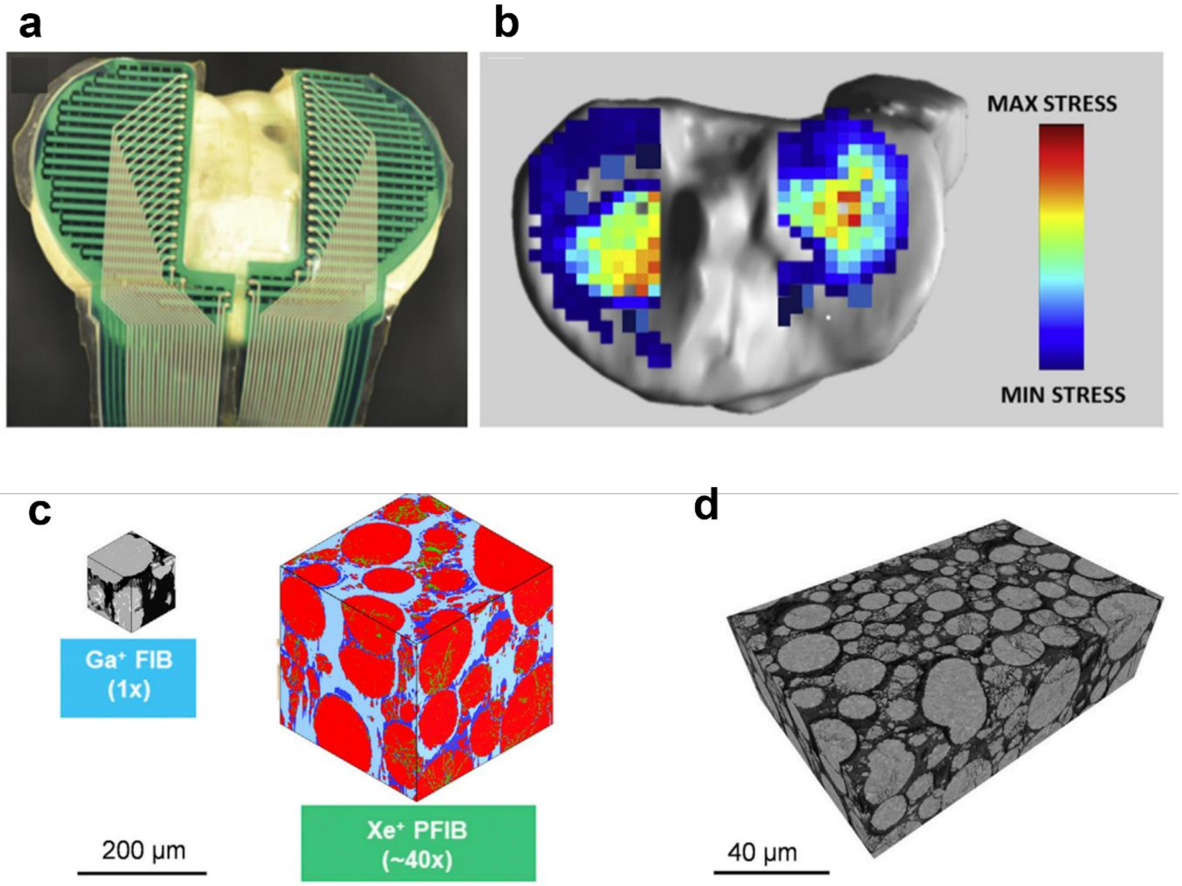

Figure 6.1 The example of using Tekscan pressure sensor for pressure mapping: a) Tekscan sensor across the tibial surface on human legs, b) stress map across the tibial surface[136]. An example of using PFIB for quantitative analysis of NMC811 thick electrode: c) the comparison between the 3D reconstruction done by Ga^+ FIB and PFIB. d) 3D reconstruction of pristine NMC811 thick PFIB[137].

As discussed in the previous section, the Li morphology is one of most crucial parameters in dictating the stability of LMB. In the previous Chapters, the effects of stack pressure on the Li plating/stripping process are studied in small cell formats (in mAh level). Although the information obtained from the work can help us to understand how pressure can densify the deposited Li, in the actual LMB (in Ah level) for commercial applications, a totally different pressure setup and monitoring system needs to be designed. Tekscan is a new type of thin and flexible pressure sensor that can provide a pressure mapping for a relatively large area (~10 cm^2). As shown in **Fig. 6.1a**

and b, the Tekscan sensor is implemented onto the tibial surface on human legs and the stress map is obtained across the tibial surface[136]. Similar pressure mapping setup can be easily adopted into the pouch cell fixtures and the applied stack pressure can be monitored in real time during the pouch cell cycling process. After cycling, a new quantitative characterization tool, Plasma Focused Ion Beam (PFIB), can be used to study the Li metal anode morphology. This new technique can help us to study the Li morphology variation in a large scale (~1000 μm^3 **Fig. 6.1c and d**)[137]. The effects of uniformity of the applied pressure on the Li metal pouch cell can be quantitatively analyzed by the combination of Tekscan sensor and PFIB.

6.3 Novel electrolyte salt and solvent design

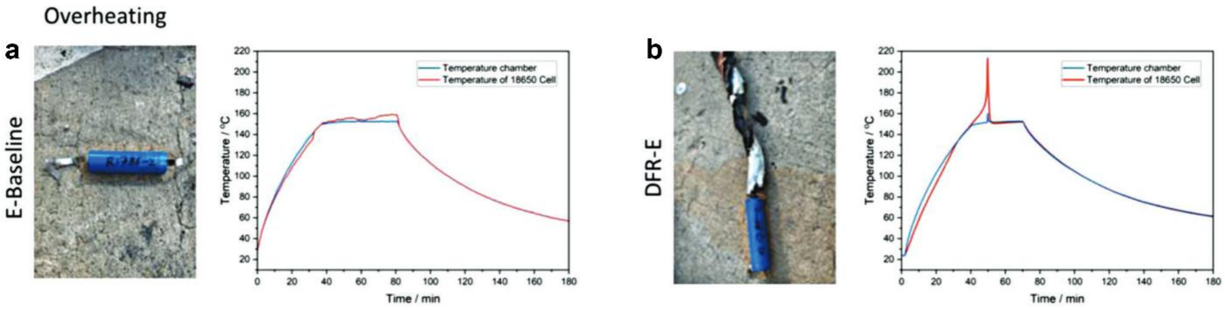

Figure 6.2 Photographs (after overheating) and temperature profiles (during heating) of Gr||LFP 18650 cells using a) E-baseline electrolyte and b) DFR-E electrolyte[54].

The results in Chapter 5 show that the interaction between the LiSFI salt and the charged cathode can cause catastrophic failure to the overall integrity of the LMB. This phenomenon is also observed in literature where the Gr||LFP 18650 cells with two types of electrolyte are tested under elevated temperatures[54]. It is found that the DFR-E, which is a new type of fire-retardant electrolyte, will cause a huge temperature spike during the heating test and lead to a detrimental damage to the cell (**Fig. 6.2b**). What is even more surprising is that the 18650 cell uses the traditional carbonate-based electrolyte actually survives the heating test without showing any temperature spikes (**Fig. 6.2a**). These results all point to one fact that the overall safety properties of a battery cell do not only rely on the fire-retardant electrolyte, but on the synergistic interaction between all components in the cell. Therefore, the future development of liquid electrolyte should focus not only on the fire-retardant property itself, but also its stability when coupled with plated Li and charged cathode. As shown in the results presented in the Chapter 5, although the LiSFI salt is considered as a popular candidate for high performance electrolyte for LMB, but its instability at elevated temperatures shows that it is not an ideal electrolyte salt for practical LMB. Future research should direct more efforts on the search and synthesis of thermally stable and high performing Li salts for LMB.

Reference

(1) Dunn, B.; Kamath, H.; Tarascon, J.-M. Electrical Energy Storage for the Grid: A Battery of Choices. *Science (80-.).* **2011**, *334* (6058), 928 LP – 935. https://doi.org/10.1126/science.1212741.

(2) Goodenough, J. B.; Park, K.-S. The Li-Ion Rechargeable Battery: A Perspective. *J. Am. Chem. Soc.* **2013**, *135* (4), 1167–1176. https://doi.org/10.1021/ja3091438.

(3) Xu, W.; Wang, J.; Ding, F.; Chen, X.; Nasybulin, E.; Zhang, Y.; Zhang, J.-G. Lithium Metal Anodes for Rechargeable Batteries. *Energy Environ. Sci.* **2014**, *7* (2), 513–537. https://doi.org/10.1039/C3EE40795K.

(4) Lin, D.; Liu, Y.; Cui, Y. Reviving the Lithium Metal Anode for High-Energy Batteries. *Nat. Nanotechnol.* **2017**, *12*, 194.

(5) Xiao, B. J. How Lithium Dendrites Form in Liquid Batteries. **2019**, *366* (6464), 426–428.

(6) Fang, C.; Wang, X.; Meng, Y. S. Key Issues Hindering a Practical Lithium-Metal Anode. *Trends Chem.* **2019**, *1* (2), 152–158. https://doi.org/10.1016/j.trechm.2019.02.015.

(7) Xu, K. Nonaqueous Liquid Electrolytes for Lithium-Based Rechargeable Batteries. *Chem. Rev.* **2004**, *104* (10), 4303–4418. https://doi.org/10.1021/cr030203g.

(8) Xiao, J. How Lithium Dendrites Form in Liquid Batteries. *Science (80-.).* **2019**, *366* (6464), 426–427. https://doi.org/10.1126/science.aay8672.

(9) Lu, D.; Shao, Y.; Lozano, T.; Bennett, W. D.; Graff, G. L.; Polzin, B.; Zhang, J.; Engelhard, M. H.; Saenz, N. T.; Henderson, W. A.; Bhattacharya, P.; Liu, J.; Xiao, J. Failure Mechanism for Fast-Charged Lithium Metal Batteries with Liquid Electrolytes. *Adv. Energy Mater.* **2015**, *5* (3), 1400993. https://doi.org/10.1002/aenm.201400993.

(10) Meng, Y. S.; Srinivasan, V.; Xu, K. Designing Better Electrolytes. *Science* **2022**, *378* (6624), eabq3750. https://doi.org/10.1126/science.abq3750.

(11) Ding, F.; Xu, W.; Graff, G. L.; Zhang, J.; Sushko, M. L.; Chen, X.; Shao, Y.; Engelhard, M. H.; Nie, Z.; Xiao, J.; Liu, X.; Sushko, P. V; Liu, J.; Zhang, J.-G. Dendrite-Free Lithium Deposition via Self-Healing Electrostatic Shield Mechanism. *J. Am. Chem. Soc.* **2013**, *135* (11), 4450–4456. https://doi.org/10.1021/ja312241y.

(12) Shiraishi, S. Surface Condition Changes in Lithium Metal Deposited in Nonaqueous Electrolyte Containing HF by Dissolution-Deposition Cycles. *J. Electrochem. Soc.* **1999**, *146* (5), 1633. https://doi.org/10.1149/1.1391818.

(13) Qian, J.; Henderson, W. A.; Xu, W.; Bhattacharya, P.; Engelhard, M.; Borodin, O.; Zhang, J.-G. High Rate and Stable Cycling of Lithium Metal Anode. *Nat. Commun.* **2015**, *6*, 6362.

(14) Suo, L.; Hu, Y.-S.; Li, H.; Armand, M.; Chen, L. A New Class of Solvent-in-Salt Electrolyte for High-Energy Rechargeable Metallic Lithium Batteries. *Nat. Commun.* **2013**, *4*, 1481.

(15) Yu, L.; Chen, S.; Lee, H.; Zhang, L.; Engelhard, M. H.; Li, Q.; Jiao, S.; Liu, J.; Xu, W.; Zhang, J. G. A Localized High-Concentration Electrolyte with Optimized Solvents and Lithium Difluoro(Oxalate)Borate Additive for Stable Lithium Metal Batteries. *ACS Energy Lett.* **2018**, *3* (9), 2059–2067. https://doi.org/10.1021/acsenergylett.8b00935.

(16) Chen, S.; Zheng, J.; Mei, D.; Han, K. S.; Engelhard, M. H.; Zhao, W.; Xu, W.; Liu, J.; Zhang, J. G. High-Voltage Lithium-Metal Batteries Enabled by Localized High-Concentration Electrolytes. *Adv. Mater.* **2018**, *30* (21), 1–7. https://doi.org/10.1002/adma.201706102.

(17) Chen, S.; Zheng, J.; Yu, L.; Ren, X.; Engelhard, M. H.; Niu, C.; Lee, H.; Xu, W.; Xiao, J.; Liu, J.; Zhang, J. G. High-Efficiency Lithium Metal Batteries with Fire-Retardant Electrolytes. *Joule* **2018**, *2* (8), 1548–1558. https://doi.org/10.1016/j.joule.2018.05.002.

(18) Ren, X.; Chen, S.; Lee, H.; Mei, D.; Engelhard, M. H.; Burton, S. D.; Zhao, W.; Zheng, J.; Li, Q.; Ding, M. S.; Schroeder, M.; Alvarado, J.; Xu, K.; Meng, Y. S.; Liu, J.; Zhang, J. G.; Xu, W. Localized High-Concentration Sulfone Electrolytes for High-Efficiency Lithium-Metal Batteries. *Chem* **2018**, *4* (8), 1877–1892. https://doi.org/10.1016/j.chempr.2018.05.002.

(19) Trinh, N. D.; Lepage, D.; Aymé-Perrot, D.; Badia, A.; Dollé, M.; Rochefort, D. An Artificial Lithium Protective Layer That Enables the Use of Acetonitrile-Based Electrolytes in Lithium Metal Batteries. *Angew. Chemie - Int. Ed.* **2018**, *57* (18), 5072–5075. https://doi.org/10.1002/anie.201801737.

(20) Li, N. W.; Yin, Y. X.; Yang, C. P.; Guo, Y. G. An Artificial Solid Electrolyte Interphase Layer for Stable Lithium Metal Anodes. *Adv. Mater.* **2016**, *28* (9), 1853–1858. https://doi.org/10.1002/adma.201504526.

(21) Hu, Z.; Zhang, S.; Dong, S.; Li, Q.; Cui, G.; Chen, L. Self-Stabilized Solid Electrolyte Interface on Host-Free Li Metal Anode towards High Areal Capacity and Rate Utilization. *Chem. Mater.* **2018**, *30*, 4039–4047. https://doi.org/10.1021/acs.chemmater.8b00722.

(22) Ma, L.; Kim, M. S.; Archer, L. A. Stable Artificial Solid Electrolyte Interphases for Lithium Batteries. *Chem. Mater.* **2017**, *29* (10), 4181–4189. https://doi.org/10.1021/acs.chemmater.6b03687.

(23) Liu, H.; Wang, X.; Zhou, H.; Lim, H.-D.; Xing, X.; Yan, Q.; Meng, Y. S.; Liu, P. Structure and Solution Dynamics of Lithium Methyl Carbonate as a Protective Layer For Lithium Metal. *ACS Appl. Energy Mater.* **2018**, *1* (5), 1864–1869. https://doi.org/10.1021/acsaem.8b00348.

(24) Kozen, A. C.; Lin, C. F.; Pearse, A. J.; Schroeder, M. A.; Han, X.; Hu, L.; Lee, S. B.; Rubloff, G. W.; Noked, M. Next-Generation Lithium Metal Anode Engineering via Atomic Layer Deposition. *ACS Nano* **2015**, *9* (6), 5884–5892. https://doi.org/10.1021/acsnano.5b02166.

(25) Kim, M. S.; Ryu, J. H.; Deepika; Lim, Y. R.; Nah, I. W.; Lee, K. R.; Archer, L. A.; Il Cho, W. Langmuir–Blodgett Artificial Solid-Electrolyte Interphases for Practical Lithium Metal Batteries. *Nat. Energy* **2018**, *3* (10), 889–898. https://doi.org/10.1038/s41560-018-0237-6.

(26) Zhai, P.; Liu, L.; Gu, X.; Wang, T.; Gong, Y. Interface Engineering for Lithium Metal Anodes in Liquid Electrolyte. *Adv. Energy Mater.* **2020**, *10* (34), 1–32. https://doi.org/10.1002/aenm.202001257.

(27) Sun, H.; Zhu, J.; Baumann, D.; Peng, L.; Xu, Y.; Shakir, I.; Huang, Y.; Duan, X. Hierarchical 3D Electrodes for Electrochemical Energy Storage. *Nat. Rev. Mater.* **2019**, *4* (1), 45–60. https://doi.org/10.1038/s41578-018-0069-9.

(28) Li, G.; Liu, Z.; Huang, Q.; Gao, Y.; Regula, M.; Wang, D.; Chen, L. Q.; Wang, D. Stable Metal Battery Anodes Enabled by Polyethylenimine Sponge Hosts by Way of Electrokinetic Effects. *Nat. Energy* **2018**. https://doi.org/10.1038/s41560-018-0276-z.

(29) Yun, Q.; He, Y. B.; Lv, W.; Zhao, Y.; Li, B.; Kang, F.; Yang, Q. H. Chemical Dealloying Derived 3D Porous Current Collector for Li Metal Anodes. *Adv. Mater.* **2016**, 6932–6939. https://doi.org/10.1002/adma.201601409.

(30) Lin, D.; Liu, Y.; Liang, Z.; Lee, H. W.; Sun, J.; Wang, H.; Yan, K.; Xie, J.; Cui, Y. Layered Reduced Graphene Oxide with Nanoscale Interlayer Gaps as a Stable Host for Lithium Metal Anodes. *Nat. Nanotechnol.* **2016**, *11* (7), 626–632. https://doi.org/10.1038/nnano.2016.32.

(31) Yan, K.; Lu, Z.; Lee, H. W.; Xiong, F.; Hsu, P. C.; Li, Y.; Zhao, J.; Chu, S.; Cui, Y. Selective Deposition and Stable Encapsulation of Lithium through Heterogeneous Seeded Growth. *Nat. Energy* **2016**, *1* (3). https://doi.org/10.1038/NENERGY.2016.10.

(32) Zheng, G.; Lee, S. W.; Liang, Z.; Lee, H.-W.; Yan, K.; Yao, H.; Wang, H.; Li, W.; Chu, S.; Cui, Y. Interconnected Hollow Carbon Nanospheres for Stable Lithium Metal Anodes. *Nat. Nanotechnol.* **2014**, *9*, 618.

(33) Kolesnikov, A.; Kolek, M.; Dohmann, J. F.; Horsthemke, F.; Börner, M.; Bieker, P.; Winter, M.; Stan, M. C. Galvanic Corrosion of Lithium-Powder-Based Electrodes. *Adv. Energy Mater.* **2020**, *10* (15), 1–9. https://doi.org/10.1002/aenm.202000017.

(34) Boyle, D. T.; Huang, W.; Wang, H.; Li, Y.; Chen, H.; Yu, Z.; Zhang, W.; Bao, Z.; Cui, Y. Corrosion of Lithium Metal Anodes during Calendar Ageing and Its Microscopic Origins. *Nat. Energy* **2021**, *6* (5), 487–494. https://doi.org/10.1038/s41560-021-00787-9.

(35) Khuwaja, K. DOE / EPRI 2013 Electricity Storage Handbook in Collaboration with NRECA DOE / EPRI 2013 Electricity Storage Handbook in Collaboration with NRECA. **2014**.

(36) Adams, B. D.; Zheng, J.; Ren, X.; Xu, W.; Zhang, J. G. Accurate Determination of Coulombic Efficiency for Lithium Metal Anodes and Lithium Metal Batteries. *Adv. Energy Mater.* **2018**, *8* (7), 1–11. https://doi.org/10.1002/aenm.201702097.

(37) Ospina-Acevedo, F.; Guo, N.; Balbuena, P. B. Lithium Oxidation and Electrolyte Decomposition at Li-Metal/Liquid Electrolyte Interfaces. *J. Mater. Chem. A* **2020**, *8* (33), 17036–17055. https://doi.org/10.1039/d0ta05132b.

(38) NORIO SATO Corrosion Research Group, Faculty of Engineering, Hokkaido University Kita-13, Nishi-8, Kita-Ku, Sapporo 060, Japan. **1996**, *41* (9), 1525–1532.

(39) Lin, D.; Liu, Y.; Li, Y.; Li, Y.; Pei, A.; Xie, J.; Huang, W.; Cui, Y. Fast Galvanic Lithium Corrosion Involving a Kirkendall-Type Mechanism. *Nat. Chem.* **2019**, *11* (4), 382–389. https://doi.org/10.1038/s41557-018-0203-8.

(40) Lafage, M.; Windel, D.; Russier, V.; Badiali, J. P. Mechanisms of Growth and Corrosion at the Lithium-Solvent Interface. *Electrochim. Acta* **1997**, *42* (19), 2841–2852. https://doi.org/10.1016/S0013-4686(97)00105-9.

(41) Iglesias, E.; Camacho, O.; Sanjuan, M.; Smith, C.; Calderón, S. M.; Rosales, A. A Parametric Dynamic Matrix Controller Approach for Nonlinear Chemical Processes. *WSEAS Trans. Syst. Control* **2016**, *11*, 397–408. https://doi.org/10.1002/advs.201500213.

(42) Nagasubramanian, G.; Fenton, K. Reducing Li-Ion Safety Hazards through Use of Non-Flammable Solvents and Recent Work at Sandia National Laboratories. *Electrochim. Acta* **2013**, *101*, 3–10. https://doi.org/10.1016/j.electacta.2012.09.065.

(43) Choi, N. S.; Profatilova, I. A.; Kim, S. S.; Song, E. H. Thermal Reactions of Lithiated Graphite Anode in LiPF6-Based Electrolyte. *Thermochim. Acta* **2008**, *480* (1–2), 10–14. https://doi.org/10.1016/j.tca.2008.09.017.

(44) Kriston, A.; Pfrang, A.; Döring, H.; Fritsch, B.; Ruiz, V.; Adanouj, I.; Kosmidou, T.; Ungeheuer, J.; Boon-Brett, L. External Short Circuit Performance of Graphite-LiNi1/3Co1/3Mn1/3O2 and Graphite-LiNi0.8Co0.15Al0.05O2 Cells at Different External Resistances. *J. Power Sources* **2017**, *361*, 170–181. https://doi.org/10.1016/j.jpowsour.2017.06.056.

(45) Jiang, J.; Dahn, J. R. Effects of Solvents and Salts on the Thermal Stability of LiC6. *Electrochim. Acta* **2004**, *49* (26), 4599–4604. https://doi.org/10.1016/j.electacta.2004.05.014.

(46) Golubkov, A. W.; Fuchs, D.; Wagner, J.; Wiltsche, H.; Stangl, C.; Fauler, G.; Voitic, G.; Thaler, A.; Hacker, V. Thermal-Runaway Experiments on Consumer Li-Ion Batteries with Metal-Oxide and Olivin-Type Cathodes. *RSC Adv.* **2014**, *4* (7), 3633–3642. https://doi.org/10.1039/c3ra45748f.

(47) Andersson, A. M.; Edström, K.; Thomas, J. O. Characterisation of the Ambient and Elevated Temperature Performance of a Graphite Electrode. *J. Power Sources* **1999**, *81–82*, 8–12. https://doi.org/10.1016/S0378-7753(99)00185-8.

(48) Galushkin, N. E.; Yazvinskaya, N. N.; Galushkin, D. N. Mechanism of Gases Generation during Lithium-Ion Batteries Cycling. *J. Electrochem. Soc.* **2019**, *166* (6), A897–A908. https://doi.org/10.1149/2.0041906jes.

(49) Wu, L.; Song, Z.; Liu, L.; Guo, X.; Kong, L.; Zhan, H.; Zhou, Y.; Li, Z. A New Phosphate-Based Nonflammable Electrolyte Solvent for Li-Ion Batteries. *J. Power Sources* **2009**, *188* (2), 570–573. https://doi.org/10.1016/j.jpowsour.2008.12.070.

(50) Zeng, Z.; Wu, B.; Xiao, L.; Jiang, X.; Chen, Y.; Ai, X.; Yang, H.; Cao, Y. Safer Lithium Ion Batteries Based on Nonflammable Electrolyte. *J. Power Sources* **2015**, *279*, 6–12. https://doi.org/10.1016/j.jpowsour.2014.12.150.

(51) Yin, Y.; Yang, Y.; Cheng, D.; Mayer, M.; Holoubek, J.; Li, W.; Raghavendran, G.; Liu,

A.; Lu, B.; Davies, D. M.; Chen, Z.; Borodin, O.; Meng, Y. S. Fire-Extinguishing, Recyclable Liquefied Gas Electrolytes for Temperature-Resilient Lithium-Metal Batteries. https://doi.org/10.1038/s41560-022-01051-4.

(52) Cao, X.; Xu, Y.; Zhang, L.; Engelhard, M. H.; Zhong, L.; Ren, X.; Jia, H.; Liu, B.; Niu, C.; Matthews, B. E.; Wu, H.; Arey, B. W.; Wang, C.; Zhang, J. G.; Xu, W. Nonflammable Electrolytes for Lithium Ion Batteries Enabled by Ultraconformal Passivation Interphases. *ACS Energy Lett.* **2019**, *4* (10), 2529–2534. https://doi.org/10.1021/acsenergylett.9b01926.

(53) Fan, X.; Ji, X.; Chen, L.; Chen, J.; Deng, T.; Han, F.; Yue, J.; Piao, N.; Wang, R.; Zhou, X.; Xiao, X.; Chen, L.; Wang, C. All-Temperature Batteries Enabled by Fluorinated Electrolytes with Non-Polar Solvents. *Nat. Energy* **2019**, *4* (10), 882–890. https://doi.org/10.1038/s41560-019-0474-3.

(54) Jia, H.; Yang, Z.; Xu, Y.; Gao, P.; Zhong, L.; Kautz, D. J.; Wu, D.; Fliegler, B.; Engelhard, M. H.; Matthews, B. E.; Broekhuis, B.; Cao, X.; Fan, J.; Wang, C.; Lin, F.; Xu, W. Is Nonflammability of Electrolyte Overrated in the Overall Safety Performance of Lithium Ion Batteries? A Sobering Revelation from a Completely Nonflammable Electrolyte. *Adv. Energy Mater.* **2022**, *2203144*. https://doi.org/10.1002/aenm.202203144.

(55) Laing, M. Melting Point, Density, and Reactivity of Metals. *J. Chem. Educ.* **2001**, *78* (8), 1054. https://doi.org/10.1021/ed078p1054.

(56) Louli, A. J.; Eldesoky, A.; Weber, R.; Genovese, M.; Coon, M.; deGooyer, J.; Deng, Z.; White, R. T.; Lee, J.; Rodgers, T.; Petibon, R.; Hy, S.; Cheng, S. J. H.; Dahn, J. R. Diagnosing and Correcting Anode-Free Cell Failure via Electrolyte and Morphological Analysis. *Nat. Energy* **2020**, *5* (9), 693–702. https://doi.org/10.1038/s41560-020-0668-8.

(57) Alvarado, J.; Schroeder, M. A.; Pollard, T. P.; Wang, X.; Lee, J. Z.; Zhang, M.; Wynn, T.; Ding, M.; Borodin, O.; Meng, Y. S.; Xu, K. Bisalt Ether Electrolytes: A Pathway towards Lithium Metal Batteries with Ni-Rich Cathodes. *Energy Environ. Sci.* **2019**, *12* (2), 780–794. https://doi.org/10.1039/c8ee02601g.

(58) Jin, S.; Jiang, Y.; Ji, H.; Yu, Y. Advanced 3D Current Collectors for Lithium-Based Batteries. *Adv. Mater.* **2018**, *1802014*, 1–13. https://doi.org/10.1002/adma.201802014.

(59) Liu, J.; Bao, Z.; Cui, Y.; Dufek, E. J.; Goodenough, J. B.; Khalifah, P.; Li, Q.; Liaw, B. Y.; Liu, P.; Manthiram, A.; Meng, Y. S.; Subramanian, V. R.; Toney, M. F.; Viswanathan, V. V.; Whittingham, M. S.; Xiao, J.; Xu, W.; Yang, J.; Yang, X. Q.; Zhang, J. G. Pathways for Practical High-Energy Long-Cycling Lithium Metal Batteries. *Nat. Energy* **2019**, *4* (3), 180–186. https://doi.org/10.1038/s41560-019-0338-x.

(60) Pei, A.; Zheng, G.; Shi, F.; Li, Y.; Cui, Y. Nanoscale Nucleation and Growth of Electrodeposited Lithium Metal. *Nano Lett.* **2017**, *17* (2), 1132–1139. https://doi.org/10.1021/acs.nanolett.6b04755.

(61) Shen, L.; Shi, P.; Hao, X.; Zhao, Q.; Ma, J.; He, Y. B.; Kang, F. Progress on Lithium Dendrite Suppression Strategies from the Interior to Exterior by Hierarchical Structure Designs. *Small* **2020**, *16* (26), 1–40. https://doi.org/10.1002/smll.202000699.

(62) Niu, C.; Pan, H.; Xu, W.; Xiao, J.; Zhang, J. G.; Luo, L.; Wang, C.; Mei, D.; Meng, J.; Wang, X.; Liu, Z.; Mai, L.; Liu, J. Self-Smoothing Anode for Achieving High-Energy Lithium Metal Batteries under Realistic Conditions. *Nat. Nanotechnol.* **2019**, *1*. https://doi.org/10.1038/s41565-019-0427-9.

(63) Zhang, R.; Cheng, X. B.; Zhao, C. Z.; Peng, H. J.; Shi, J. Le; Huang, J. Q.; Wang, J.; Wei, F.; Zhang, Q. Conductive Nanostructured Scaffolds Render Low Local Current Density to Inhibit Lithium Dendrite Growth. *Adv. Mater.* **2016**, *28* (11), 2155–2162. https://doi.org/10.1002/adma.201504117.

(64) Liu, Y.; Qin, X.; Zhang, S.; Huang, Y.; Kang, F.; Chen, G.; Li, B. Oxygen and Nitrogen Co-Doped Porous Carbon Granules Enabling Dendrite-Free Lithium Metal Anode. *Energy Storage Mater.* **2019**, *18* (August 2018), 320–327. https://doi.org/10.1016/j.ensm.2018.08.018.

(65) Zhang, R.; Wen, S.; Wang, N.; Qin, K.; Liu, E.; Shi, C. N-Doped Graphene Modified 3D Porous Cu Current Collector toward Microscale Homogeneous Li Deposition for Li Metal Anodes. **2018**, *1800914*, 1–9. https://doi.org/10.1002/aenm.201800914.

(66) Zhao, H.; Lei, D.; He, Y. B.; Yuan, Y.; Yun, Q.; Ni, B.; Lv, W.; Li, B.; Yang, Q. H.; Kang, F.; Lu, J. Compact 3D Copper with Uniform Porous Structure Derived by Electrochemical Dealloying as Dendrite-Free Lithium Metal Anode Current Collector. *Adv. Energy Mater.* **2018**, *8* (19), 1–8. https://doi.org/10.1002/aenm.201800266.

(67) Wang, Y.; Wang, Z.; Lei, D.; Lv, W.; Zhao, Q.; Ni, B.; Liu, Y.; Li, B.; Kang, F.; He, Y. B. Spherical Li Deposited inside 3D Cu Skeleton as Anode with Ultrastable Performance. *ACS Appl. Mater. Interfaces* **2018**, *10* (24), 20244–20249. https://doi.org/10.1021/acsami.8b04881.

(68) Yue, Y.; Liang, H. 3D Current Collectors for Lithium-Ion Batteries: A Topical Review. *Small Methods* **2018**, *1800056*, 1800056. https://doi.org/10.1002/smtd.201800056.

(69) Chen, K. H.; Sanchez, A. J.; Kazyak, E.; Davis, A. L.; Dasgupta, N. P. Synergistic Effect of 3D Current Collectors and ALD Surface Modification for High Coulombic Efficiency Lithium Metal Anodes. *Adv. Energy Mater.* **2019**, *9* (4), 1–12. https://doi.org/10.1002/aenm.201802534.

(70) Frisco, S.; Liu, D. X.; Kumar, A.; Whitacre, J. F.; Love, C. T.; Swider-lyons, K. E.; Litster, S. Internal Morphologies of Cycled Li-Metal Electrodes Investigated by Nano-Scale Resolution X - Ray Computed Tomography. **2017**, *18757* (1). https://doi.org/10.1021/acsami.7b03003.

(71) Ebner, M.; Wood, V.; Soc, J. E.; Ebner, M.; Wood, V. Tool for Tortuosity Estimation in Lithium Ion Battery Porous Electrodes F OCUS I SSUE OF S ELECTED P RESENTATIONS FROM IMLB 2014 Tool for Tortuosity Estimation in Lithium Ion Battery Porous Electrodes. **2015**. https://doi.org/10.1149/2.0111502jes.

(72) Liu, H.; Wang, E.; Zhang, Q.; Ren, Y.; Guo, X.; Wang, L.; Li, G. Unique 3D Nanoporous / Macroporous Structure Cu Current Collector for Dendrite-Free Lithium Deposition. *Energy Storage Mater.* **2018**, No. July, 0–1. https://doi.org/10.1016/j.ensm.2018.07.010.

(73) Matsuda, S.; Kubo, Y.; Uosaki, K.; Nakanishi, S. Lithium-Metal Deposition/Dissolution within Internal Space of CNT 3D Matrix Results in Prolonged Cycle of Lithium-Metal Negative Electrode. *Carbon N. Y.* **2017**, *119*, 119–123. https://doi.org/10.1016/j.carbon.2017.04.032.

(74) Fang, C.; Li, J.; Zhang, M.; Zhang, Y.; Yang, F.; Lee, J. Z.; Lee, M.; Alvarado, J.; Schroeder, M. A.; Yang, Y.; Lu, B.; Williams, N.; Ceja, M.; Yang, L.; Cai, M.; Gu, J.; Xu, K.; Wang, X.; Meng, Y. S. Batteries. *Nature*. https://doi.org/10.1038/s41586-019-1481-z.

(75) Cooper, S. J.; Bertei, A.; Shearing, P. R.; Kilner, J. A.; Brandon, N. P. TauFactor: An Open-Source Application for Calculating Tortuosity Factors from Tomographic Data. *SoftwareX* **2016**, *5*, 203–210. https://doi.org/10.1016/j.softx.2016.09.002.

(76) Cheng, X. B.; Zhang, R.; Zhao, C. Z.; Zhang, Q. Toward Safe Lithium Metal Anode in Rechargeable Batteries: A Review. *Chem. Rev.* **2017**, *117* (15), 10403–10473. https://doi.org/10.1021/acs.chemrev.7b00115.

(77) Winter, M.; Barnett, B.; Xu, K. Before Li Ion Batteries. *Chemical Reviews*. 2018, pp 11433–11456. https://doi.org/10.1021/acs.chemrev.8b00422.

(78) Fang, C.; Li, J.; Zhang, M.; Zhang, Y.; Yang, F.; Lee, J. Z.; Lee, M.-H.; Alvarado, J.; Schroeder, M. A.; Yang, Y.; Lu, B.; Williams, N.; Ceja, M.; Yang, L.; Cai, M.; Gu, J.; Xu, K.; Wang, X.; Meng, Y. S. Quantifying Inactive Lithium in Lithium Metal Batteries. *Nature* **2019**, *572* (7770), 511–515. https://doi.org/10.1038/s41586-019-1481-z.

(79) Xu, W.; Wang, J.; Ding, F.; Chen, X.; Nasybulin, E.; Zhang, Y.; Zhang, J. G. Lithium Metal Anodes for Rechargeable Batteries. *Energy and Environmental Science*. 2014, pp 513–537. https://doi.org/10.1039/c3ee40795k.

(80) Chazalviel, J. N. Electrochemical Aspects of the Generation of Ramified Metallic Electrodeposits. *Phys. Rev. A* **1990**, *42* (12), 7355–7367. https://doi.org/10.1103/PhysRevA.42.7355.

(81) Cao, X.; Ren, X.; Zou, L.; Engelhard, M. H.; Huang, W.; Wang, H.; Matthews, B. E.; Lee, H.; Niu, C.; Arey, B. W.; Cui, Y.; Wang, C.; Xiao, J.; Liu, J.; Xu, W.; Zhang, J. G. Monolithic Solid–Electrolyte Interphases Formed in Fluorinated Orthoformate-Based Electrolytes Minimize Li Depletion and Pulverization. *Nat. Energy* **2019**, *4* (9), 796–805. https://doi.org/10.1038/s41560-019-0464-5.

(82) Yang, Y.; Davies, D. M.; Yin, Y.; Borodin, O.; Lee, J. Z.; Fang, C.; Olguin, M.; Zhang, Y.; Sablina, E. S.; Wang, X.; Rustomji, C. S.; Meng, Y. S. High-Efficiency Lithium-Metal Anode Enabled by Liquefied Gas Electrolytes. *Joule* **2019**, *3* (8), 1986–2000. https://doi.org/10.1016/j.joule.2019.06.008.

(83) Chen, S.; Zheng, J.; Mei, D.; Han, K. S.; Engelhard, M. H.; Zhao, W.; Xu, W.; Liu, J.; Zhang, J. G. High-Voltage Lithium-Metal Batteries Enabled by Localized High-Concentration Electrolytes. *Adv. Mater.* **2018**, *1706102*, 1–7. https://doi.org/10.1002/adma.201706102.

(84) Niu, C.; Pan, H.; Xu, W.; Xiao, J.; Zhang, J.-G.; Luo, L.; Wang, C.; Mei, D.; Meng, J.; Wang, X.; Liu, Z.; Mai, L.; Liu, J. Self-Smoothing Anode for Achieving High-Energy

Lithium Metal Batteries under Realistic Conditions. *Nat. Nanotechnol.* **2019**, *14* (6), 594–601. https://doi.org/10.1038/s41565-019-0427-9.

(85) Cao, D.; Xing, Y.; Tantratian, K.; Wang, X.; Ma, Y.; Mukhopadhyay, A.; Cheng, Z.; Zhang, Q.; Jiao, Y.; Chen, L.; Zhu, H. 3D Printed High-Performance Lithium Metal Microbatteries Enabled by Nanocellulose. *Adv. Mater.* **2019**, *31* (14), 68–71. https://doi.org/10.1002/adma.201807313.

(86) Xu, R.; Cheng, X.-B.; Yan, C.; Zhang, X.-Q.; Xiao, Y.; Zhao, C.-Z.; Huang, J.-Q.; Zhang, Q. Artificial Interphases for Highly Stable Lithium Metal Anode. *Matter* **2019**, *1* (2), 317–344. https://doi.org/10.1016/j.matt.2019.05.016.

(87) Wang, J.; Huang, W.; Pei, A.; Li, Y.; Shi, F.; Yu, X.; Cui, Y. Improving Cyclability of Li Metal Batteries at Elevated Temperatures and Its Origin Revealed by Cryo-Electron Microscopy. *Nat. Energy* **2019**. https://doi.org/10.1038/s41560-019-0413-3.

(88) Liu, J.; Bao, Z.; Cui, Y.; Dufek, E. J.; Goodenough, J. B.; Khalifah, P.; Li, Q.; Yann Liaw, B.; Liu, P.; Manthiram, A.; Shirley Meng, Y.; Subramanian, V. R.; Toney, M. F.; Viswanathan, V. V; Stanley Whittingham, M.; Xiao, J.; Xu, W.; Yang, J.; Yang, X.-Q.; Zhang, J.-G. Pathways for Practical High-Energy Long-Cycling Lithium Metal Batteries. *Nat. Energy* **2019**, *4*, 180–186. https://doi.org/10.1038/s41560-019-0338-x.

(89) Hirai, T. Influence of Electrolyte on Lithium Cycling Efficiency with Pressurized Electrode Stack. *J. Electrochem. Soc.* **1994**, *141* (3), 611. https://doi.org/10.1149/1.2054778.

(90) Brandt, K.; Stiles, J. A. R. Battery and Methods of Making the Battery. 1190279, 1985.

(91) Wilkinson, D. P.; Blom, H.; Brandt, K.; Wainwright, D. Effects of Physical Constraints on Li Cyclability. *J. Power Sources* **1991**, *36* (4), 517–527. https://doi.org/10.1016/0378-7753(91)80077-B.

(92) Weber, R.; Genovese, M.; Louli, A. J.; Hames, S.; Martin, C.; Hill, I. G.; Dahn, J. R. Long Cycle Life and Dendrite-Free Lithium Morphology in Anode-Free Lithium Pouch Cells Enabled by a Dual-Salt Liquid Electrolyte. *Nat. Energy* **2019**. https://doi.org/10.1038/s41560-019-0428-9.

(93) Yin, X.; Tang, W.; Jung, I. D.; Phua, K. C.; Adams, S.; Lee, S. W.; Zheng, G. W. Insights into Morphological Evolution and Cycling Behaviour of Lithium Metal Anode under Mechanical Pressure. *Nano Energy* **2018**, *50* (April), 659–664. https://doi.org/10.1016/j.nanoen.2018.06.003.

(94) Louli, A. J.; Genovese, M.; Weber, R.; Hames, S. G.; Logan, E. R.; Dahn, J. R. Exploring the Impact of Mechanical Pressure on the Performance of Anode-Free Lithium Metal Cells. **2019**, *166* (8), 1291–1299. https://doi.org/10.1149/2.0091908jes.

(95) Zhang, X.; Wang, Q. J.; Harrison, K. L.; Jungjohann, K.; Boyce, B. L.; Roberts, S. A.; Attia, P. M.; Harris, S. J. Rethinking How External Pressure Can Suppress Dendrites in Lithium Metal Batteries. *J. Electrochem. Soc.* **2019**, *166* (15), 3639–3652. https://doi.org/10.1149/2.0701914jes.

(96) Masias, A.; Felten, N.; Garcia-Mendez, R.; Wolfenstine, J.; Sakamoto, J. Elastic, Plastic,

and Creep Mechanical Properties of Lithium Metal. *J. Mater. Sci.* **2019**, *54* (3), 2585–2600. https://doi.org/10.1007/s10853-018-2971-3.

(97) Xu, C.; Ahmad, Z.; Aryanfar, A.; Viswanathan, V.; Greer, J. R. Enhanced Strength and Temperature Dependence of Mechanical Properties of Li at Small Scales and Its Implications for Li Metal Anodes. *Proc. Natl. Acad. Sci. U. S. A.* **2017**, *114* (1), 57–61. https://doi.org/10.1073/pnas.1615733114.

(98) Wang, Y.; Dang, D.; Xiao, X.; Cheng, Y. T. Structure and Mechanical Properties of Electroplated Mossy Lithium: Effects of Current Density and Electrolyte. *Energy Storage Mater.* **2020**, *26*, 276–282. https://doi.org/10.1016/j.ensm.2020.01.004.

(99) Ponce, V.; Galvez-Aranda, D. E.; Seminario, J. M. Analysis of a Li-Ion Nanobattery with Graphite Anode Using Molecular Dynamics Simulations. *J. Phys. Chem. C* **2017**, *121* (23), 12959–12971. https://doi.org/10.1021/acs.jpcc.7b04190.

(100) Xu, Z.; Buehler, M. J. Nanoengineering Heat Transfer Performance at Carbon Nanotube Interfaces. *ACS Nano* **2009**, *3* (9), 2767–2775. https://doi.org/10.1021/nn9006237.

(101) Plimpton, S. Fast Parallel Algorithms for Short-Range Molecular Dynamics. *Journal of Computational Physics*. 1995, pp 1–19. https://doi.org/10.1006/jcph.1995.1039.

(102) Stukowski, A. Visualization and Analysis of Atomistic Simulation Data with OVITO-the Open Visualization Tool. *Model. Simul. Mater. Sci. Eng.* **2010**, *18* (1), 015012. https://doi.org/10.1088/0965-0393/18/1/015012.

(103) Lee, H.; Chen, S.; Ren, X.; Martinez, A.; Shutthanandan, V.; Vijayakumar, M.; Han, K. S.; Li, Q.; Liu, J.; Xu, W.; Zhang, J. G. Electrode Edge Effects and the Failure Mechanism of Lithium-Metal Batteries. *ChemSusChem* **2018**, *11* (21), 3821–3828. https://doi.org/10.1002/cssc.201801445.

(104) Gaissmaier, D.; Fantauzzi, D.; Jacob, T. First Principles Studies of Self-Diffusion Processes on Metallic Lithium Surfaces. *J. Chem. Phys* **2019**, *150*, 41723. https://doi.org/10.1063/1.5056226.

(105) Ghassemi, H.; Au, M.; Chen, N.; Heiden, P. A.; Yassar, R. S. Real-Time Observation of Lithium Fibers Growth inside a Nanoscale Lithium-Ion Battery. *Appl. Phys. Lett.* **2011**, *99* (12), 123113. https://doi.org/10.1063/1.3643035.

(106) Zeng, Z.; Liang, W. I.; Liao, H. G.; Xin, H. L.; Chu, Y. H.; Zheng, H. Visualization of Electrode-Electrolyte Interfaces in LiPF6/EC/DEC Electrolyte for Lithium Ion Batteries via in Situ TEM. *Nano Lett.* **2014**, *14* (4), 1745–1750. https://doi.org/10.1021/nl403922u.

(107) He, Y.; Ren, X.; Xu, Y.; Engelhard, M. H.; Li, X.; Xiao, J.; Liu, J.; Zhang, J. G.; Xu, W.; Wang, C. Origin of Lithium Whisker Formation and Growth under Stress. *Nat. Nanotechnol.* **2019**, *14* (11), 1042–1047. https://doi.org/10.1038/s41565-019-0558-z.

(108) Uhlig, H. H.; Revie, R. W. *Corrosion and Corrosion Control. An Introduction to Corrosion Science and Engineering. Third Edition.*; 1985.

(109) Beleevskii, V. S.; Kudelin, Y. I.; Lisov, S. F.; Timonin, V. A. Electrochemical and Corrosion Behavior of Metals in Solutions of Weak Acids and Salts of Weak Acids. *Sov.*

Mater. Sci. **1991**, *26* (6), 622–628. https://doi.org/10.1007/BF00723646.

(110) Alekseev, V. I.; Perkas, M. M.; Yusupov, V. S.; Lazarenko, G. Y. The Mechanism of Metal Corrosion Passivation. *Russ. J. Phys. Chem. A* **2013**, *87* (8), 1380–1385. https://doi.org/10.1134/S0036024413080049.

(111) Richey, F. W.; McCloskey, B. D.; Luntz, A. C. Mg Anode Corrosion in Aqueous Electrolytes and Implications for Mg-Air Batteries. *J. Electrochem. Soc.* **2016**, *163* (6), A958–A963. https://doi.org/10.1149/2.0781606jes.

(112) Macdonald, D. Fundamental Studies of Passivity and Passivity Breakdown. *DOE Rep.* **1994**.

(113) Jones, D. A. Principles and Prevention of Corrosion, Prentice-Hall International, NJ, USA. *Encephale*. 1996, p Prentice-Hall International, NJ, USA.

(114) Brodd, R. J. *Advanced Batteries.*; 1985; Vol. 15. https://doi.org/10.1007/978-0-387-76424-5.

(115) Dahn, J. R. S163163 ---- AND Ts SCIs163. **2009**, *137* (7), 3–7.

(116) Goodenough, J. B.; Park, K. J. B. Goodenough and K.-S. Park, J. Amer. Chem. Soc. *J. Am. Chem. Soc.* **2012**, *135*, 1167.

(117) Winter, M. The Solid Electrolyte Interphase - The Most Important and the Least Understood Solid Electrolyte in Rechargeable Li Batteries. *Zeitschrift fur Phys. Chemie* **2009**, *223* (10–11), 1395–1406. https://doi.org/10.1524/zpch.2009.6086.

(118) Wang, H. F.; Xu, Q. Materials Design for Rechargeable Metal-Air Batteries. *Matter* **2019**, *1* (3), 565–595. https://doi.org/10.1016/j.matt.2019.05.008.

(119) Winter, M.; Barnett, B.; Xu, K. Before Li Ion Batteries. *Chem. Rev.* **2018**, *118* (23), 11433–11456. https://doi.org/10.1021/acs.chemrev.8b00422.

(120) Xiong, S.; Diao, Y.; Hong, X.; Chen, Y.; Xie, K. Characterization of Solid Electrolyte Interphase on Lithium Electrodes Cycled in Ether-Based Electrolytes for Lithium Batteries. *J. Electroanal. Chem.* **2014**, *719*, 122–126. https://doi.org/10.1016/j.jelechem.2014.02.014.

(121) Chang, Y.; Wang, M.; Wang, S.; Na, J.; Bund, A.; Nanjundan, A. K.; Yamauchi, Y. Ultralong Storage Life of Li/MnO2 Primary Batteries Using MnO2-(CFx)n with C–F Semi-Ionic Bond as Cathode Materials. *Electrochim. Acta* **2019**, *320*, 134618. https://doi.org/10.1016/j.electacta.2019.134618.

(122) Ren, X.; Zou, L.; Cao, X.; Engelhard, M. H.; Liu, W.; Burton, S. D.; Lee, H.; Niu, C.; Matthews, B. E.; Zhu, Z.; Wang, C.; Arey, B. W.; Xiao, J.; Liu, J.; Zhang, J. G.; Xu, W. Enabling High-Voltage Lithium-Metal Batteries under Practical Conditions. *Joule* **2019**, *3* (7), 1662–1676. https://doi.org/10.1016/j.joule.2019.05.006.

(123) Hobold, G. M.; Lopez, J.; Guo, R.; Minafra, N.; Banerjee, A.; Shirley Meng, Y.; Shao-Horn, Y.; Gallant, B. M. Moving beyond 99.9% Coulombic Efficiency for Lithium Anodes in Liquid Electrolytes. *Nat. Energy* **2021**, *6* (10), 951–960.

https://doi.org/10.1038/s41560-021-00910-w.

(124) Lee, J. Z.; Wynn, T. A.; Schroeder, M. A.; Alvarado, J.; Wang, X.; Xu, K.; Meng, Y. S. Cryogenic Focused Ion Beam Characterization of Lithium Metal Anodes. *ACS Energy Lett.* **2019**, *4* (2), 489–493. https://doi.org/10.1021/acsenergylett.8b02381.

(125) Fang, C.; Lu, B.; Pawar, G.; Zhang, M.; Cheng, D.; Chen, S.; Ceja, M.; Doux, J.-M.; Musrock, H.; Cai, M.; Liaw, B.; Meng, Y. S. Pressure-Tailored Lithium Deposition and Dissolution in Lithium Metal Batteries. *Nat. Energy* **2021**, *6* (October), 987–994. https://doi.org/10.1038/s41560-021-00917-3.

(126) Lin, C. F.; Kozen, A. C.; Noked, M.; Liu, C.; Rubloff, G. W. ALD Protection of Li-Metal Anode Surfaces – Quantifying and Preventing Chemical and Electrochemical Corrosion in Organic Solvent. *Adv. Mater. Interfaces* **2016**, *3* (21), 1–7. https://doi.org/10.1002/admi.201600426.

(127) Tobishima, S.; Sakurai, Y.; Yamaki, J. Safety Characteristics of Rechargeable Lithium Metal Cells. *J. Power Sources* **1997**, *68* (2), 455–458. https://doi.org/10.1016/S0378-7753(96)02584-0.

(128) Yamaki, J. I.; Tobishima, S. I.; Sakurai, Y.; Saito, K. I.; Hayashi, K. Safety Evaluation of Rechargeable Cells with Lithium Metal Anodes and Amorphous V2O5 Cathodes. *J. Appl. Electrochem.* **1998**, *28* (2), 135–140. https://doi.org/10.1023/A:1003270406759.

(129) Grace, W. R. Life, Performance. **1990**, 0–3.

(130) Hess, S.; Wohlfahrt-Mehrens, M.; Wachtler, M. Flammability of Li-Ion Battery Electrolytes: Flash Point and Self-Extinguishing Time Measurements. *J. Electrochem. Soc.* **2015**, *162* (2), A3084–A3097. https://doi.org/10.1149/2.0121502jes.

(131) Puthusseri, D.; Parmananda, M.; Mukherjee, P. P.; Pol, V. G. Probing the Thermal Safety of Li Metal Batteries. *J. Electrochem. Soc.* **2020**, *167* (12), 120513. https://doi.org/10.1149/1945-7111/ababd2.

(132) Liu, D. H.; Bai, Z.; Li, M.; Yu, A.; Luo, D.; Liu, W.; Yang, L.; Lu, J.; Amine, K.; Chen, Z. Developing High Safety Li-Metal Anodes for Future High-Energy Li-Metal Batteries: Strategies and Perspectives. *Chem. Soc. Rev.* **2020**, *49* (15), 5407–5445. https://doi.org/10.1039/c9cs00636b.

(133) Shi, F.; Ross, P. N.; Somorjai, G. A.; Komvopoulos, K. The Chemistry of Electrolyte Reduction on Silicon Electrodes Revealed by in Situ ATR-FTIR Spectroscopy. *J. Phys. Chem. C* **2017**, *121* (27), 14476–14483. https://doi.org/10.1021/acs.jpcc.7b04132.

(134) Julien, C. M.; Mauger, A.; Zaghib, K.; Groult, H. Comparative Issues of Cathode Materials for Li-Ion Batteries. *Inorganics* **2014**, *2* (1), 132–154. https://doi.org/10.3390/inorganics2010132.

(135) Li, W.; Cheng, D.; Shimizu, R.; Li, Y.; Yao, W.; Raghavendran, G.; Zhang, M.; Meng, Y. S. Artificial Cathode Electrolyte Interphase for Improving High Voltage Cycling Stability of Thick Electrode with Co-Free 5 V Spinel Oxides. *Energy Storage Mater.* **2022**, *49* (January), 77–84. https://doi.org/10.1016/j.ensm.2022.04.002.

(136) Chen, T.; Wang, H.; Innocenti, B. *Tekscan Measurements of Interfacial Contact Area and Stress in Articulating Joints*; Elsevier Inc., 2017. https://doi.org/10.1016/B978-0-12-803802-4.00017-2.

(137) Zhang, M.; Chouchane, M.; Shojaee, S. A.; Winiarski, B.; Liu, Z.; Li, L.; Pelapur, R.; Shodiev, A.; Yao, W.; Doux, J.-M.; Wang, S.; Li, Y.; Liu, C.; Lemmens, H.; Franco, A. A.; Meng, Y. S. Coupling of Multiscale Imaging Analysis and Computational Modeling for Understanding Thick Cathode Degradation Mechanisms. *SSRN Electron. J.* **2022**, 1–20. https://doi.org/10.2139/ssrn.4241175.